FRACTURE AND FAILURE OF LAYERED MATERIALS UNDER THERMO-MECHANICAL LOADING

by

Sharath P. Shetty

B. Tech., Indian Institute of Technology, Bombay, India
(1995)

Submitted to the Department of Aeronautics and Astronautics
in partial fulfillment of
the requirements for the degree of

Master of Science
in Aeronautics and Astronautics

at the
Massachusetts Institute of Technology

May 1997

Signature of Author_____
Department of Aeronautics and Astronautics
May 21, 1997

Certified by_____
Professor S. Mark Spearing
Thesis Supervisor

Accepted by_____
Professor Jaime Peraire
Chairman, Departmental Graduate Committee

FRACTURE AND FAILURE OF LAYERED MATERIALS UNDER THERMOMECHANICAL LOADING

by
Sharath P. Shetty

Submitted to the Department of Aeronautics and Astronautics on May 21, 1997 in partial fulfillment of the requirements for the degree of Master of Science in Aeronautics and Astronautics

ABSTRACT

The problem of joining two or more layers of dissimilar materials is commonly encountered in structural design, particularly in the aerospace industry. When these layered materials are subjected to thermo-mechanical loading, the mismatch between the thermoelastic properties of the materials, combined with the presence of a discrete interface between each pair of materials, can result in fracture of one or more layers or the interface between them. The reliability of such joints, therefore, is a recurring issue in their design. In this thesis, steady-state fracture mechanics solutions are used as a tool for analyzing the failure behavior of single and double composite-metal lap joints. This allows prediction of the failure mode and load to cause failure as a function of material properties, geometry, and interface toughness. The results are compared with data from an experimental program consisting of thermal loading tests on specimens composed of aluminum/graphite-epoxy composite. The adhesive toughness was obtained from mechanical tests on aluminum specimens. The results from the thermal tests confirm that steady-state analysis correctly predicts trends in the critical temperature drop for failure and the resulting failure modes. It was also observed that a single value of adhesive toughness is not sufficient to describe the data. Possible reasons for this phenomenon are investigated. The mechanical tests revealed that scrim-reinforced film adhesives can exhibit resistance curve behavior. Finally, failure design maps for composite-metal joints are presented; these are readily used for preliminary design, presentation of experimental data, and failure mode analysis.

Thesis Supervisor: S. Mark Spearing

Title: Assistant Professor, Department of Aeronautics and Astronautics, Massachusetts Institute of Technology

ACKNOWLEDGMENTS

The person I'd like to thank the most for making this possible is my advisor Mark, who's guidance, advice and support have been invaluable to me. Mark has been much more than an advisor to me; he's taken a very personal interest in me right from the day I arrived in the US. Working with Mark has always been a lot of fun, and one of my most valuable experiences here.

I'd also like to thank the other professors: Paul, Hugh, and Prof. Dugundji, from whom I've learnt a lot over the past 2 years. Thanks also to Deb and Ping for taking care of the little things that matter the most. I could never have completed my experiments without the help of Al, who was always patient and ever-willing to share his wisdom. I'm also grateful to John for help during my testing. Also thanks to Don & Dick in the machine shop, and Lenny in Mat. Sci. for their help. Thanks to Mary for being a great UROP'er and for working hard even when high on acetone.

Of course, the best part about the lab are its students...special thanks to Hary and Brian for always answering my questions. Thanks to Chris and Bari for all the late night homework sessions and to Kaustubh, Chris and Steve for the sessions of mmm...beer! Thanks to Mark Tudela for giving me a reputation in TELAC (@#$%!), and for being part of so many memorable incidents. Also thanks to Bethany, Dennis, Kuo-Shen, Lauren, Luis, Ronan and Tom, all of whom have always been willing to lend a helping hand.

The biggest reason I've made it this far in life is the support, encouragement and inspiration that my parents have provided me. Thanks to my parents and Shaila for always being there.

TABLE OF CONTENTS

LIST OF FIGURES 7

LIST OF TABLES 11

NOMENCLATURE 12

1. INTRODUCTION 15

   1.1 RELIABILITY OF MULTILAYER SYSTEMS 16

   1.2 PRESENT WORK 16

   1.3 OVERVIEW 18

2. BACKGROUND 20

   2.1 MODELING OF THE MECHANICS OF LAYERED MATERIALS 20

      2.1.1 Residual Stresses 20

      2.1.2 Fracture Mechanics 21

   2.2 ADHESIVE LAP JOINTS 23

      2.2.1 Approach To Modeling Of Adhesive Joints 24

      2.2.2 Testing Of Adhesive Joints 25

   2.3 STRESS-BASED VS. ENERGY-BASED APPROACHES 26

   2.4 DESIGN DIAGRAMS FOR RELIABILITY 27

   2.5 SUMMARY 28

3. ANALYTICAL MODELING 30

   3.1 MECHANICS OF LAYERED MATERIALS 30

      3.1.1 Failure Modes and Parameters for their Characterization 31

      3.1.2 Stress Calculations 32

      3.1.3 Interfacial Strain Energy Release Rate 34

      3.1.4 Strain Energy Release Rate for Delamination/ 36

Spalling
3.1.5 Stresses for Matrix Cracking/ Crazing 39
3.2 FAILURE CRITERIA 40
3.3 SHORT CRACK EFFECTS 41
4. EXPERIMENTAL METHOD 54
4.1 THERMAL TESTING 54
4.1.1 Specimen Fabrication/ Materials 55
4.1.2 Non-Precracked Specimens 55
4.1.3 Precracked Specimens 56
4.1.4 Test Procedure 57
4.2 MECHANICAL TESTING 58
4.2.1 Specimen Fabrication and Materials 58
4.2.2 Test Procedure 59
4.3 FRACTURE IN CERAMIC MATRIX COMPOSITES/ CERAMICS 60
4.4 FRACTOGRAPHY 61
5. OBSERVATIONS AND RESULTS 67
5.1 THERMAL TEST RESULTS 67
5.1.1 Pre-Testing Observations 67
5.1.2 Fractography 68
5.1.3 Non-precracked Thermal Tests 69
5.1.4 Pre-cracked Thermal Tests 70
5.2 MECHANICAL TEST RESULTS 71
5.2.1 Mode I Tests 71
5.2.2 Mode II Tests 72
5.2.3 Fractography/ Observations 73
5.3 CERAMIC/CMC SPECIMENS 73
6. DISCUSSION 92

6.1 INFERENCES FROM EXPERIMENTAL WORK 92
6.1.1 Results from thermal testing and correlation with mechanical testing 92
6.1.2 Mode-mixity 93
6.1.3 Short Crack Effects 94
6.1.4 Temperature Dependence of Adhesive Properties 95
6.1.5 Edge-Stress Analysis 96
6.1.5 Material Non-linearity 96
6.2 R-CURVE MODELING 97
6.3 FAILURE MECHANISM MAPS 99
7. CONCLUSIONS AND RECOMMENDATIONS 112
7.1 CONCLUSIONS 115
7.2 RECOMMENDATIONS FOR FUTURE WORK 115
REFERENCES 118

LIST OF FIGURES

Figure 1.1	Schematic representations of crazing of layer 1(a) and layer 2 (b), interfacial fracture (c) and spalling of layer 2 (d)	19
Figure 3.1	Failure modes of a composite-metal single lap joint	43
Figure 3.2	Illustration of control volumes far ahead and behind the crack tip	43
Figure 3.3	Strain energy release rate for single lap joint undergoing interfacial fracture	44
Figure 3.4	Strain energy release rate for double lap joint undergoing interfacial fracture	45
Figure 3.5	Delamination height (from interface) vs. thickness ratio	46
Figure 3.6	Strain energy release rate for single lap joint undergoing composite delamination	47
Figure 3.7	Illustration of delamination/alligatoring in a double lap joint	48
Figure 3.8	Delamination height (from interface) vs. thickness ratio for a double lap joint	48
Figure 3.9	Strain energy release rate for double lap joint undergoing composite delamination	49
Figure 3.10	Strain energy release rate for double lap joint undergoing alligatoring	50
Figure 3.11	Maximum tensile stresses in layer 1 (0° composite) at the outer edge of the composite	51
Figure 3.12	Maximum tensile stresses in layer 1 (90° composite) at the interface	52

Figure 3.13	Non-dimensional strain energy release rate for two thickness ratios as a function of crack length	53
Figure 4.1	Typical specimen geometry for thermal testing experiments	63
Figure 4.2	Specimen for mode I fracture testing experiments	64
Figure 4.3	Specimen for mode II fracture testing experiments	64
Figure 4.4	Testing configuration for mode I fracture data	65
Figure 4.5	Testing configuration for mode II fracture data	66
Figure 5.1	Curvature of bilayer specimens plotted against thickness ratio	75
Figure 5.2	(a) Illustration of fracture path in composite-metal lap joints (b) SEM micrograph of the transition region in the adhesive	76
Figure 5.3	SEM micrographs of fracture surface (a) close-up of transition region (b) adhesive surface away from transition region	77
Figure 5.4	Thermal fracture data for unprecracked single lap joints between $[0]_{16}$ graphite-epoxy/ aluminum adherends	78
Figure 5.5	Thermal fracture data for unprecracked double lap joints between $[0]_{16}$ graphite-epoxy/ aluminum adherends	79
Figure 5.6	Thermal fracture data for precracked single lap joints between $[0]_{16}$ graphite-epoxy/ aluminum adherends	80
Figure 5.7	Thermal fracture data for precracked double lap joints between $[0]_{16}$ graphite-epoxy/ aluminum adherends	81
Figure 5.8	Thermal fracture data for precracked single lap joints between $[0]_{32}$ graphite-epoxy/ aluminum	82

adherends

Figure 5.9 Thermal fracture data for precracked single lap joints between $[0]_{16}$ graphite-epoxy/ steel adherends 83

Figure 5.10 Thermal fracture data for precracked single lap joints between $[90_4/0_4]_s$ graphite-epoxy/ aluminum adherends 84

Figure 5.11 Micrograph showing delamination between 90° and 0° layers in $[90_4/0_4]_s$ graphite-epoxy/ aluminum specimens 85

Figure 5.12 Typical load vs. time plot for a DCB specimen 86

Figure 5.13 Mode I fracture resistance data for aluminum adherends 87

Figure 5.14 Mode II fracture resistance data at room temperature for aluminum adherends bonded with FM 123-2 adhesive 88

Figure 5.15 SEM micrograph of fracture surface of adhesive showing presence of bundles of scrim fibers (a) at starter crack, and (b) away from starter crack 89

Figure 5.16 SEM close-up micrograph of adhesive fracture surface showing pull-out of scrim fibers at oblique angles 90

Figure 5.17 Optical micrograph of spallation, debonding, and crazing in alumina bonded with nicalon-reinforced calcium aluminosilicate 91

Figure 6.1 R-curve modeling and bridging law 103

Figure 6.2 R-curve calculated assuming softening bridging tractions, superimposed on fracture resistance calculated from measured data 104

Figure 6.3 Predicted R-curves for DCB specimens of three different thicknesses assuming the bridging behavior shown in figure 6.1 105

Figure 6.4 Failure mechanism diagram for $[0]_{16}$ AS4/3501-6 106

graphite/epoxy-aluminum single lap joint

Figure 6.5 Failure mechanism diagram for $[0_4/90_4]_s$ AS4/3501-6 graphite/epoxy-aluminum single lap joint 107

Figure 6.6 Failure mechanism diagram for $[0]_{16}$ AS4/3501-6 graphite/epoxy-aluminum double lap joint 108

Figure 6.7 Failure mechanism diagram for alumina/ Nicalon-reinforced CAS 109

Figure 6.8 E-α contour map for selection of material to be joined with 2mm thick AS4/3501-6 graphite-epoxy in order to avoid interfacial fracture 110

Figure 6.9 E-α contour map for selection of material to be joined with 2mm thick AS4/3501-6 graphite-epoxy on both sides to form a symmetric double lap joint. Design is against interfacial fracture 111

LIST OF TABLES

Table 3.1	List of values for Dundurs parameters for representative metals.	42
Table 4.1	Thermomechanical Properties Of Adherends	60
Table 4.2	Test matrix of precracked specimens	60

NOMENCLATURE

a	Crack length in double cantilever beam specimen
A	Elastic mismatch parameter
B	Width of double cantilever beam specimen
E_i	Elastic modulus of layer i
E_L	Longitudinal modulus of composite
E_T	Transverse modulus of composite
h	Delamination stand-off distance
$\mathcal{G}$	Strain energy release rate
$\mathcal{G}_{all}$	Critical strain energy release rate for alligatoring
$\mathcal{G}_{delam}$	Critical strain energy release rate for delamination
$\mathcal{G}_{ic}$	Adhesive fracture energy
G_{ss}	Steady-state strain energy release rate
G_o	Initiation critical strain energy release rate
G_{Ic}	Mode I critical strain energy release rate
G_{IIc}	Mode II critical strain energy release rate
K_I	Mode I stress intensity factor
K_{II}	Mode II stress intensity factor
l	Crack length
L	Length of DCB specimen
L_{ss}	Steady-state bridging length
M_i	Bending moment per unit width in layer i

P_i	In-plane force per unit width in layer i
p_o	Bridging law load parameter
R	Radius of curvature
t_i	thickness of layer i
t_{al}	thickness of aluminum layer
t_c	thickness of composite layer
t_{st}	thickness of steel layer
$\mathcal{U}_a$	Strain energy per unit length behind crack tip in symmetric trilayer undergoing alligatoring
$\mathcal{U}_d$	Strain energy/length ahead of crack tip in a symmetric trilayer
$\mathcal{U}_r$	Strain energy/length behind a delamination crack
$\mathcal{U}_t$	Strain energy/length ahead of crack tip in a bimaterial beam
u_o	Bridging law displacement parameter
α_i	Coefficient of thermal expansion of layer i
α_L	Longitudinal coefficient of thermal expansion of composite
α_T	Transverse coefficient of thermal expansion of composite
β	Term in strain energy expression (equation 3.2)
δa	Incremental crack length
ΔT	Change in temperature relative to stress-free temperature
ε_t	Free thermal strain
η	Ratio of delamination depth to layer thickness
λ	Ratio of layer elastic moduli
ν_i	Poisson's ratio of layer i
ν_{LT}	Poisson's ratio (longitudinal-transverse) of composite

ν_{TL}	Poisson's ratio (transverse-longitudinal) of composite
σ_{ji}	Stress in layer j at the interface
σ_{jo}	Stress in layer j at the outer surface
σ_T	Transverse strength of composite
ξ	Ratio of layer thicknesses

CHAPTER 1

INTRODUCTION

Multilayered components and structures are increasingly used in high performance applications. These generally have multiple functional requirements, which are often achieved by combining two or more constituent materials in a layered fashion. Designers have the flexibility of optimizing a wide variety of mechanical, thermal, electrical, and environmental properties by judiciously layering combinations of metals, composites, ceramics and polymers.

The aerospace industry provides many examples of the use of multilayer systems, including foam insulation on metal cryogenic tanks, metal facings for increasing the erosion resistance of composite substructures, and ceramic thermal barrier coatings on engine combustor liners. Many of these structures are built by adhesively bonding successive layers at their respective interfaces. Adhesive joints are also potentially more structurally efficient than mechanical fasteners as they can achieve a significant weight saving.

1.1 RELIABILITY OF MULTILAYER SYSTEMS

When a pair of materials adhesively bonded together is subjected to thermal or mechanical loading, stresses are produced due to the mismatch in thermo-mechanical properties between them. Reliability of the system then becomes a concern due to the combined effect of this stress state, together with the presence of a discrete interface between the layers. Failure can occur by one or more of several modes.

Figure 1.1 is an illustration of the different failure modes possible in a bilayer. There are four possible modes: crazing of one or other layer, interfacial fracture, and spalling. When one of the layers is a laminated composite, additional failure modes can result due to delamination and matrix cracking of the composite. These are dealt with in more detail in chapter 3. In addition, permanent deformation may result from inelastic constitutive behavior of the materials; this is not addressed in the present work.

1.2 PRESENT WORK

The evaluation and enhancement of the mechanical reliability of multilayers have emerged as high priority subjects to material scientists and

solid mechanicians alike. This has led to significant advances in predictive methodologies for failure of layered materials, as is described in chapter 2.

The aim of the present work is to extend previous work on multilayer design to the reliability of dissimilar materials, particularly adhesive joints, under thermo-mechanical loading. Steady-state fracture mechanics solutions are used as a tool for predicting the failure behavior of single and double lap joints between metals and composites. The analysis is conducted assuming linear, elastic, brittle behavior in the adherends. Solid mechanics and fracture mechanics analyses are performed to determine the onset of each failure mode as a function of the thermo-elastic properties of the adherends and the thermal loading. The analysis was supported by an experimental program involving thermal testing of composite-to-metal joints. Mechanical testing was also performed to independently verify the adhesive toughness values used to model the fracture under purely thermal loading.

Lap joints between composite and metal adherends were chosen because they are particularly demanding structural features. The composite is anisotropic, heterogeneous, and, depending on the laminate stacking sequence, can possess a very low thermal expansion coefficient relative to the metal. This makes the joints very susceptible to failure, which can be induced experimentally for verification with theory. The methodology, however, is not restricted to adhesive joints, and can be applied equally well to any of the multilayer systems described earlier. The objective of using steady-state

fracture mechanics is to obtain a conservative lower bound estimate of the load to cause failure, that can be useful for material selection and preliminary design of multilayers.

1.3 OVERVIEW

In chapter 2, previous work relevant to the problem is reviewed. This includes early work on the subject, studies contributing to present understanding, and recent work on the topic. The analytical methodology, including the fracture mechanics model and failure predictions, is developed in chapter 3. Chapter 4 describes the thermal and mechanical testing carried out to verify the analysis. Experimental data from the thermal and mechanical tests are presented in chapter 5, along with comparisons with predictions. The implications of these results are discussed in chapter 6. Conclusions and recommendations for future work are made in chapter 7.

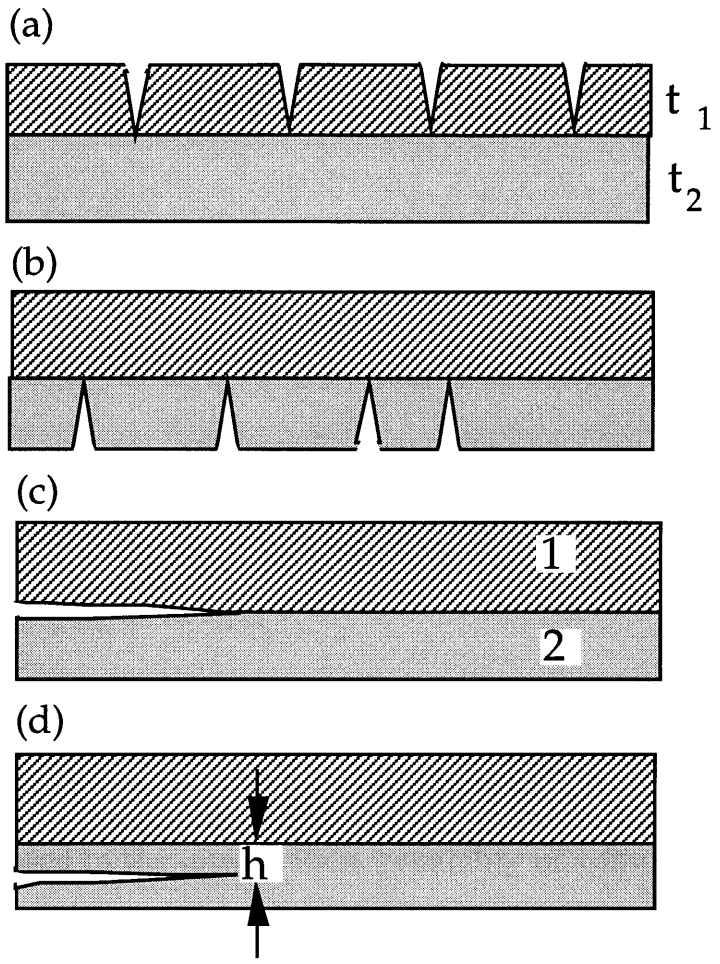

Figure 1.1 Schematic representations of crazing of layer 1(a) and layer 2 (b), interfacial fracture (c) and spalling of layer 2 (d)

CHAPTER 2

BACKGROUND

This chapter reviews past and current work on understanding the mechanical behavior of layered materials and adhesive joining. Layered materials in general are addressed in section 2.1, followed by a review of work related to adhesive joints in section 2.2.

2.1 MODELING OF THE MECHANICS OF LAYERED MATERIALS

As discussed in the introduction, reliability in a multilayer system is a concern due, in part, to the mismatch in the thermal and elastic properties between the constituents which causes misfit stresses to be generated. This section reviews existing literature on attempts to address this and related problems.

2.1.1 Residual Stresses

Residual stresses can arise from several sources; they can be a consequence of thermal expansion differences between the constituent materials of a multilayer system, from the processing method used [1], from

plasticity in one or more adherends, or from cyclic plasticity under thermal cycling [2], or from piezoelectric deformations [3]. The particular case of thermal stress has been addressed in detail by Doerner and Nix [4], in their review article. This problem was first analyzed more than eight decades ago by Stoney [5], in his article on thin films. This was followed by a detailed analysis of a bimetallic strip by Timoshenko [6]. Consequently, the problem is now well-characterized for different geometries, material response, and loading patterns [7]. Problems involving determination of biaxial residual stresses in layered plates can now be easily solved using classical laminated plate theory (CLPT) [8].

2.1.2 Fracture Mechanics

As seen in the introduction, failure can occur by interfacial fracture, spalling, crazing, or a combination of the three modes (see figure 1.1). Studies on fracture in layered materials have mostly concentrated on interfacial cracks in bilayers.

The elasticity theory of interfacial cracks in layered materials was developed in the 60's and 70's, primarily by Erdogan and his coworkers [9, 10], England [11] and Rice and Sih [12]. Traditionally, the problem has been tackled by considering the singular stress field at the tip of the crack. Interface cracking is a mixed-mode problem, unlike cracking within isotropic solids, where the crack is free to evolve maintaining mode I conditions at its

tip. The asymmetry in elastic moduli with respect to the interface, as well as possible nonsymmetric loading and geometry, induces a mode II component. The mismatch in moduli between interfaces was shown to depend on only two non-dimensional combinations of elastic moduli by Dundurs [13]. The crack tip stress intensity factor is complex (it has real and imaginary parts), and is characterized by an oscillatory index which depends on one of the Dundurs' parameters [14].

The problem has received renewed attention more recently, especially since the late 1980's. A particular focus has been on fracture problems in multilayer structures that are subject to a steady-state strain energy release rate [14-17]. In these cases, the analysis can be simplified because the need to analyze the complex stress intensities in the crack tip region is circumvented. A large body of recent work on mixed-mode fracture has been prompted by considering interface fracture in ceramics and this has been generalized to examine failures in other systems such as fiber composites [18]. A substantial amount of experimental work has complemented theoretical investigations. These studies, partly referenced here, have mainly focused on the development of techniques for measuring interface toughnesses [19-23].

The problem of spallation in brittle materials has also been addressed recently, based on experiments which have revealed that cracks in films exposed to residual tension have a strong tendency to extend into brittle substrates and evolve into a trajectory parallel to the interface [24, 25]. The

problem has been formulated analytically by solving for the stress intensity factors at the crack tip, combined with the criterion that the crack has zero mode II component [15]. Orthotropy introduces additional complications, and the problem becomes very difficult to analyze.

Hutchinson and Suo have written an excellent review article which summarizes the current predictive capability for the fracture of layered materials [14]. The cracking and decohesion of thin films is a topic that has been dealt with extensively in the literature [15, 25-27], and in many cases, these analyses can be extended to bilayers in general, and thence, to multilayers. Reference [28] is a good source for the current state-of-the-art in thin film analysis.

2.2 ADHESIVE LAP JOINTS

Adhesive lap joints can, in general, be considered a subset of layered materials in which the adhesive is a discrete layer of small thickness relative to the adherends. Many studies on this topic have focused the role of the adhesive layer. Particular attention has been given to whether the failure is within the adhesive layer or adherends (cohesive failure), or between the adhesive and adherend (adhesive failure). This section deals with the various approaches used to model the mechanical behavior of adhesive joints and some standard test methods.

2.2.1 Approach To Modeling Of Adhesive Joints

Literature on the analysis of adhesive joints dates back to the 1930's, with several authors concentrating on prediction of stresses. Volkerson [29] was the first to use elastic shear lag analysis to study double lap joints. Goland and Reissner [30] were the first to consider non-uniform stresses in adherends, and their work is a classical reference for single lap joints. Hart-Smith [31-33] extended their work to include elastic-plastic adhesive behavior and derived explicit solutions for stresses. His analysis predicted an increase in joint strength due to adhesive plasticity, and was able to explain premature failure predictions found when linear elastic behavior of the adhesive was assumed. Renton and Vinson [34] and Allman [35] have been some of the other major contributors in the field; they modeled the normal, bending and shear stresses in adherends in their analyses. These closed-form analyses are useful from the point of view of gaining a physical understanding of the problem, but become increasingly intractable for complex joint geometries and loading combinations. Finite element methods for stress analysis have also been popular among investigators [36-38] due to their relative convenience for complicated cases involving nonlinearities, complex boundary conditions, etc.

The aim of fracture mechanics approaches has been to analyze mathematically the loads at which intrinsic flaws in adhesive joints

propagate. Fracture mechanics has proved to be useful for such aspects as characterizing the toughness of adhesives, identifying mechanisms of failure, and estimating the service life of damaged components. Early attempts to evaluate strength of joints using fracture mechanics were made by Ripling *et al* [39]. Fracture mechanics approaches mentioned in section 2.1.2 have been applied to adhesive joints in recent years [14]. These approaches have been based on the premise that the *in situ* fracture response of the bondline can be characterized by a critical strain energy release rate as a function of the mode of loading, for a specific system. More recent efforts have been concentrated on the observation that local cracking morphology can have a strong effect on the interface toughness [14]. These and other associated problems such as crack path selection within the adhesive layer have also been approached using fracture mechanics models, with varying success [40-43].

2.2.2 Testing Of Adhesive Joints

The most commonly used standard test methods for assessing the performance of an adhesive joint are those issued by the American Society for Testing and Materials (ASTM). These tests are useful in maintaining comparative conditions wherever conducted, and enable the performance of practical adhesive joints to be estimated by simulating the geometries and stresses likely to be encountered [44]. These are typically strength evaluation tests under mechanical loading, (e.g. single lap joint tests and peel tests [45-

47]), and under hostile environmental conditions (elevated temperatures, moisture, etc. [48-50]). Adhesive fracture energy tests are limited to mode I fracture toughness evaluation [51]. Other fracture tests, such as mode II testing of adhesive joints and thermal testing of adhesive joints between dissimilar materials are not present in the standards literature.

Many authors have used experimental fracture mechanics with the aim of providing a critical parameter to characterize crack growth which is independent of test geometry. In order to validate this requirement, a wide range of different geometries has been developed [44]. Several authors have shown that the adhesive fracture energy G_c is independent of joint geometry for different kinds of adhesives for a range of adhesive thicknesses [52-54].

2.3 STRESS-BASED VS. ENERGY BASED APPROACHES

Stress-based failure criteria, in conjunction with closed form analyses of stresses within the adhesive, have been used to predict failure of joints. However, in order to use this approach, it is necessary to know the engineering properties of the adhesive (i.e. longitudinal and shear moduli, yield stress, fracture stress in uniaxial tension & pure shear). These properties are difficult to obtain reliably *in situ* because of the complex stress state induced in the adhesive layer by the specimen geometry and processing conditions.

Shear lag approaches used to predict stresses are convenient approximations for simple configurations, but are difficult to apply for more complex joints. Moreover, they usually involve experimental determination of shear lag parameters, which are often not generalizable to different systems.

A major advantage of energy methods is that the actual stress in the adhesive need not be considered; an effective toughness can be assigned to the system, which is, in general, a function of mode-mixity of the applied loading. This makes the problem much simpler to analyze, especially when used together with assumptions of steady-state cracking, so that a global energy release rate can be considered. A disadvantage of energy-based criteria is that the fracture energy is usually characteristic of a particular system, so experimental data for each combination of materials would be needed.

2.4 DESIGN DIAGRAMS FOR RELIABILITY

Efforts to construct guidelines for preliminary design and manufacture of layered materials in general have been made recently [3, 55]. These authors have used the concept of design diagrams to map performance metrics relevant to multifunctional design for multiple performance systems. The primary objective of these works has been to bring together recent developments in the fracture of layered materials in order to carry out fail-

safe multilayer designs. Such designs refer to multilayers that are incapable of thermostructural failure from the residual stresses existing in the system [17].

2.5 SUMMARY

A considerable body of recent work has attempted to characterize the fracture and failure of layered materials. Adhesive joints in particular have also been analyzed within a fracture mechanics framework. However, many holes still remain to be filled, some of which are addressed by this thesis.

An important issue that has not yet been explicitly investigated is the failure behavior of adhesive joints between dissimilar adherends under thermal loading. Also, assessment of the competition between failure modes has not been carried out experimentally. This work extends the design philosophy of Spearing *et al* [3, 55] to single and double lap joints between fiber-reinforced composites and metals, in order to identify material and geometric parameters that are relevant to preliminary design. In performing this analysis, a simple fracture mechanics based methodology is employed for prediction of stresses and failure. An effective toughness, which is a function of mode-mixity, is assigned to an adhesive joining the two materials, based on an expected failure mode. This eliminates the complications associated with the need to look at finer issues such as local cracking morphology. An

important assumption is that the adhesive layer is thin and has negligible influence on joint deformation. This approach considerably simplifies analysis; details are provided in chapter 3.

It should be noted that the objective of this work is not to provide a methodology for detailed design. Once preliminary design has been performed and relevant parameters identified using the suggested approach, more advanced techniques such as finite element analyses can be used for detailed design purposes.

CHAPTER 3

ANALYTICAL MODELING

This chapter describes the theoretical approach to the problem of the mechanical behavior of dissimilar bonded materials. The stress state solution is developed in terms of a few geometric and thermo-mechanical parameters, and the load applied. This is used as an input to a steady-state fracture mechanics model in order to compute the strain energy release rate. Finally, a failure criterion is used to predict the critical load to cause failure.

3.1 MECHANICS OF LAYERED MATERIALS

The mechanics of layered materials are illustrated by considering the case of composite to metal single and double lap joints. This configuration is useful for illustration of different failure modes; the model is easily extended to other combinations of materials. For simplicity, the loading is assumed initially to be purely thermal; mechanical loading could be incorporated subsequently by including an additional term in the governing equations, as will be indicated in section 3.1.2.

The role of the adhesive as a discrete layer is also ignored, by neglecting the thickness of the adhesive. The adherends are assumed to be linear-elastic and brittle. This assumption gives conservative lower bounds for fracture, as in practice, non-linear effects such as plasticity, viscoelasticity or creep of the adherends or adhesive may limit stress levels.

3.1.1 Failure Modes and Parameters for their Characterization

Figure 3.1 is an illustration of the failure modes in a composite-metal bilayer. There are three primary modes: debonding of the interface between the layers, delamination of the composite, and matrix cracking [56, 57]. Failure can occur by any combination of these modes. Delamination is analogous to spalling in isotropic materials, and matrix cracking occurs by a mechanism similar to crazing [3, 14, 27, 55]. Theoretically, metal spalling or crazing are also possible, but are unlikely due to the high toughness of the metal.

It is useful to invoke four non-dimensional geometric and material parameters to describe the stresses, deformations and elastic strain energy that result from application of a uniform thermal load. These parameters are as follows [13, 15-17]:

the ratio of layer thicknesses: $$\xi = t_1 / t_2 \qquad [3.1a]$$

the elastic mismatch parameter [13]: $$A = \frac{\bar{E}_1 - \bar{E}_2}{\bar{E}_1 + \bar{E}_2} \qquad [3.1b]$$

the ratio of the elastic moduli : $$\lambda = \frac{\bar{E}_1}{\bar{E}_2}\left(= \frac{1+A}{1-A}\right)$$ [3.1c]

and the free thermal strain: $$\varepsilon_t = (\alpha_1 - \alpha_2)\Delta T$$ [3.1d]

where $t_{1,2}$ are the thicknesses of the layers, $\bar{E}_{1,2}$ are the effective Young's moduli ($\bar{E}_i = E_i/(1-\nu_{LT}\nu_{TL})$ for plane strain, $\bar{E}_i = E_i$ for plane stress), $\alpha_{1,2}$ the coefficients of thermal expansion and ΔT the temperature change. In the case of the composite, the material properties in the longitudinal direction (in laminate axes) are considered.

3.1.2 Stress Calculations

The one-dimensional stress state in each material strip can be analyzed using simple Euler-Bernoulli beam theory. The thermal loading applied to the system can be considered as a superposition of a uniform in-plane force per unit width, P_j and a bending moment per unit width, M_j [6]. These can be obtained using equilibrium and compatibility of curvatures and interfacial strains of the materials [7, 58]. The expressions for P_j and M_j for an elastic bilayer as follows:

$$P_1 = -\xi\beta t_1\left(\lambda\xi^3 + 1\right)$$ [3.2a]

$$P_2 = +\xi\beta t_1\left(\lambda\xi^3 + 1\right)$$ [3.2b]

$$M_1 = +\frac{1}{2}\lambda\xi^3\beta t_1^2(\xi + 1)$$ [3.2c]

$$M_2 = +\frac{1}{2}\beta t_1^2(\xi+1) \qquad [3.2d]$$

where: $$\beta = \frac{\varepsilon_t E_1}{\xi(\lambda\xi^3+1)(\lambda\xi+1)+3\lambda\xi^2(\xi+1)^2}$$

Tensile forces, clockwise moments on rightward facing sections and temperature increases are defined as positive. The above equations were obtained assuming purely thermal loading; mechanical loads can be included by having additional force/moment terms in the equilibrium equations.

The radius of curvature of an elastic bilayer is given by the following expression:

$$R = \frac{E_1 t_1}{6\beta\lambda\xi^3(\xi+1)} \qquad [3.3]$$

The same approach is used for obtaining the stress state in a trilayer. For a symmetric double lap joint, the moments cancel out due to the restriction on bending. Uniform, in-plane forces act on each layer, given by:

$$P_1 = \frac{2E_1 t_1 \varepsilon_t}{2+\xi\lambda} \qquad [3.4a]$$

$$P_2 = \frac{-E_1 t_1 \varepsilon_t \xi}{2+\xi\lambda} \qquad [3.4b]$$

Here, t_1 refers to the total thickness of the center layer, and t_2 denotes the thickness of each of the outer layers.

The same methodology can be extended to general multilayers [14] or two-dimensional systems, by extending the same equations to include transverse stresses and strains.

3.1.3 Interfacial Strain Energy Release Rate

Interfacial fracture is an inherently mixed-mode problem, which can be modeled as a steady-state fracture phenomenon, i.e. strain energy released as the crack propagates is independent of the crack length. This provides a lower bound to the thermomechanical loading required for fracture [3, 14]. The strain energy available for crack propagation is calculated by considering control volumes of length δa far ahead and behind the crack tip (see figure 3.2). The difference between the elastic strain energy stored in the control volumes is equivalent to advancing the crack by a distance δa. This approach allows us to conveniently analyze the problem without considering the complex stress state at the crack tip.

For the case of interfacial debonding, the total stored strain energy ahead of the crack is used up in crack propagation (material far behind the crack tip is stress-free). The strain energy stored ahead of the crack tip in a bimaterial beam, per unit length is given by [3, 55]:

$$\mathcal{U}_t = \frac{\beta^2 t_1\left(\lambda\xi^3+1\right)}{2E_1}\left[\xi^2(\lambda\xi+1)\left(\lambda\xi^3+1\right)+3\lambda\xi^3(\xi+1)^2\right] \qquad [3.5]$$

The strain energy release rate is therefore given by:

$$\mathcal{G} = \mathcal{U}_t \qquad [3.6]$$

This expression is plotted in figure 3.3 for different values of the Dundurs parameter A. In order to relate these curves to real composite-metal joints, a list of metals is provided in table 3.1, spanning a wide range of values of A with respect to a composite layer. The composite properties in each case are those of unidirectional AS4/3501-6 graphite/epoxy with E_L=141 GPa, E_T=10 GPa, ν_{LT}=0.32, α_L= -0.5 ppm/K and α_T= 30 ppm/K. Note that for calculation of A, the composite is taken as layer 1.

For a double lap joint undergoing simultaneous debonding of both interfaces, the corresponding expression is:

$$\mathcal{U}_d = \frac{\varepsilon_t^2 t_1 \bar{E}_1}{2 + \lambda\xi} \qquad [3.7]$$

For the case of single interfacial fracture, the strain energy released is the difference of equations (3.7) and (3.5), i.e.

$$\mathcal{G} = \mathcal{U}_d - \mathcal{U}_t \qquad [3.8]$$

This is plotted in figure 3.4 for a range of values of A. The strain energy stored in the double lap joint is higher for any thickness ratio due to the inherent symmetry constraint.

3.1.4 Strain Energy Release Rate for Delamination/ Spalling

Spallation is a steady state fracture mode, in which the crack follows a mode I path, parallel to, but not at, the interface. Spallation manifests itself as a delamination in a unidirectional composite bonded to metal. In order to evaluate the strain energy release rate for delamination, it is first necessary to calculate the stand off distance, h, of the delamination crack from the interface. The problem is similar to finding the spall depth in an isotropic material. Suo and Hutchinson [15] have solved the latter problem by formulating an integral equation based on a kernel solution derived by considering an array of continuously distributed edge dislocations. Their solutions are specifically focused on the case of spallation due to a thin film on a thick substrate, but they are also valid for cases where ξ approaches unity. The method is described in detail in the appendices to their paper and the expressions for the mode I and mode II stress intensity factors can be obtained directly from equation [11] and appendix A of this reference [15].

In the present work solutions for $K_{II} = 0$ are obtained by applying a Newton-Raphson iterative routine to Suo and Hutchinson's equations, as was performed in [3]. The computed distance of the crack plane from the interface plane, h, is plotted as a function of thickness ratio in figure 3.5 for various values of A. The crack trajectory is a strong function of both the modulus mismatch and the thickness ratio. There is a limit to the occurrence of delamination, defined by the thickness ratio for which no mode I path exists

within the composite. This limit varies with modulus mismatch and is shown as a dashed line in Fig 3.5. This is of practical importance as it is possible to choose a value of ξ for which delamination is not a concern.

Given the distance, h, of the crack from the interfacial plane it is straightforward to determine the strain energy release rate for delamination in a similar manner as for interfacial fracture. The strain energy behind the crack tip is given by the same expression as in equation 3.5, with the substitution of η (=t_1/h) for ξ:

$$\mathcal{U}_r = \frac{\beta^2\eta^2 t_1\left(\lambda\eta^3+1\right)}{2E_1}\left[\eta^2(\lambda\eta+1)\left(\lambda\eta^3+1\right)+3\lambda\eta^3(\eta+1)^2\right] \qquad [3.9]$$

The difference between this residual strain energy and the total strain energy represents the steady state strain energy release rate for the delamination crack:

$$\mathcal{G}_{delam} = \mathcal{U}_t - \mathcal{U}_r \qquad [3.10]$$

This is plotted for a range of values of A against ξ in Fig. 3.6. The non-zero value of $\mathcal{U}_r$ implies that the strain energy release rate for delamination is less than that for interfacial fracture for any value of ξ.

For the case of double lap joints, delamination takes place symmetrically about the midplane, or through the midplane (i.e. the center of the composite layer). The latter mode is also referred to as alligatoring. In the former case, two mode I delamination cracks are assumed to grow

simultaneously at fixed stand-off distances from the midplane, for a given thickness ratio (see figure 3.7). The strain energy release rate associated with this mode is evaluated by finding the delamination stand-off distance from the composite-metal interface. This is done in a similar manner as for the single lap joint, with a slight modification. In this case, Suo and Hutchinson's [15] solutions are modified by enforcing the zero moment boundary condition on the composite layer. The delamination stand-off distance from the interface and the strain energy release rate for delamination are plotted for a range of values of A in figures 3.8 and 3.9 respectively. For the case of alligatoring, the strain energy per unit length behind the crack tip, $\mathcal{U}_a$, is the same as the total strain energy in a bilayer (equation 3.5), with $\xi/2$ instead of ξ and $t_1/2$ instead of t_1. The strain energy release rate for alligatoring, G_{all} is given by:

$$\mathcal{G}_{all} = \mathcal{U}_d - 2\,\mathcal{U}_a \qquad [3.11]$$

This is plotted as a function of thickness ratio for a range of values of A in figure 3.10.

For any ply configuration other than unidirectional, the delamination crack need not be mode I. In a cross-ply composite, for instance, the crack often tends to propagate at, or close to the 0/90 interface. In this case, the distance h is the height of this interface from the composite-metal interface. In the case of multiple 0/90 interfaces, the delamination crack propagates at

the distance h that results in the highest strain energy release rate. This can be found iteratively for any stacking sequence.

3.1.5 Stresses for Matrix Cracking/ Crazing

Crazing in one or more layers results from in-plane tensile stresses exceeding the local material strengths. Matrix cracking perpendicular to the fiber direction in the composite is a similar phenomenon. Several rigorous analyses predicting the onset and evolution of matrix cracking in both polymeric and ceramic matrix composites can be found in the literature [59-62]. However, a simplistic analysis based on a strength of materials criterion is probably adequate for preliminary design purposes. For our analysis, the *in situ* transverse strength is assumed to be independent of the ply thickness, although in practice, this may not strictly be true. For a unidirectional composite, the stresses in the transverse direction are considered as the strength is lowest in that direction. In each layer of a bilayer, the stress varies linearly across the thickness, and the extreme in-plane stresses act at the interface and at the outer ligament of each layer. These stresses are designated σ_{ji} and σ_{jo} (where j=1 or 2 according to the layer) respectively and are given by beam theory as [3]:

$$\sigma_{1i} = \xi\left[4\lambda\xi^3 + 3\lambda\xi^2 + 1\right]\beta \qquad [3.12a]$$

$$\sigma_{1o} = \xi\left(2\lambda\xi^3 + 3\xi^2\lambda - 1\right)\beta \qquad [3.12b]$$

If layer 1 (composite) is assumed to have a higher transverse CTE than the CTE of the metal, upon cooling P_1 is tensile and P_2 is compressive. Note that P_1 and P_2 are now perpendicular to the longitudinal direction. The peak tensile stress in the composite layer is then σ_{1i}. If, on the other hand, the composite CTE is lower, then σ_{2o} is the highest tensile stress in the composite. These stresses are plotted as a function of ξ in figures 3.11 and 3.12, for the same range of elastic mismatch as in the preceding sections. Composite properties in the longitudinal direction are considered for calculation of σ_{1o} and transverse properties are used for determination of σ_{1i}. An important observation is that in the second case σ_{1o} may be quite large and tensile, even though the mean stress is compressive. This is due to the effect of the bending moment acting on the layer [3, 15].

For laminate configurations other than unidirectional, the transverse stress in each ply needs to be calculated, and is best analyzed using CLPT [8].

3.2 FAILURE CRITERIA

In order to make use of the mechanics solutions presented in section 3.1, it is necessary to equate them to appropriate failure criteria. For the case of interfacial fracture, the steady-state strain energy release rate is equated to the adhesive toughness, $\mathcal{G}_{ic}$. The adhesive toughness is a function of mode-

mixity [14], and is obtained experimentally [63]. For delamination, the strain energy release rate is equated to the interlaminar toughness of the composite, which is also a function of the mode-mixity. For the case of matrix cracking, the transverse strength of the composite σ_T, which is assumed to be deterministic, is used. Both the strength and toughness may be obtained by conventional mechanical test techniques.

3.3 SHORT CRACK EFFECTS

For cracks not long enough to be in the steady-state, a higher load is required for propagation than for the steady-state case. Characterizing failure in these cases could be useful for detailed design. A solution for a thin film on a thick substrate has been provided by Akisanya and Fleck [64], using Eshelby-type superposition of stresses and numerically solving the simplified problem. The complex stress intensity at the crack tip is presented in terms of complex numerical coefficients for different thickness ratios and crack lengths.

Akisanya and Fleck's analysis was extended to case of thermal loading. Misfit stresses were calculated and used to compute stress intensity factors for representative geometries for different crack lengths. A plot of results for $t_1/t_2 = 0.1$ and 0.33 is displayed in figure 3.13 for a CFRP/aluminum lap joint.

It is seen from the graph that steady-state is reached within 4-5 times the composite thickness for both thickness ratios considered.

Table 3.1 List of values for Dundurs parameters for representative metals. A_1 and A_2 denote values of A with respect to 0° and 90° AS4/3501-6 graphite-epoxy respectively.

Metal	E	α(ppm)	A_1	A_2
Aluminum	70	24.1	.33	-.75
Titanium	125	8.5	.06	-.85
Iron	210	11.7	-.197	-.9
Molybdenum	275	5.4	-.32	-.93
Boron	400	3.1	-.48	-.95

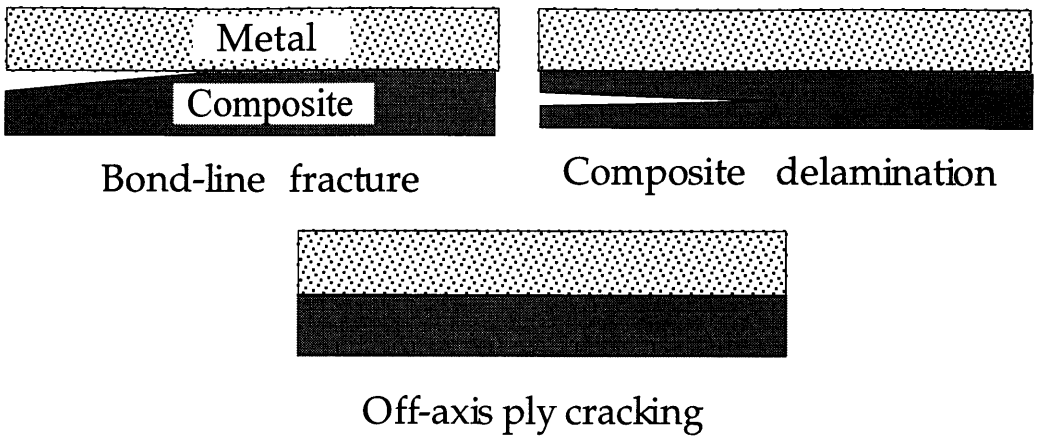

Figure 3.1 Failure modes of a composite-metal single lap joint

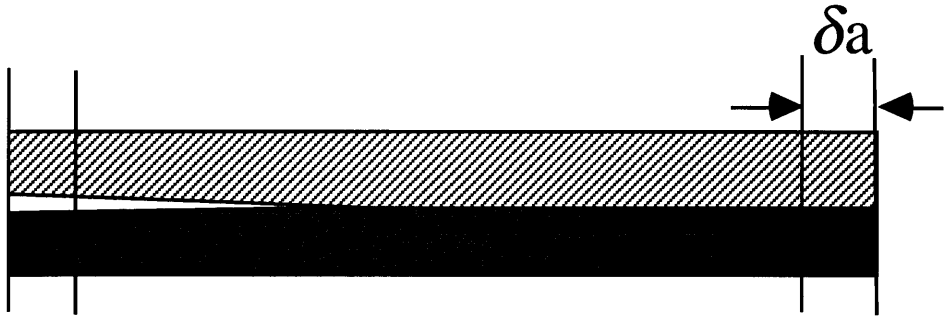

Figure 3.2 Illustration of control volumes far ahead and behind the crack tip

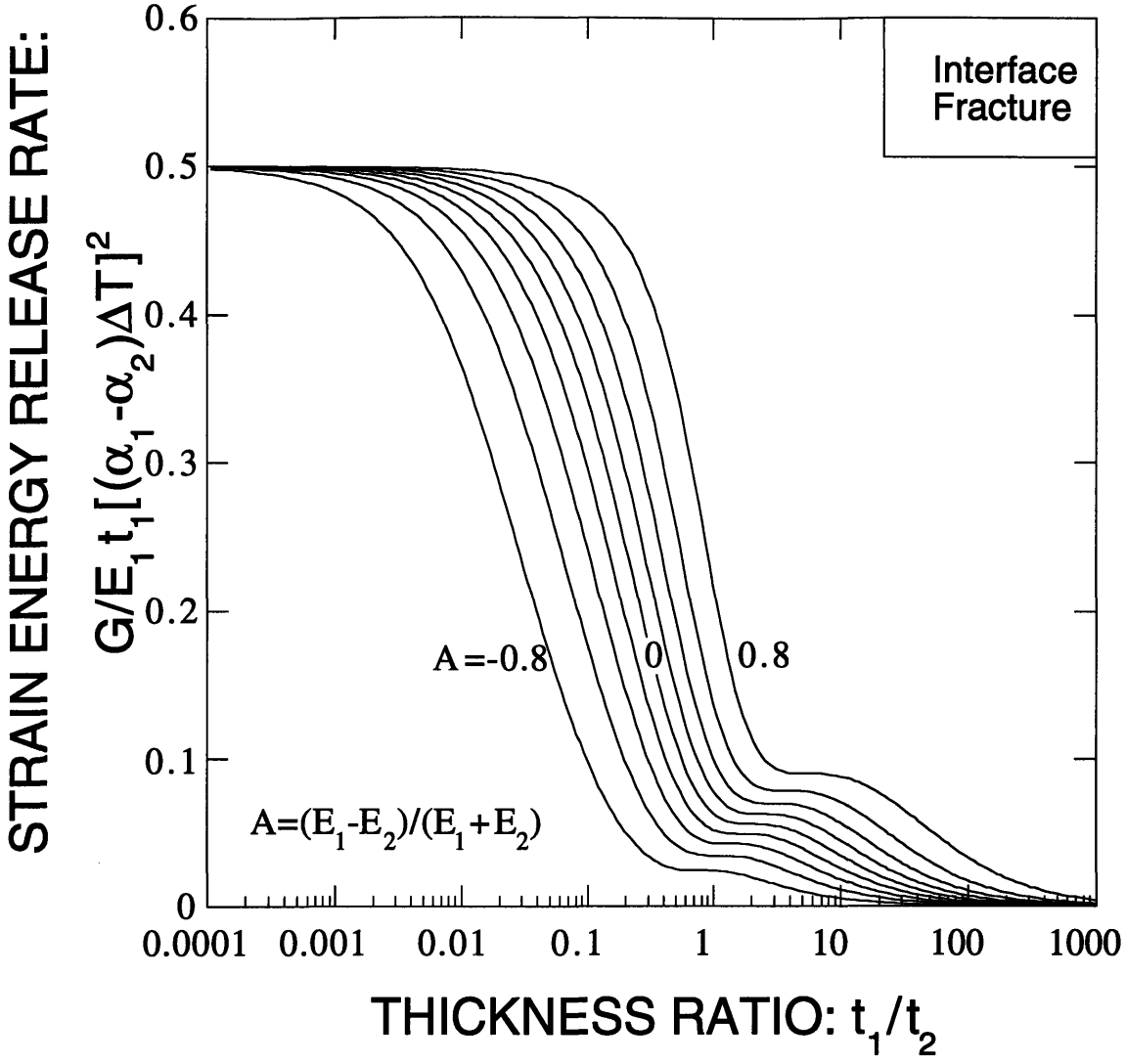

Figure 3.3 Strain energy release rate for single lap joint undergoing interfacial fracture

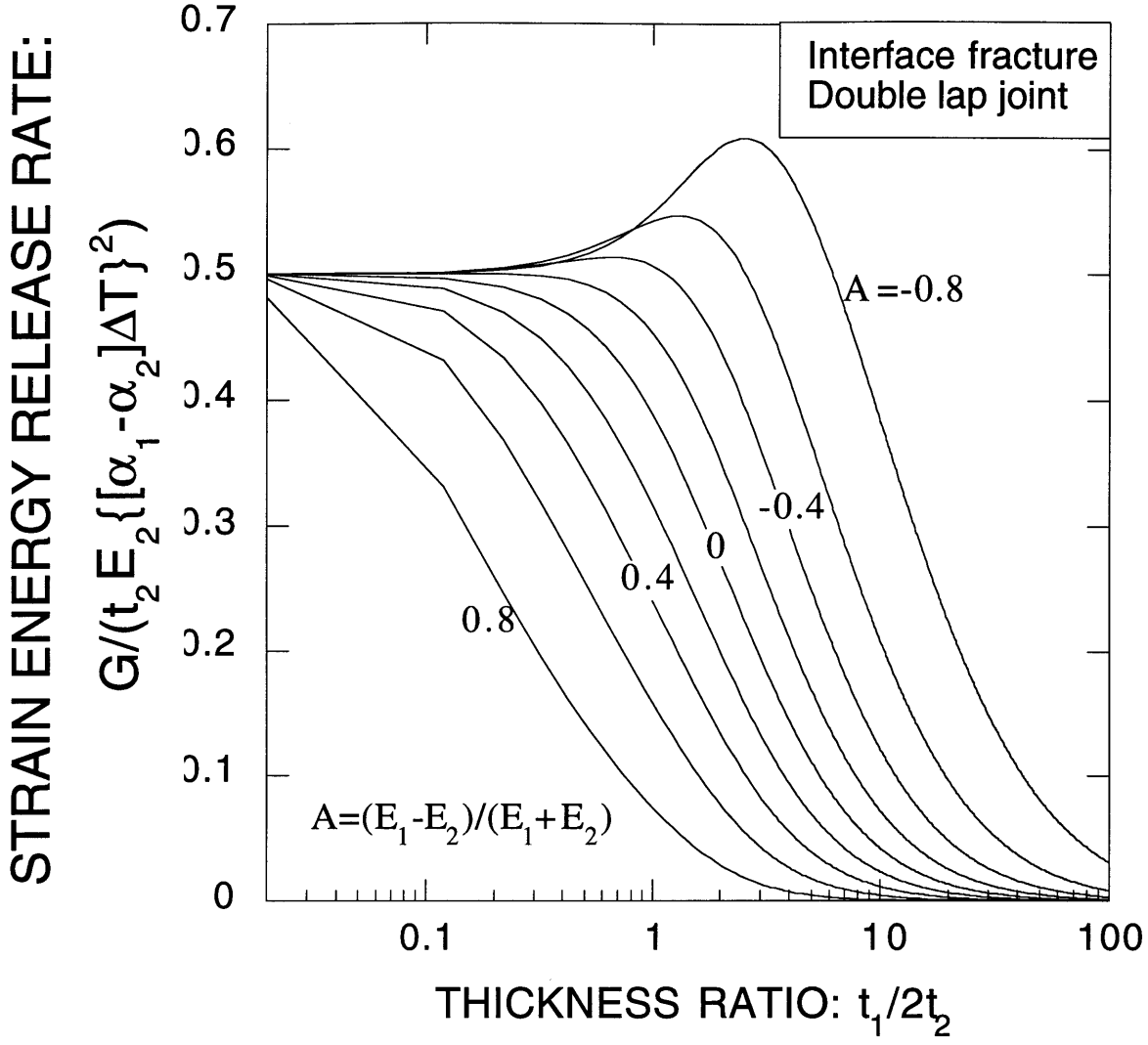

Figure 3.4 Strain energy release rate for double lap joint undergoing interfacial fracture

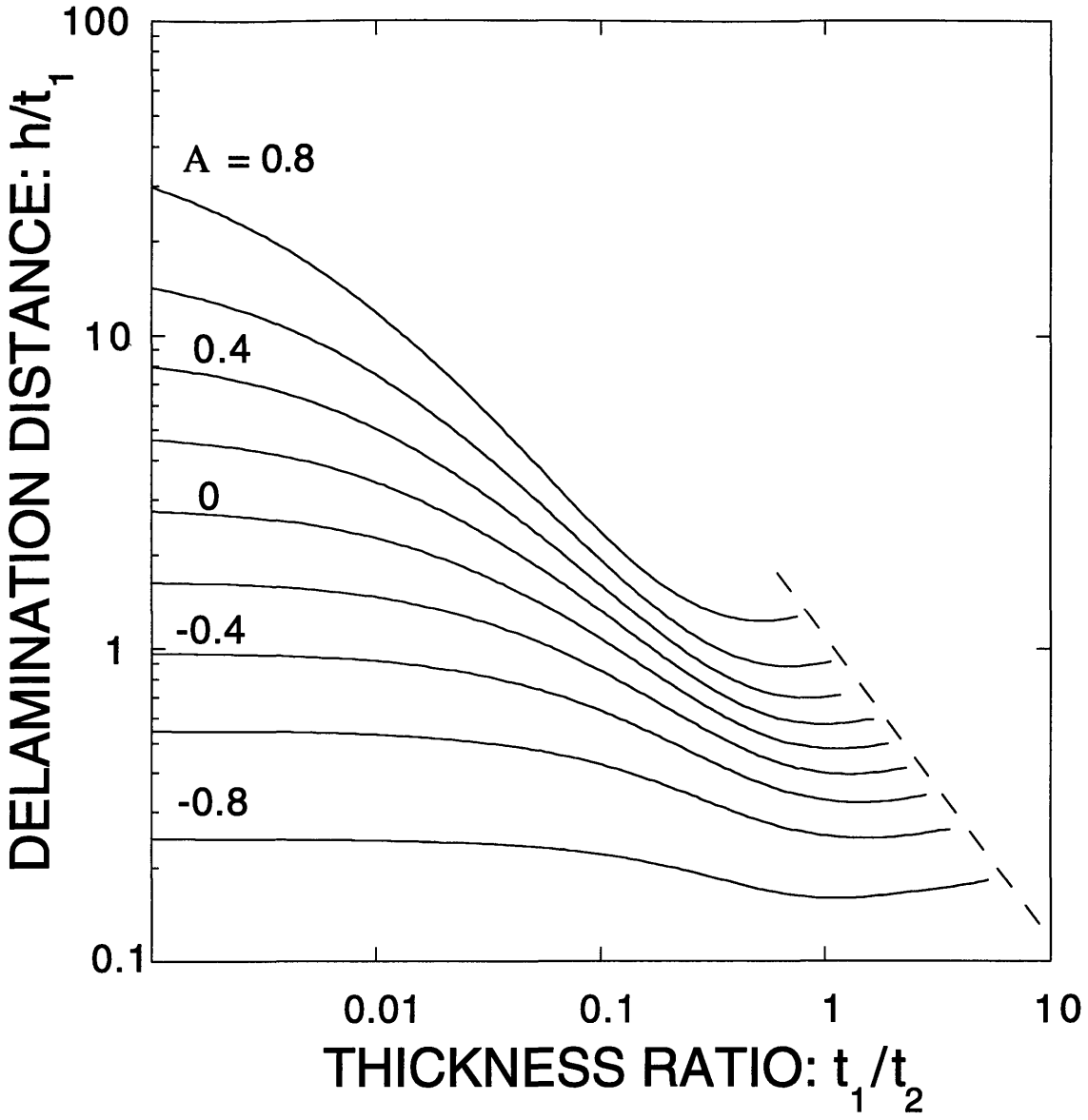

Figure 3.5 Delamination height (from interface) vs. thickness ratio for a single lap joint

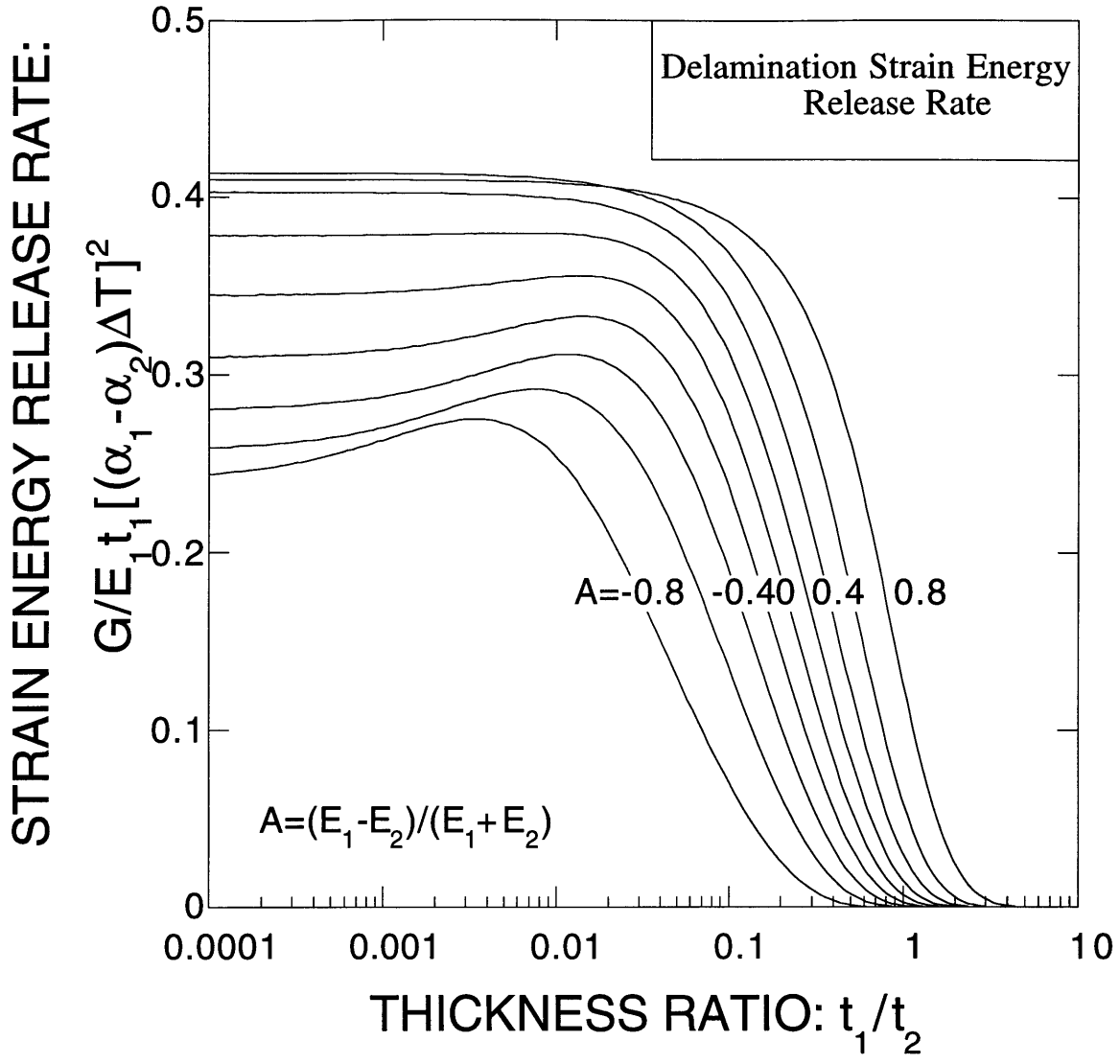

Figure 3.6 Strain energy release rate for single lap joint undergoing composite delamination

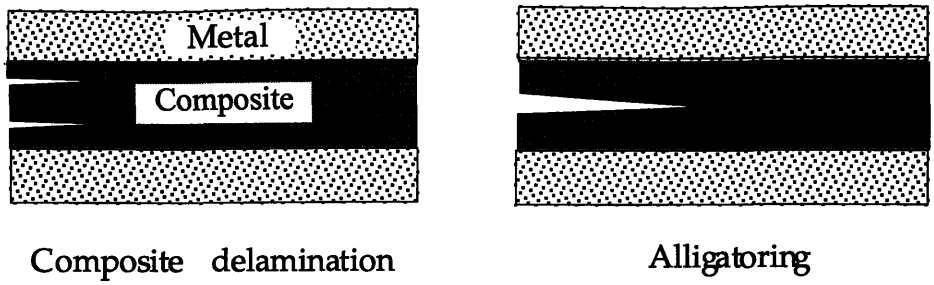

Figure 3.7 Illustration of delamination/alligatoring in a double lap joint

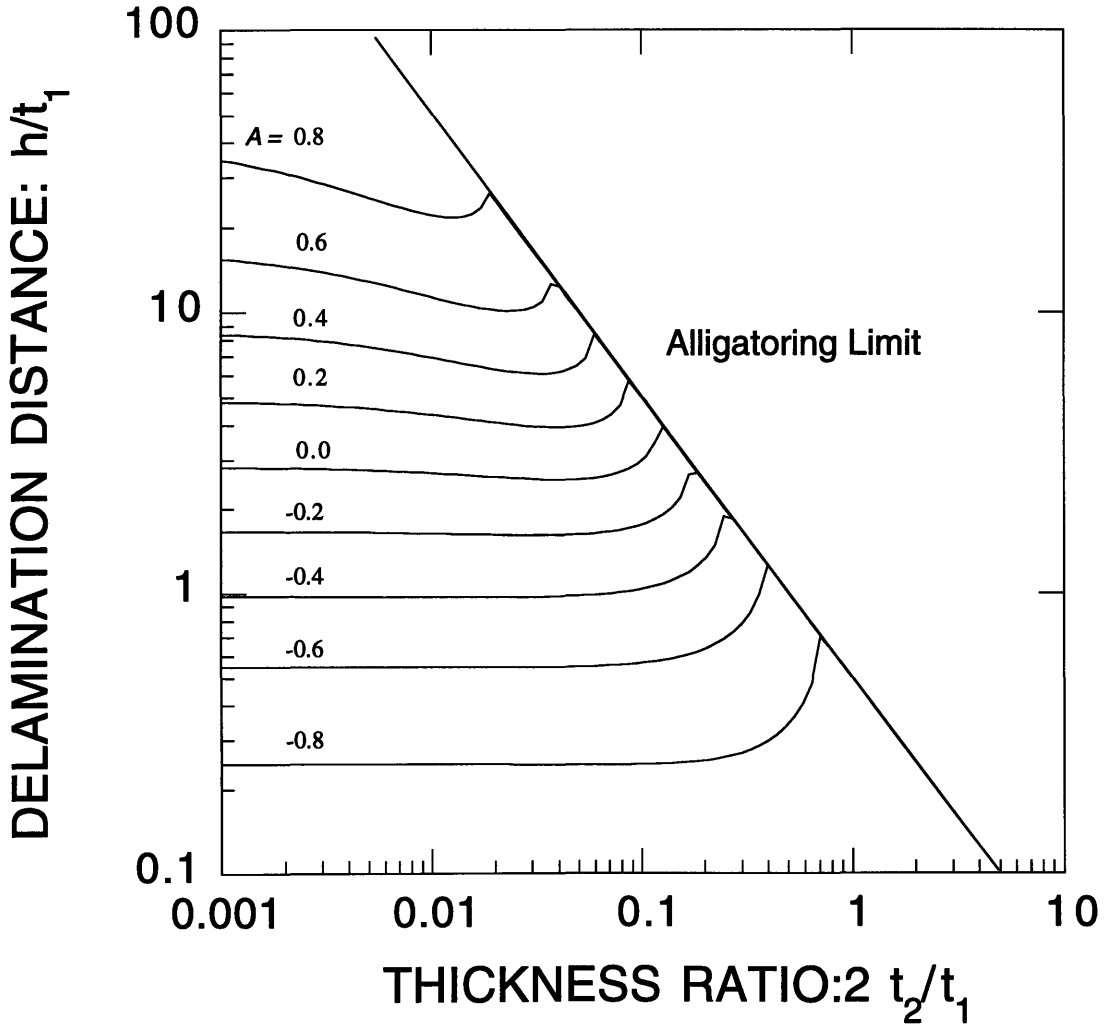

Figure 3.8 Delamination height (from interface) vs. thickness ratio for a double lap joint

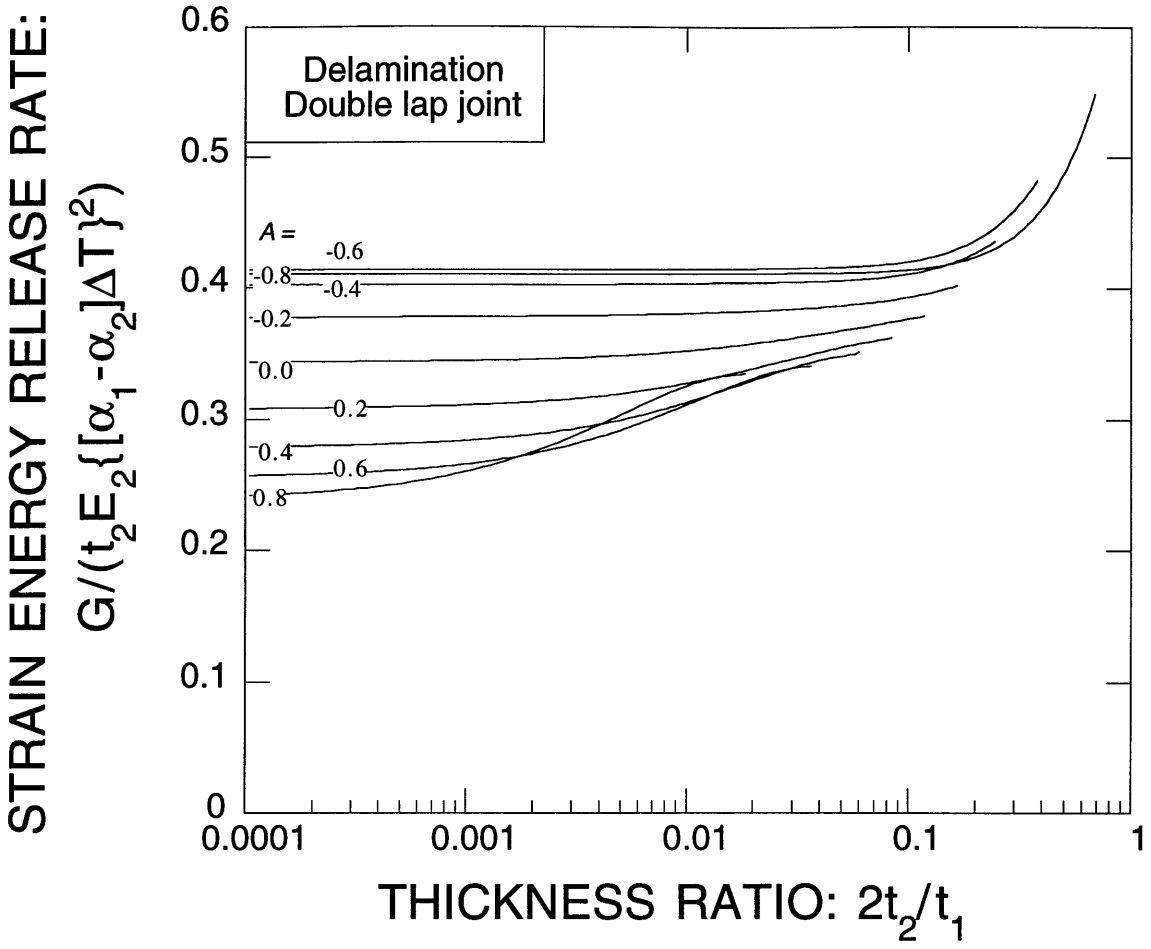

Figure 3.9 Strain energy release rate for double lap joint undergoing composite delamination

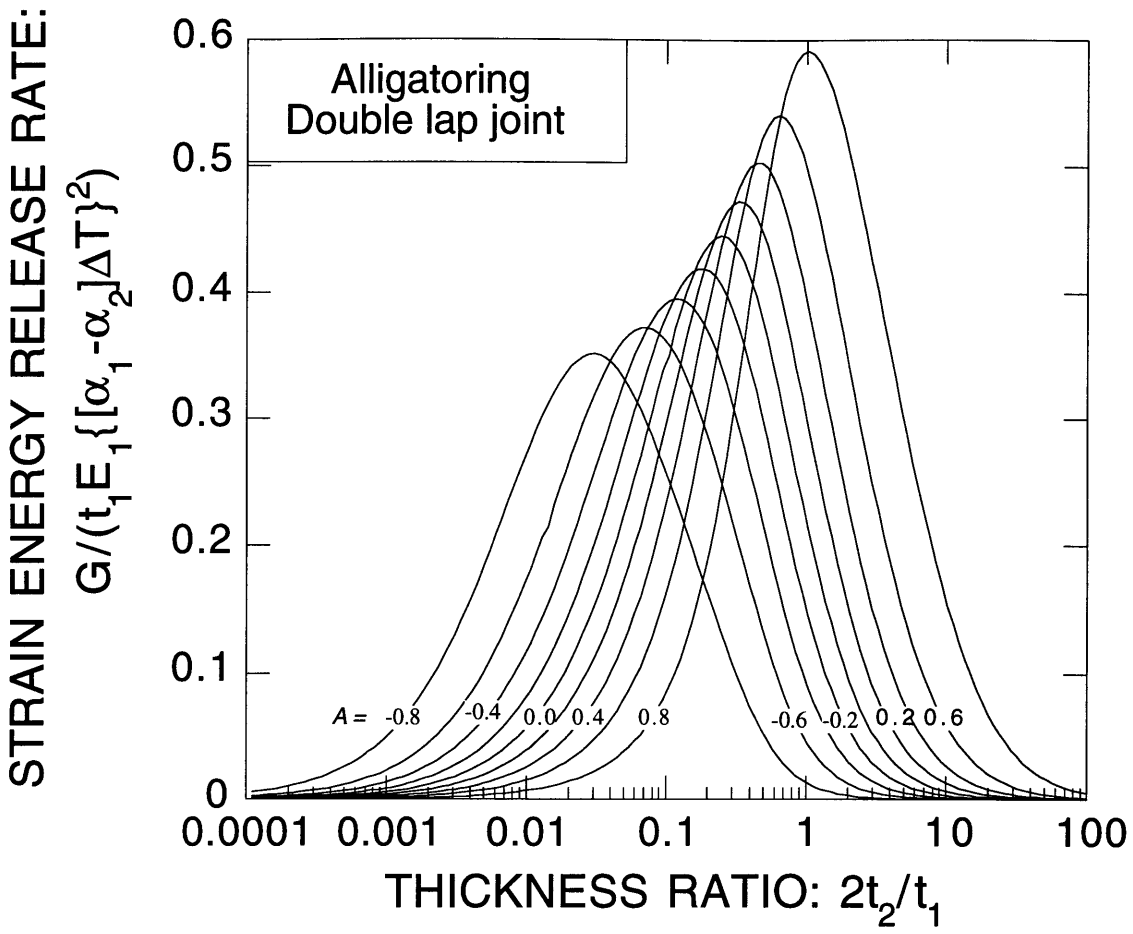

Figure 3.10 Strain energy release rate for double lap joint undergoing alligatoring

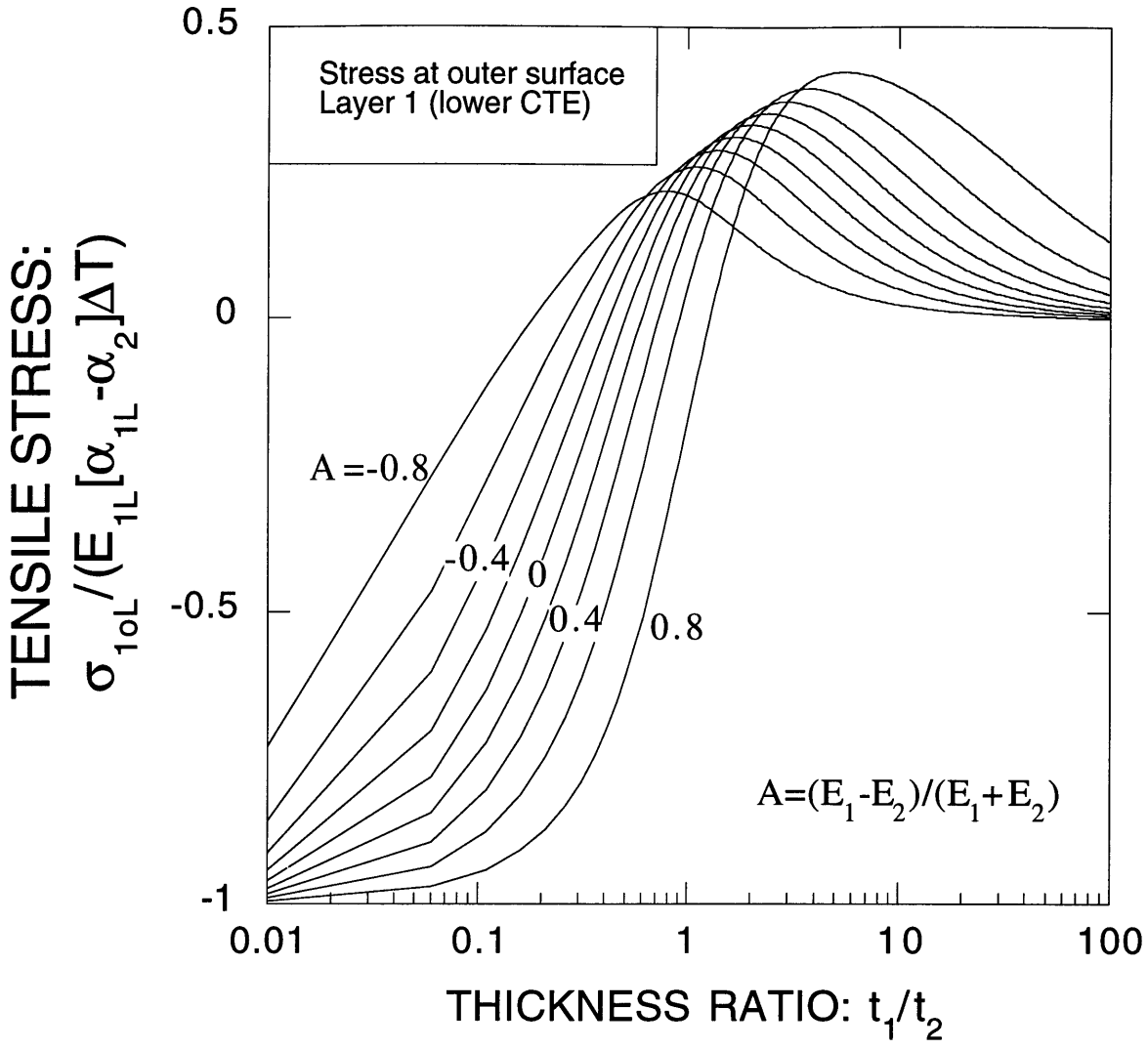

Figure 3.11 Maximum tensile stresses in layer 1 (0° composite) at the outer edge of the composite

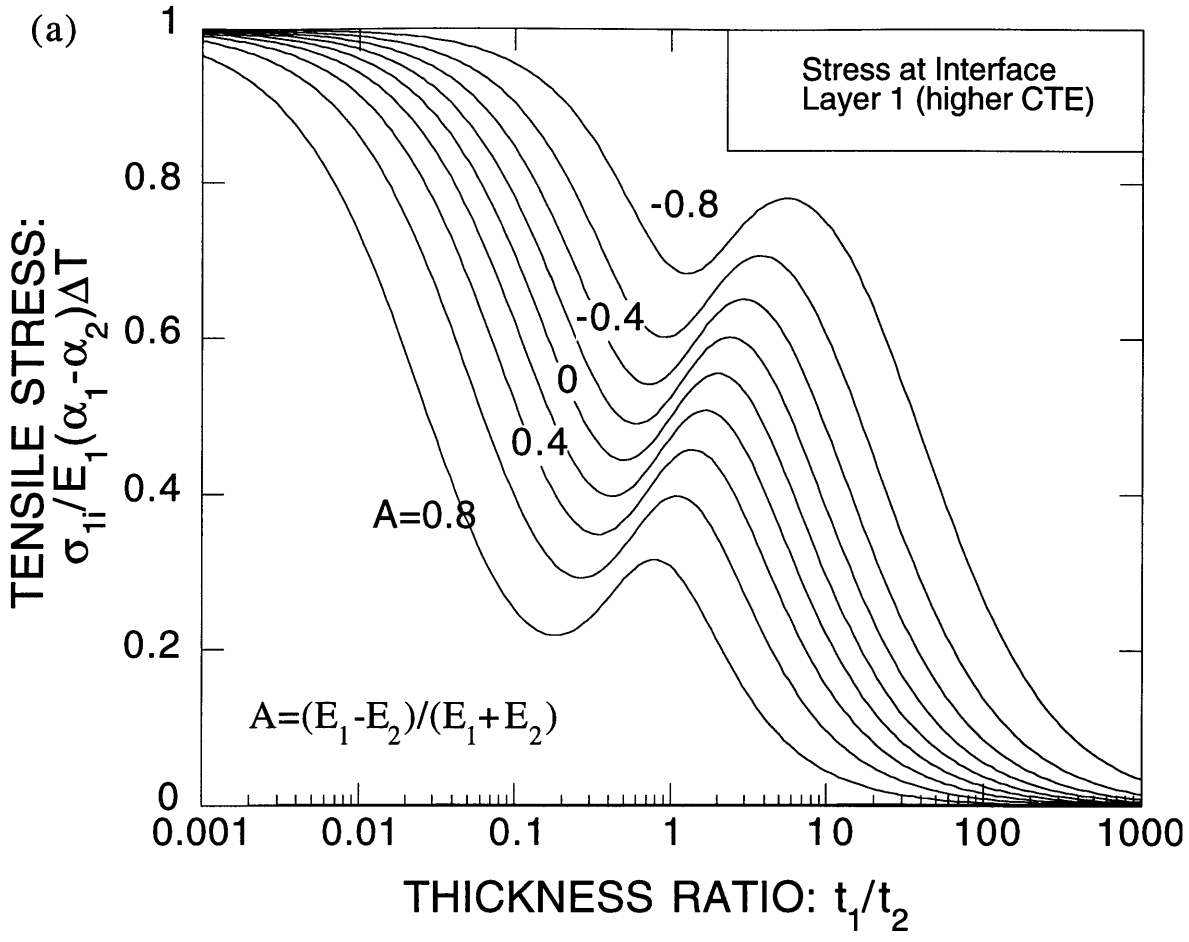

Figure 3.12 Maximum tensile stresses in layer 1 (90° composite) at the interface

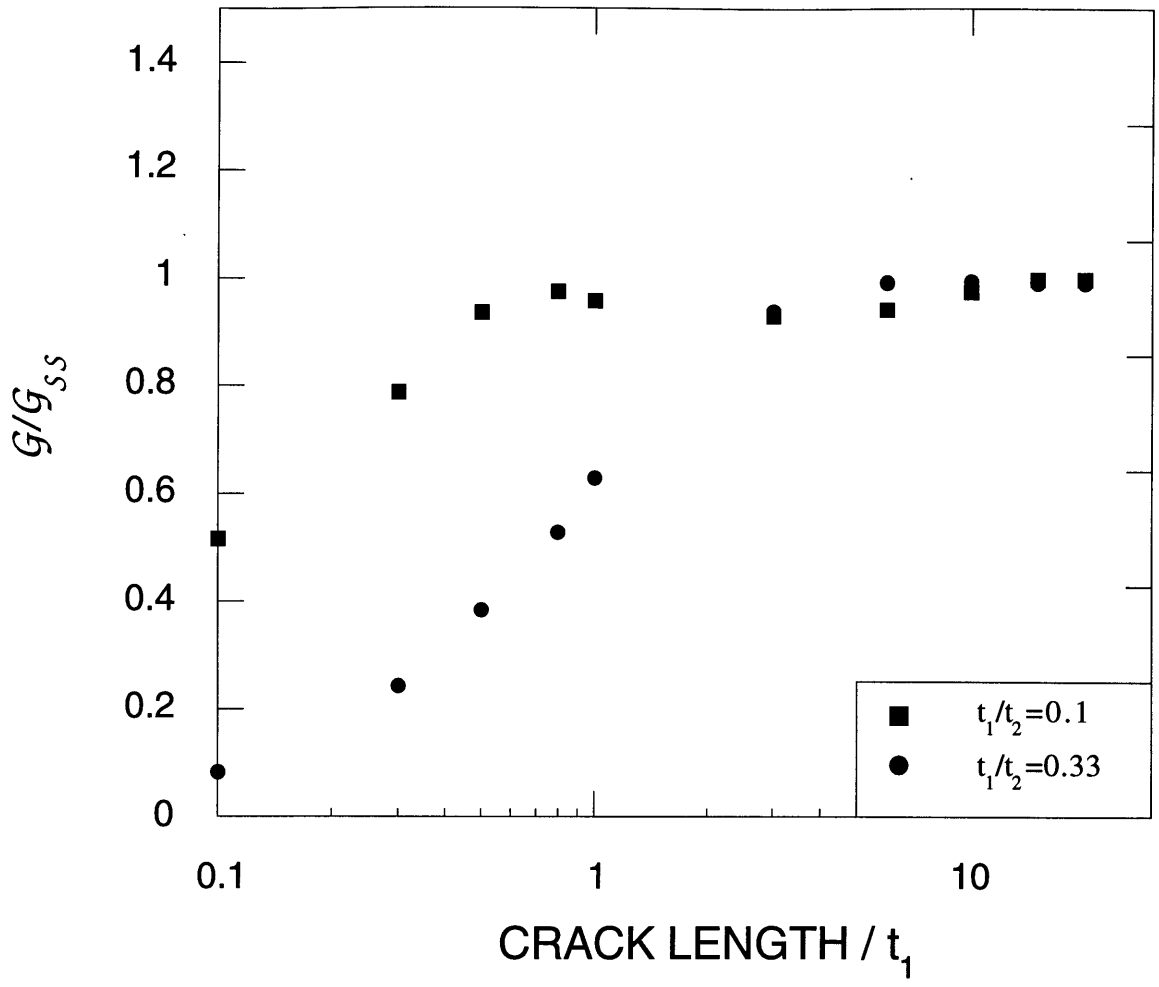

Figure 3.13 Non-dimensional strain energy release rate for two thickness ratios as a function of crack length

CHAPTER 4

EXPERIMENTAL METHOD

As seen in the previous chapter, steady state fracture mechanics solutions have been formulated to predict loads to failure in terms of material properties, configuration, and thickness ratio. A thermal testing program on metal-composite joints was conducted at the Technology Laboratory for Advanced Composites (TELAC) at MIT to verify the theoretical predictions. In parallel, adhesive fracture tests were conducted to attempt to link results obtained in purely mechanical loading with those obtained in thermal loading. This chapter provides a description of the test procedures. In order to compare different material systems, a study was also conducted on bilayers of a ceramic bonded to a ceramic matrix composite.

4.1 THERMAL TESTING

The basic approach was to fabricate specimens consisting of two dissimilar materials bonded at the interface between them. Thermal loading was applied by cooling the specimens below the bonding temperature in order to study the fracture behavior.

4.1.1 Specimen Fabrication/ Materials

Single and double composite-to-metal lap joints were used for this purpose. The specimens were of two types, non-precracked and precracked.

4.1.2 Non-Precracked Specimens

Strips of 6061-T6 aluminum were bonded to AS4/3501-6 graphite-epoxy composite. The materials and thicknesses were chosen so as to obtain a range of thermal loads to cause failure. The composite thickness was kept constant at 2 mm, while the aluminum thickness was varied to give composite-aluminum thickness ratios between 0.42 and 3.16. The composite was manufactured as a 30.5 cm x 35.5 cm panel using 16 unidirectional plies in a $[0]_{16}$ configuration. The plies were cut from prepreg tape manufactured by Hercules, laid up, and the cure was performed at 380 K for 1 hour and 450 K for 2 hours following a standard procedure [65]. After postcure, the composite was cut into 117 mm x 30 mm strips on a milling machine. The aluminum was cut into strips with identical planforms using a bandsaw and sanded for a smooth finish.

Surface preparation of the metal for the bond cure consisted of light abrasion with garnet paper and subsequent solvent cleaning. The peel ply applied to the composite laminate during curing [65] provides a roughened surface which was adequate surface preparation for the graphite/epoxy. FM

123-2 film adhesive (Cytec) was used. The adhesive contains a glass fiber scrim, to provide strength to the uncured adhesive film during handling. The cure was performed at 380 K for 2 hours under 102 kPa autoclave chamber air pressure. A vacuum was maintained on the assembly throughout, to eliminate gas entrapment and voiding.

After curing, the specimens were sanded to eliminate the excess adhesive from the edges of the lap joint. The curvatures of the single lap joints were measured, using a DEKTAK 8000 profilometer. The profilometer employed a mechanical probe that measured displacements along the length of the specimen. This was done in order to compare with beam theory predictions (made assuming that the stress state was linear), as described in chapter 3.

4.1.3 Precracked Specimens

Specimens were manufactured with pre-cracks in order to ensure steady state fracture, rather than short crack behavior. Similar specimens were used as for the non-precracked case, but included a wider range of material properties and specimen thicknesses. Single and double lap joints were manufactured using aluminum (6061-T6) or steel (AISI 01) bonded to AS4/3501-6 graphite/epoxy unidirectional and cross-ply composite. The laminates consisted of 16 or 32 plies, giving a laminate thickness of 2 or 4 mm. The metal thickness was varied between 1.6 and 16.4 mm. The reason

for using two different metals was to change the mismatch in thermal and elastic properties and thus the thermal load to cause failure for the same composite thickness. The composite thickness was doubled for the same aluminum thicknesses to validate the total thickness dependence for the same thickness ratio. Also, the composite configuration was varied in order to observe different failure modes, and to use more realistic laminates. Table 4.1 lists the thermomechanical properties of the materials used. Table 4.2 is the test matrix of precracked specimens, showing the different combinations described above.

The composite was manufactured in the form of panels as before, and milled to form strips 140 mm x 25 mm. The fabrication procedure was the same as for the non-precracked specimens, except for the 25 mm precrack at one end of each specimen. The precrack was created by spraying the metal surface on one end of each specimen using (MoldWiz™ F-57 NC). Figure 4.1 is an illustration of the geometry of a typical specimen.

4.1.4 Test Procedure

The thermal test specimens were placed in a liquid nitrogen-cooled thermal cycling chamber which had a low temperature limit of 85 K. The specimens were cooled at a nominal rate of 7 K/min and brought back to room temperature, at which point they were examined for signs of fracture under an

optical microscope. The minimum temperature change after which fracture was first observed was noted as the critical temperature.

4.2 MECHANICAL TESTING

The mechanical tests were conducted in order to obtain mode I and mode II fracture data which could be used to bound the mixed-mode fracture toughness value for the adhesive. This mixed-mode value could then be used to fit the thermal test data.

4.2.1 Specimen Fabrication And Materials

Double cantilever beam specimens were used to obtain mode I fracture data. The test was carried out according to ASTM standard D 3433 - 93 [51], with the exception that a shorter specimen length was used (152 mm vs. 356 mm). The specimen geometry, shown in figure 4.2, consists of flat adherend 6061-T6 aluminum bars 152 mm in length, 25.4 mm wide and 12.7 mm thick. A 25 mm precrack was manufactured into the specimen. The decision to perform the test using aluminum adherends was taken after observing that fracture initially initiated at the adhesive-aluminum interface (details are provided in the next chapter).

For Mode II testing, in the absence of a recognized standard, specimens similar to those used for end-notch flexure (ENF) testing of polymer matrix

composites were used [66]. The specimen geometry used was the same as that for the DCB tests, except that the specimen was precracked to about 50 mm (vs. 25 mm for the mode I specimens) from one end. This geometry conformed to the design requirements specified in [67] for ensuring material linearity and small deflection behavior. The specimens were machined to increase the separation between the two faces in the pre-cracked region (see figure 4.3). This reduces the error in the calculated fracture resistance caused by friction between the crack faces.

Bar stock of 6061-T6 aluminum was cut into 152 mm lengths. Surface preparation of the specimens and the pre-cracking technique used were the same as for the thermal testing specimens (section 4.1.3). The cure procedure followed was also the same as before, and is described in 4.1.3.

4.2.2 Test Procedure

For mode I testing, the fixture used for mounting the specimens on the testing machine was designed such that the applied load is always perpendicular to the specimen mid-plane. The loading arrangement is depicted in figure 4.4. Holes of diameter 6.35 mm were drilled through the specimen in order to insert the steel pins (see figure 4.2). Mode II testing utilized a three-point bending fixture, as shown in figure 4.5. The tests were performed on a 100 kN capacity MTS™-810 testing machine. Data were collected using Labview™ data acquisition software. The tests were

performed in displacement control at a rate of 0.01 mm/s throughout, which ensured fracture in approximately one minute. Data sampling was at a frequency of 2 Hz. A traveling microscope was used to monitor crack extension.

4.3 FRACTURE IN CERAMIC MATRIX COMPOSITES/ CERAMICS

In joints between two brittle materials, both materials as well as the interface may fracture, in contrast to metal-composite joints where the metal is unlikely to fracture [68]. As a result, a variety of failure modes can occur in bilayers of ceramics and CMC's, including spalling and crazing, as described in chapter 3. For comparison, specimens of CMC-ceramic bilayers were obtained and the failure modes observed.

Bilayers of alumina bonded to unidirectional Nicalon-reinforced calcium aluminosilicate (CAS) were examined for fracture. The specimens were manufactured at Corning by hot pressing the composite prepreg, to densify and to form a bond with the alumina. Subsequently, the matrix is devitrified by heat treatment to leave a glass ceramic matrix. The devitrification temperature is approximately 900K. The specimens were of 2 thicknesses; the alumina was 0.65 mm and 0.5 mm thick and the composite was 0.65 mm and 1.5 mm thick respectively.

4.4 FRACTOGRAPHY

After the thermal testing was conducted on the metal-composite specimens, representative specimens were cross-sectioned for detailed observation of the fracture surface. A scanning electron microscope (SEM) was used for this purpose. Prior to observation under the SEM, the sacrificial specimens were gold-plated in order to make them conductive. Chapter 5 provides details of the observations made.

The ceramic/CMC specimens were cross-sectioned using a medium speed diamond wafering saw and mounted in epoxy. They were then polished, starting with a 30 micron grinding wheel, down to 1 micron using diamond paste. They were then examined under a high-resolution optical microscope and photographed.

Table 4.1: Thermomechanical properties of adherends

	Aluminum	Steel	UD CFRP
E_L (GPa)	70	200	141
E_T (GPa)	70	200	10
ν_{LT}	0.3	0.3	0.32
α_L (ppm/K)	24	11	-0.5
α_T (ppm/K)	24	11	30

Table 4.2: Test matrix of precracked specimens

	AS4/3501-6 graphite-epoxy composite			
	$[0]_{16}$	$[0]_{32}$	$[0_4/90_4]_s$	$[0]_{16}$ (2 sided)
Aluminum (t_1)	3	3	3	3
Aluminum (t_2)	3	3	3	3
Aluminum (t_3)	3	3	3	3
Aluminum (t_4)	3	3	3	3
Steel (t_1)	3	-	-	-
Steel (t_2)	3	-	-	-
Steel (t_3)	3	-	-	-
Steel (t_4)	3	-	-	-

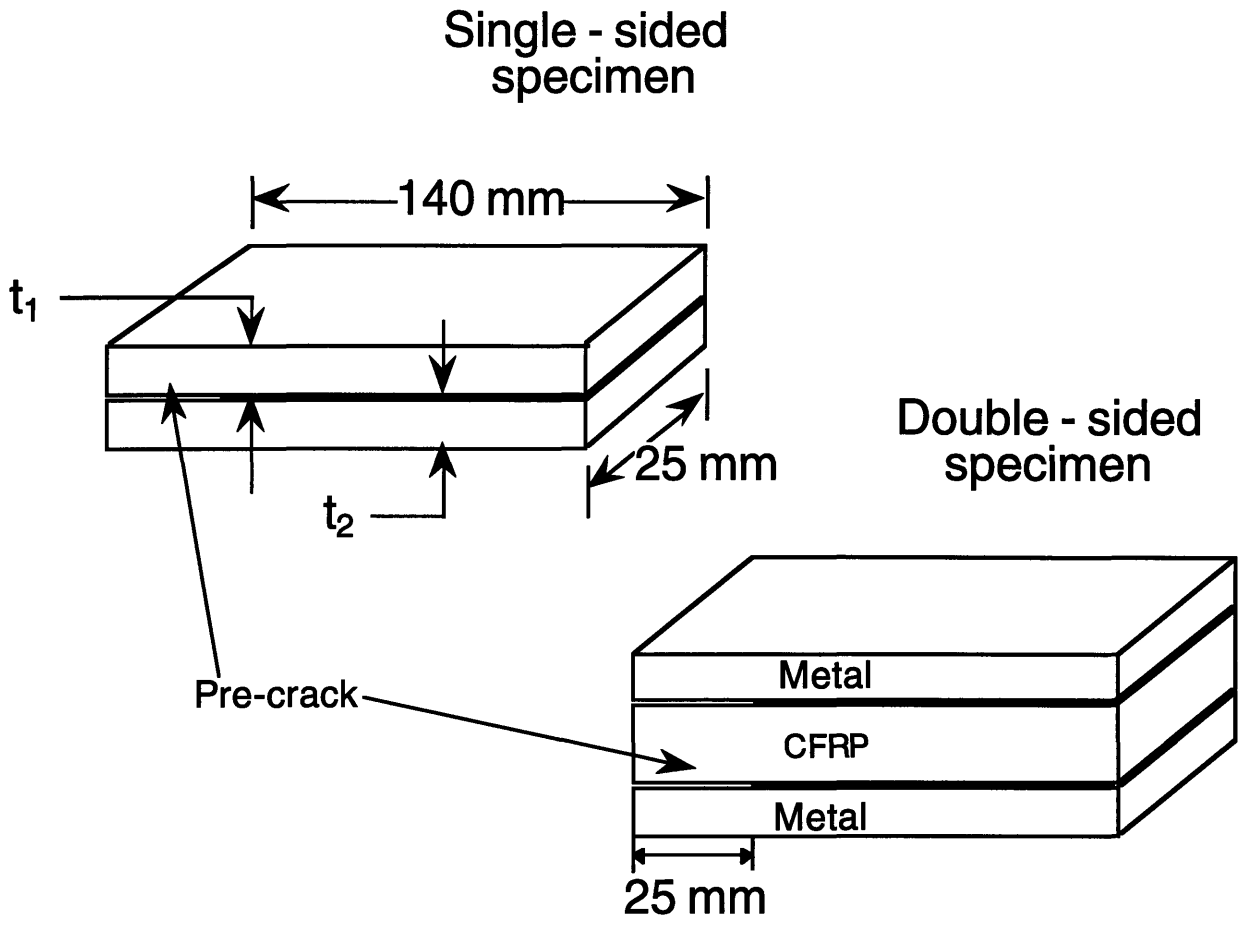

Figure 4.1 Typical specimen geometry for thermal testing experiments (note: not drawn to scale)

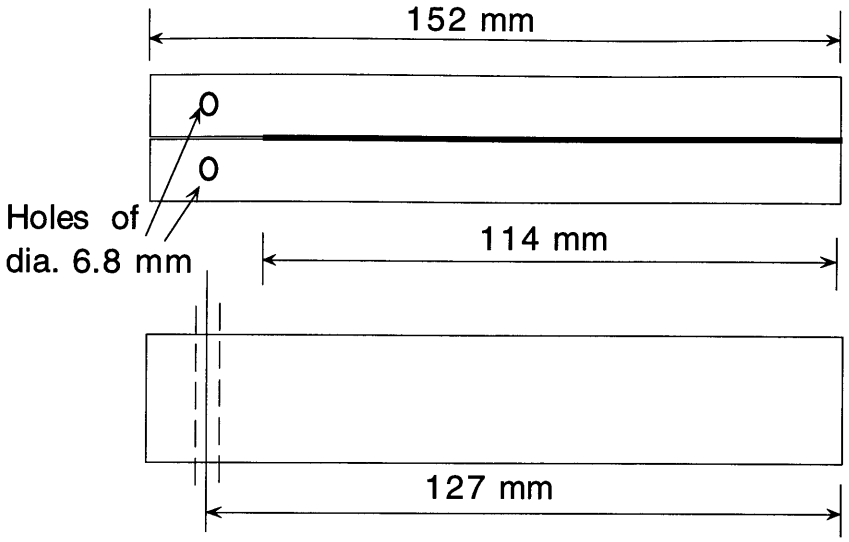

Figure 4.2 Specimen for mode I fracture testing experiments

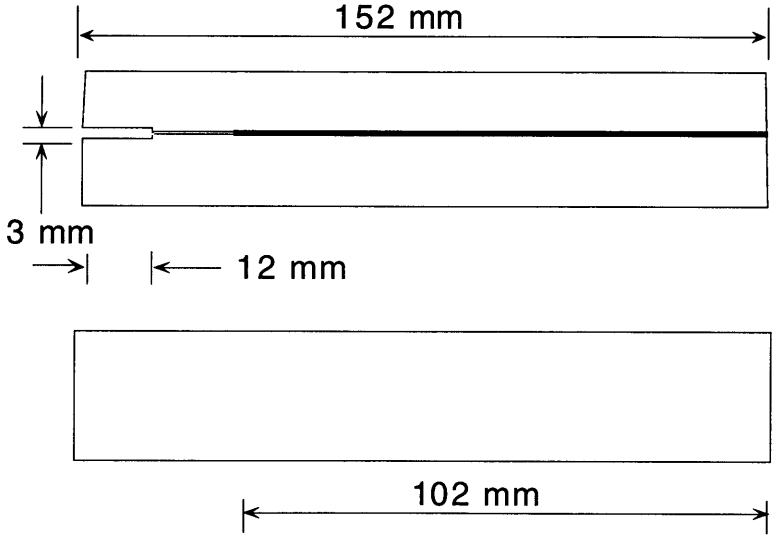

Figure 4.3 Specimen for mode II fracture testing experiments

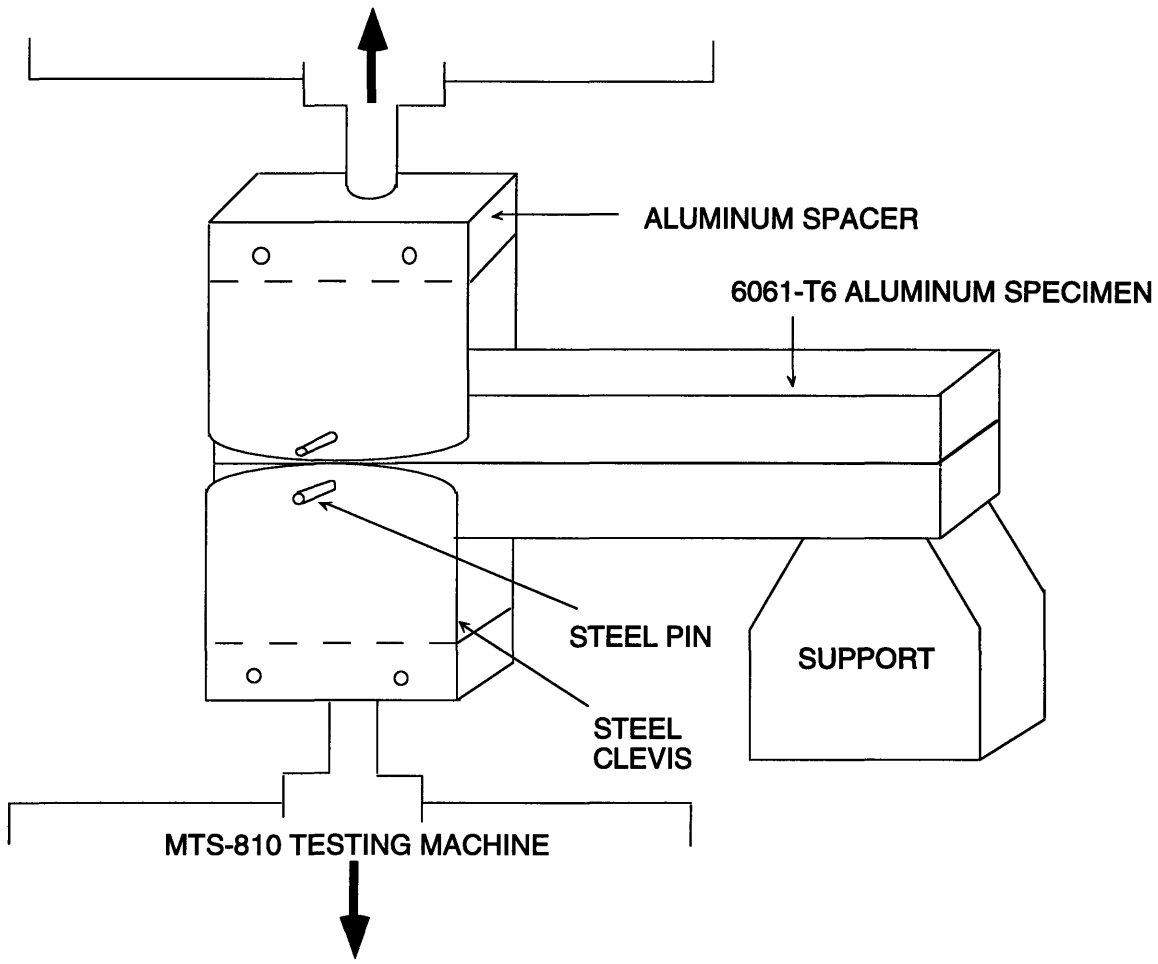

Figure 4.4 Testing configuration for mode I fracture data

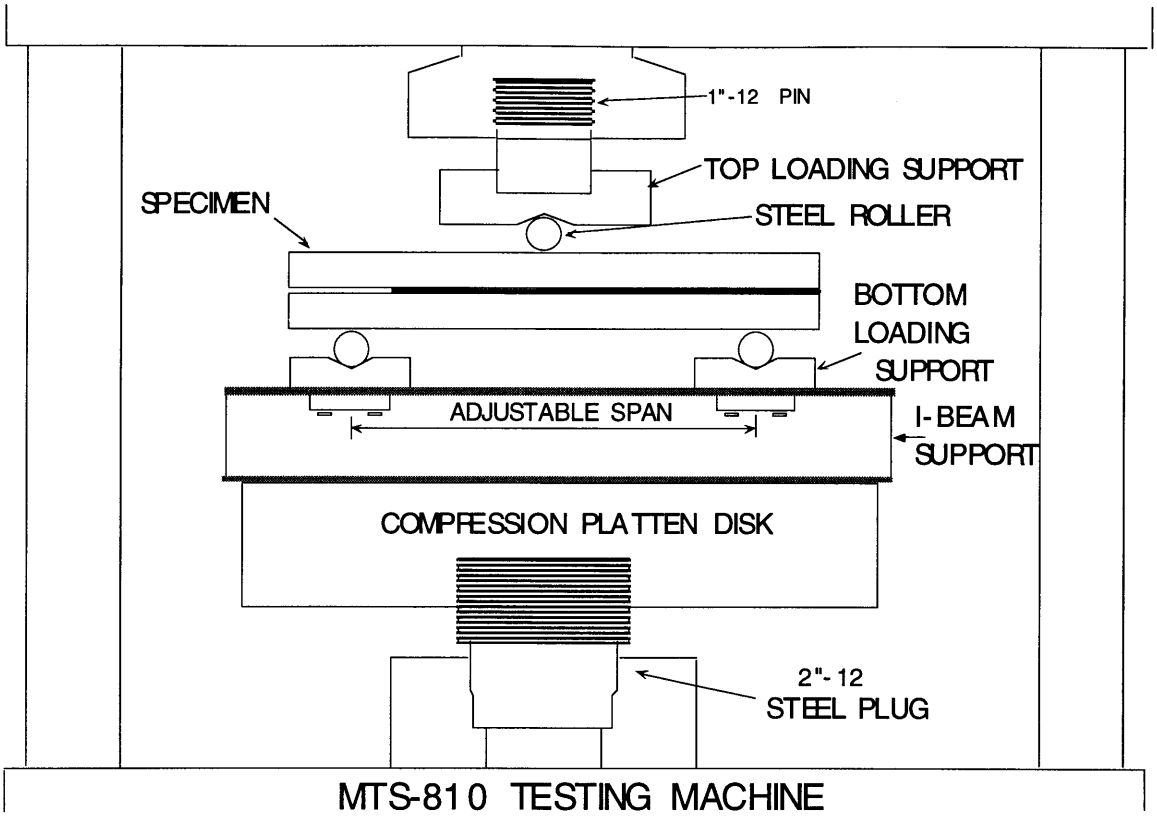

Figure 4.5 Testing configuration for mode II fracture data

CHAPTER 5

OBSERVATIONS AND RESULTS

In this chapter, the results from the thermal and mechanical testing experiments described in chapter 4 are presented. Observations of fracture paths in both metal-composite and ceramic-CMC joints are also described.

5.1 THERMAL TEST RESULTS

This section describes observations made prior to testing, but after the composite-metal bonded joints were taken out of the autoclave. Data from the thermal tests are then presented.

5.1.1 Pre-Testing Observations

The metal/composite single lap joints were noticeably curved after they were subjected to the cure temperature drop of 107 K. Since the composite has a lower longitudinal coefficient of thermal expansion than the metal for all configurations tested, the metal contracted more in the longitudinal direction in all cases. This caused the specimens to curve with the composite on the convex side. A plot of measured curvature vs. thickness ratio of the

composite to the metal is shown in figure 5.1. Also plotted are curvatures predicted from elastic beam theory (equation 3.3). From the graph, it is seen that elastic beam theory is able to predict curvatures fairly accurately. It is also noted that the maximum stress in the metal was found to be below the corresponding yield stress in all cases (e.g. maximum stress in the aluminum was found to be less than 70 MPa, less then half its estimated yield strength). This was another justification for the use of linear beam theory.

The double lap joints had, in most cases, undergone debonding of one metal-composite interface, due to the loading induced by the cure temperature drop. The extent of debonding varied from specimen to specimen. The intact specimens had zero curvature, as expected due to their symmetry.

5.1.2 Fractography

The thermal testing resulted in a variety of failure modes. In all cases, fracture initiated at the composite-metal bondline. In the cross-ply specimens, delamination and matrix cracking subsequently occurred. The pattern of interfacial debonding was identical in all cases; the fracture always initiated at the metal-adhesive interface and then crossed over to the composite-adhesive interface. Thus, the mode of fracture was adhesive (i.e. the crack follows the adherend-adhesive interface) rather than cohesive (i.e. the crack lies within the adhesive layer). The fracture path is illustrated in figure 5.2a. Figure 5.2b is an SEM micrograph of the transition region, where

the interfacial crack crosses between interfaces. Figure 5.3a is a close-up of the transition region in the adhesive, showing the exposed scrim fibers. Figure 5.3b is a micrograph of the relatively smooth adhesive fracture surface far away from the transition region.

5.1.3 Non-precracked Thermal Tests

In the first stage of thermal testing, in which the specimens were not precracked, all the specimens failed by interfacial debonding. Figures 5.4 and 5.5 show experimental data for the change in temperature to cause fracture as a function of composite-to-aluminum thickness ratio for single and double-sided specimens respectively. Curves of predicted fracture temperature for fixed values of adhesive fracture resistance are also plotted. In the case of the double lap joints, some of the specimens were observed to have undergone fracture at one interface as they cooled from the cure temperature, as mentioned in 5.1.1. This is indicated by arrows in figure 5.5. Thus, double lap joints are more prone to interfacial fracture than single lap joints, as was expected (refer chapter 3). It is seen that trends in critical temperature drop to cause fracture are correctly predicted, but the scatter in data is considerable. The scatter may be attributable to the fact that not all the specimens undergo steady state fracture; in some cases, the initiation, or short crack behavior dominates the fracture process.

5.1.4 Pre-cracked Thermal Tests

The data from the second stage of thermal testing together with steady-state fracture predictions are plotted in figures 5.6-5.10. It is apparent that the scatter in data is reduced compared to the unprecracked specimens. Figures 5.6 and 5.7 are for a similar range of thickness ratios as figures 5.4 and 5.5 respectively. It is seen that the trends observed in the data are captured by the steady-state fracture mechanics model, and that the predicted fracture temperature drop curves may act as lower bounds. However, no single value of adhesive toughness is adequate to characterize the data. The apparent toughness of the joint increases as the aluminum thickness is increased. Figure 5.8 shows test data for $[0]_{32}$ graphite/epoxy-aluminum specimens. The thickness effect predicted by the model is clearly evident in this plot, as critical temperatures for fracture are less than those for specimens with $[0]_{16}$ composite, for the same thickness ratios.

The experimental trends for steel/composite specimens are similar to those for aluminum/composite specimens, as seen in figure 5.9. The closer CTE match leads to greater temperature changes to cause failure. One set of specimens, corresponding to the maximum thickness ratio (t_c/t_{st}), remained intact even when subjected to the maximum temperature drop achievable in the chamber. This is as predicted by theory for an adhesive fracture toughness of 400 J/m^2.

Figure 5.10 shows data for aluminum/$[90_4/0_4]_s$ graphite-epoxy specimens. Here, delamination is the predominant failure mode according to steady-state fracture predictions, as seen in figure 5.10. In practice, the crack initially propagates at the bondline between the composite and metal, continuing from the starter crack, and then kinks into the 0/90 interface as a delamination. This behavior is captured in figure 5.11. Thus the failure mode was correctly predicted; the data follows the trends as for other configurations. It should be noted that the predictions were very conservative, and the effect of thickness was less than expected.

5.2 MECHANICAL TEST RESULTS

The mechanical tests generated some interesting results in addition to substantiating the adhesive toughness values used to fit the thermal test data. A fracture resistance curve was obtained from mode I and mode II tests [63]. This fracture behavior has not been reported in the adhesive literature. Details about the same will be provided in this section.

5.2.1 Mode I Tests

In the DCB tests, a load drop was observed at every crack extension. A typical load vs. time profile is shown in figure 5.12. The maximum load just before crack extension was recorded as the critical load for that crack length

(crack length was measured from the point of loading). The mode I fracture toughness, G_{Ic}, was calculated using [51]

$$G_{Ic} = \frac{[4L^2(\max)][3a^2 + h^2]}{E.B.h^2} \qquad [5.1]$$

where L(max) is the critical load corresponding to a crack length a. B and h are the width and height of the specimen respectively, and E is the Young's modulus of the adherend material. The elastic properties and thickness of the adhesive layer are ignored in this calculation.

The fracture in the mode I tests was found to be cohesive [69] (i.e. the crack ran predominantly through the adhesive rather than at the interface between the adhesive and metal), and the crack growth was stable. The reduced data from these tests are plotted in figure 5.13. It is observed that the mode I fracture toughness is not a unique value, but increases with crack length, thus demonstrating resistance curve (R-curve) behavior.

5.2.2 Mode II Tests

The data from the mode II tests are plotted in figure 5.14. R-curve behavior is clearly evident, and is more pronounced than in the DCB tests. The tests were interrupted before the specimens reached maximum crack extension, and this resulted in a marked decrease in fracture resistance,

possibly due to the breaking of bridging fibers during unloading. The initiation value of G_{IIc} is approximately 900 J/m^2 compared to a value of only 100 J/m^2 for G_{Ic}. The friction component in the mode II tests was not completely eliminated and it is unclear as to how much this affected the results.

5.2.3 Fractography/ Observations

The mechanism responsible for this observed R-curve behavior is clearly apparent from inspection of the fracture surfaces. Figures 5.15a and 5.15b are SEM micrographs of the fracture surface showing the presence of scrim fibers in the residual adhesive layer on one of the adherends. As the crack front advances, the fibers are pulled out of the adhesive at oblique angles, as seen from the close-up micrograph in figure 5.16. This results in the dissipation of energy and thus increases the fracture energy required for crack propagation.

5.3 CERAMIC/CMC SPECIMENS

A variety of failure modes was observed in alumina/CMC specimens described in section 4.3. A combination of crazing in both layers and interfacial fracture was observed in the specimens with the thicker CMC layer. In the other set of specimens, there was also spallation of the CMC, in

addition to the above mentioned failure modes. Figure 5.17 is a micrograph of a representative cross-section of one of the specimens, illustrating all 3 modes.

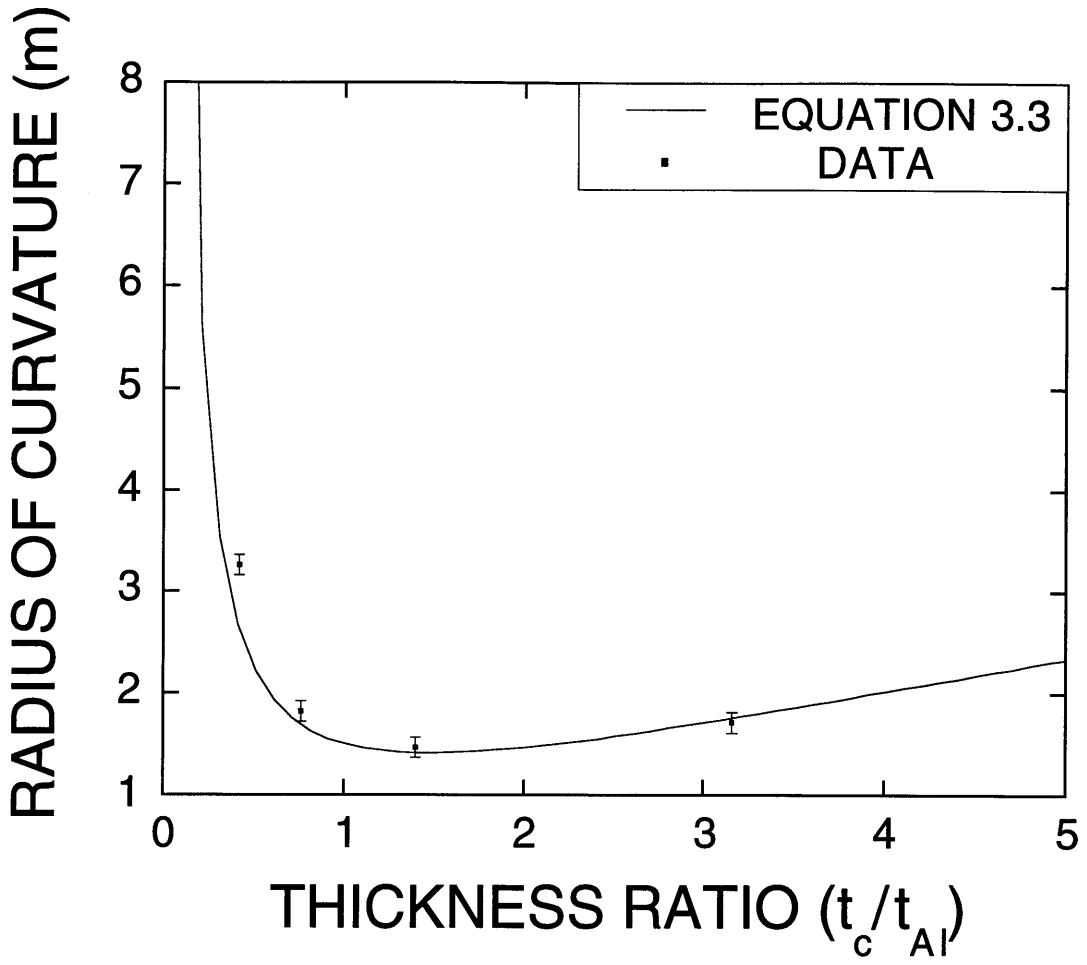

Figure 5.1 Curvature of bilayer specimens plotted against thickness ratio

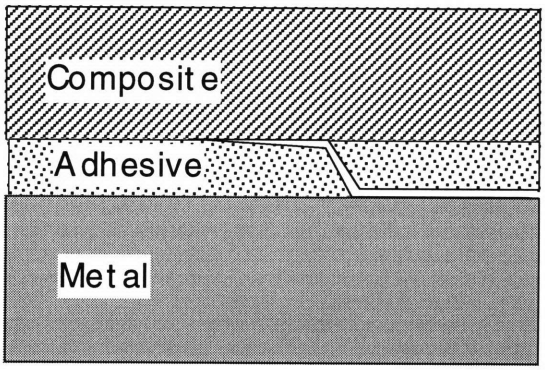

(a)

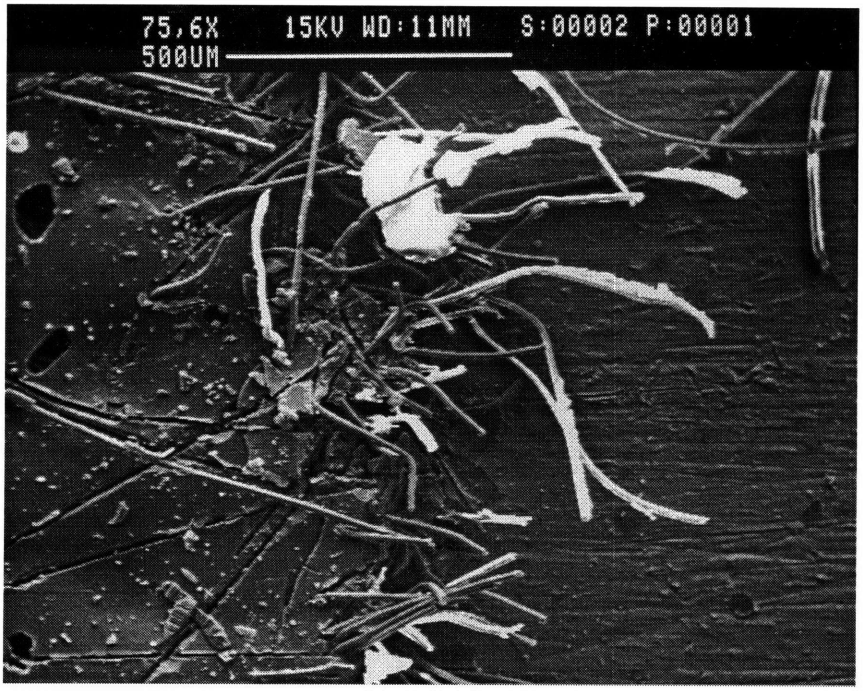

(b)

Figure 5.2 (a) Illustration of fracture path in composite-metal lap joints
(b) SEM micrograph of the transition region in the adhesive

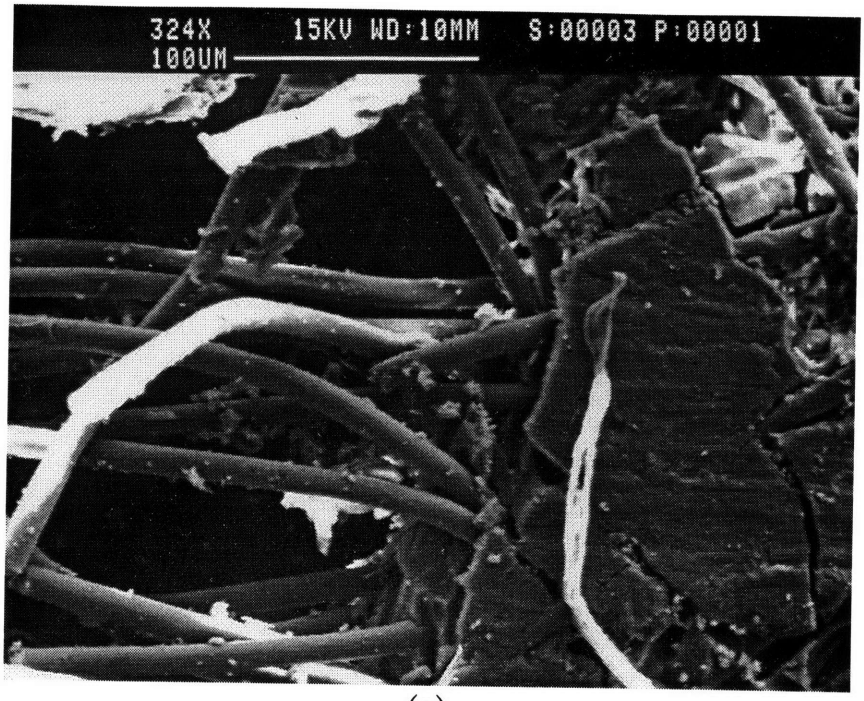

(a)

(b)

Figure 5.3 SEM micrographs of fracture surface
(a) close-up of transition region (b) adhesive surface away from transition region

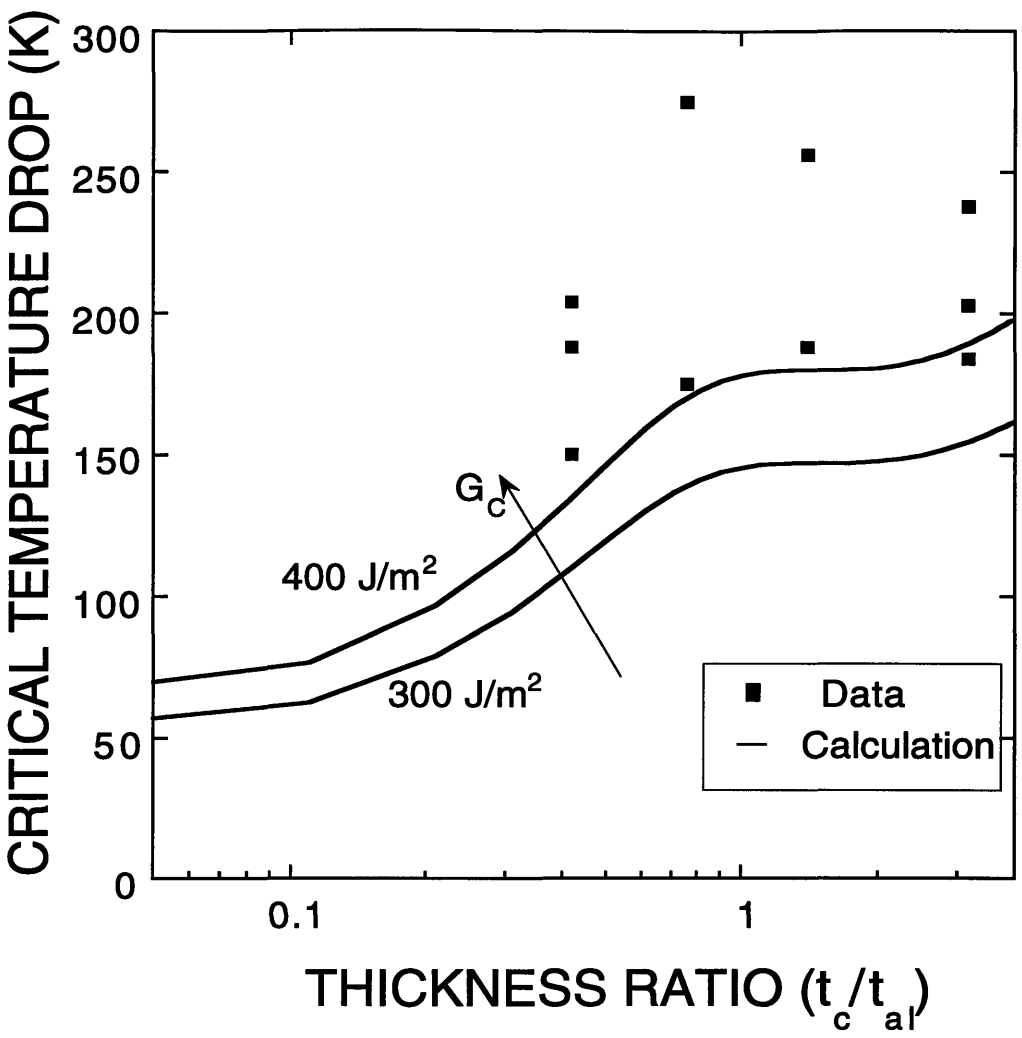

Figure 5.4 Thermal fracture data for unprecracked single lap joints between $[0]_{16}$ graphite-epoxy/ aluminum adherends

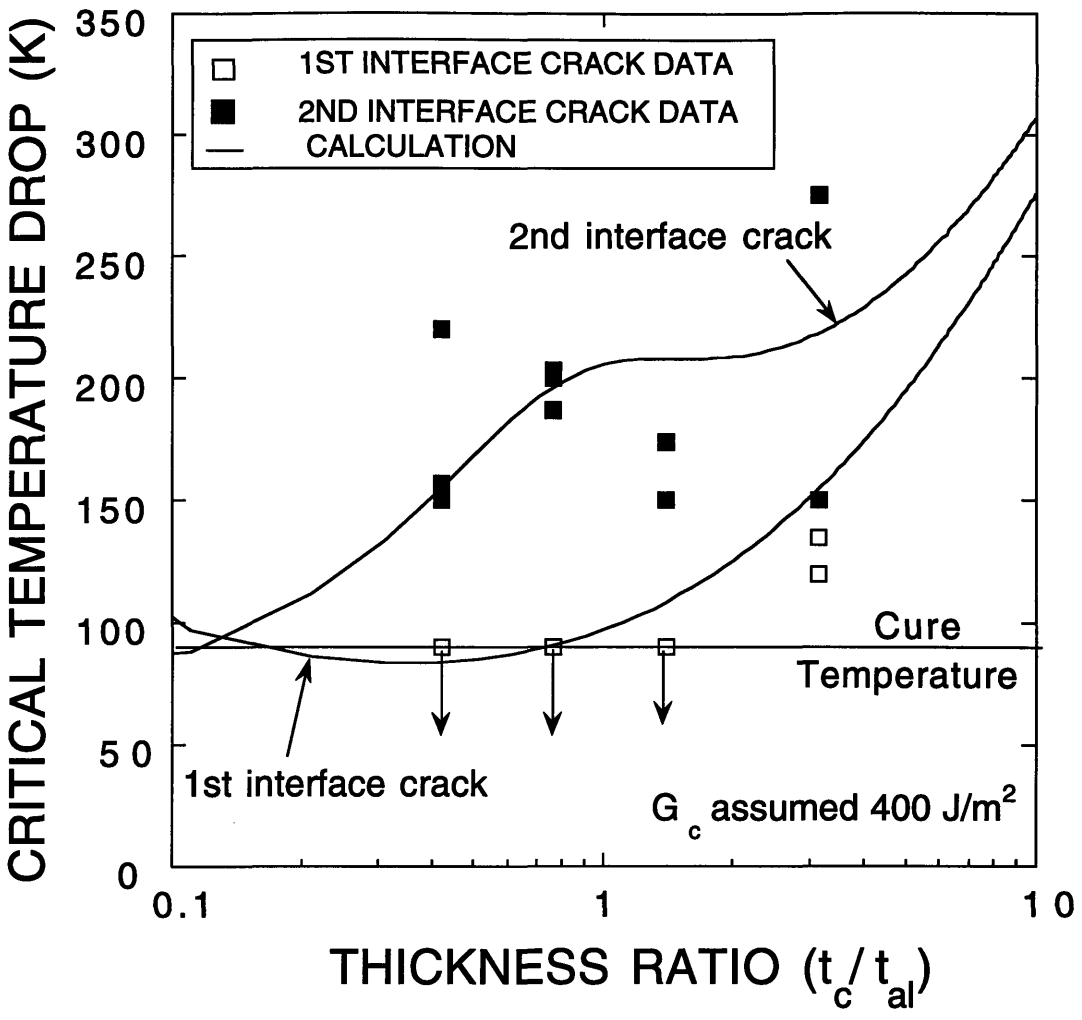

Figure 5.5 Thermal fracture data for unprecracked double lap joints between $[0]_{16}$ graphite-epoxy/ aluminum adherends

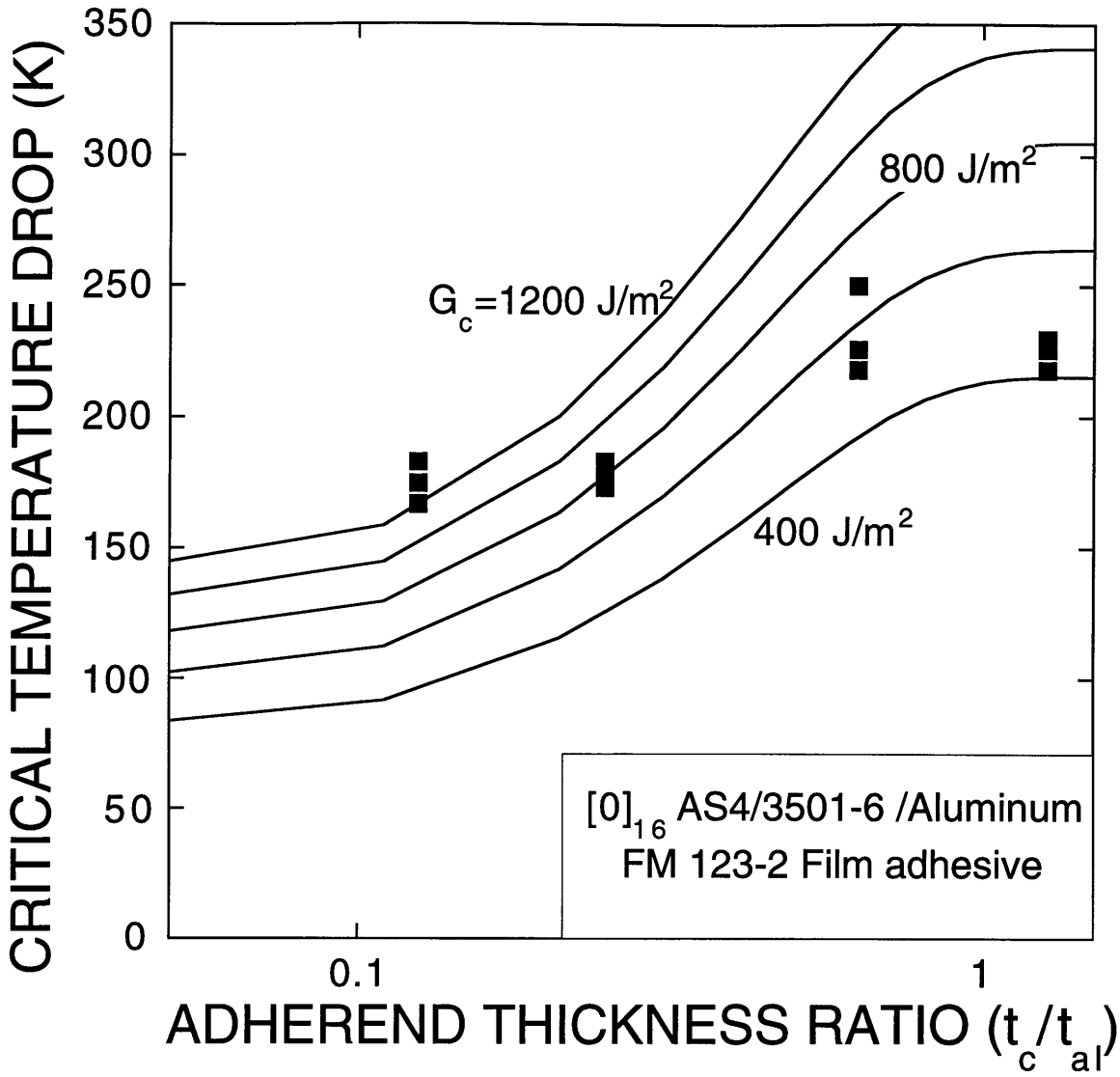

Figure 5.6 Thermal fracture data for precracked single lap joints between $[0]_{16}$ graphite-epoxy/ aluminum adherends

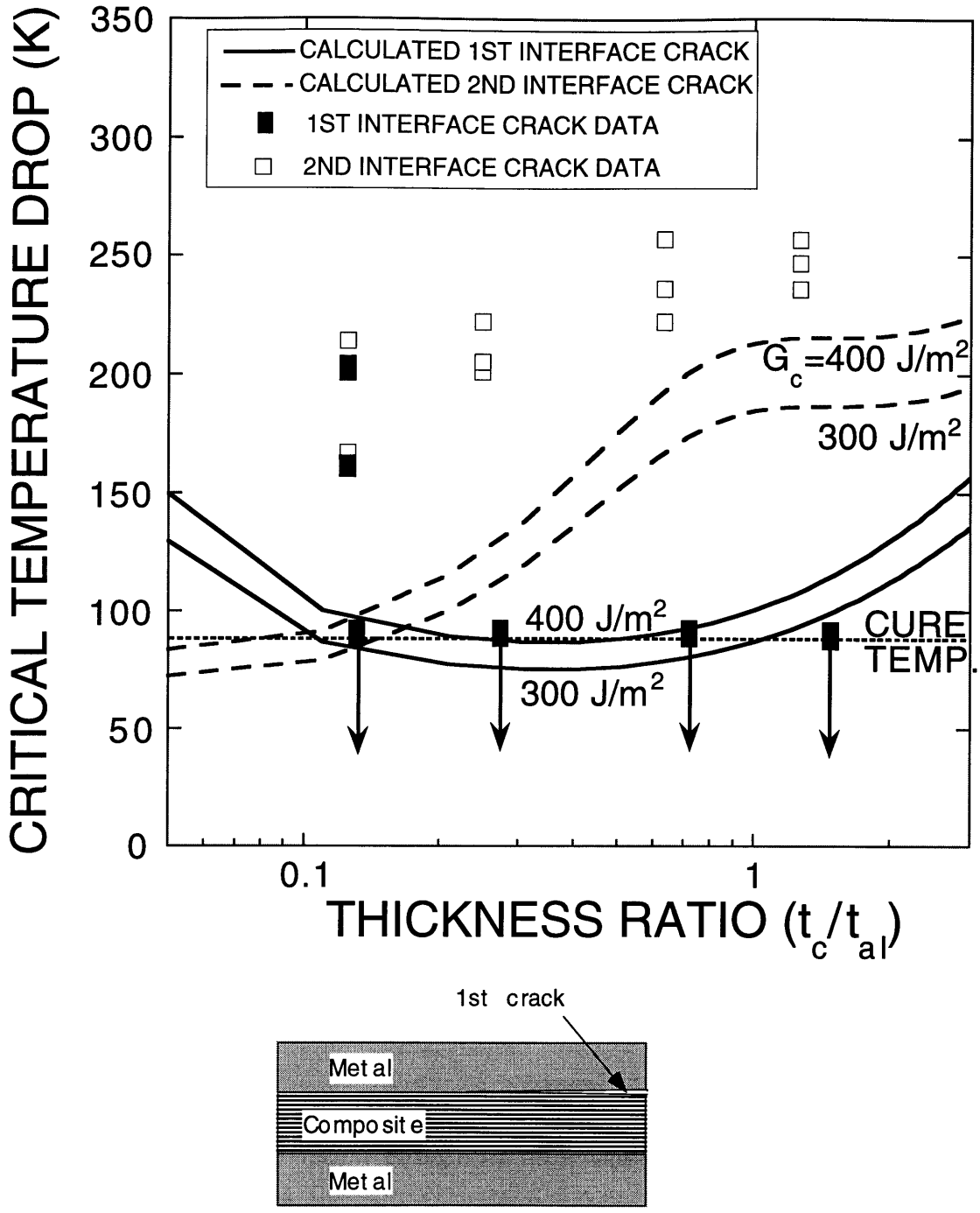

Figure 5.7 Thermal fracture data for precracked double lap joints between $[0]_{16}$ graphite-epoxy/ aluminum adherends

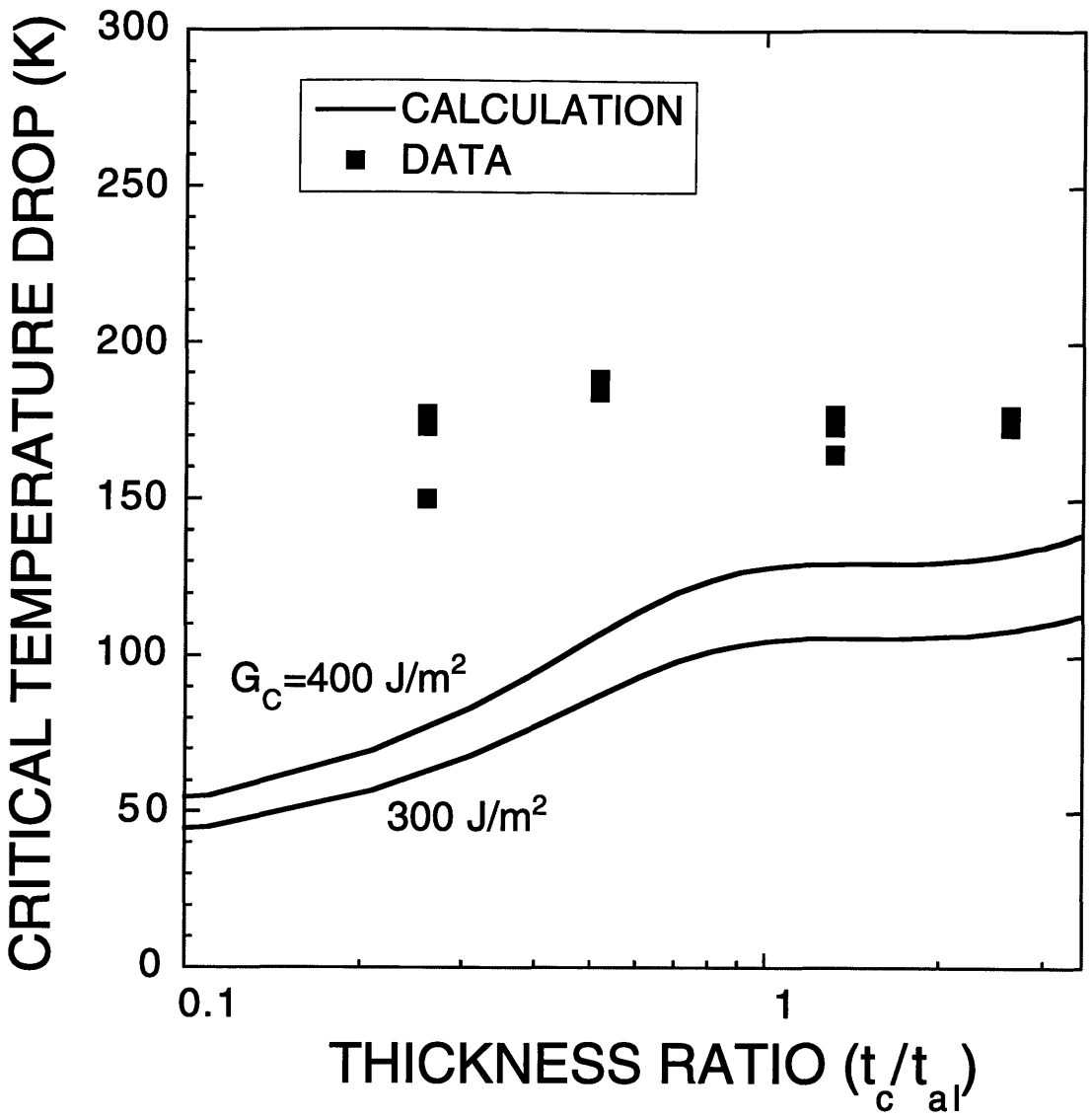

Figure 5.8 Thermal fracture data for precracked single lap joints between $[0]_{32}$ graphite-epoxy/ aluminum adherends

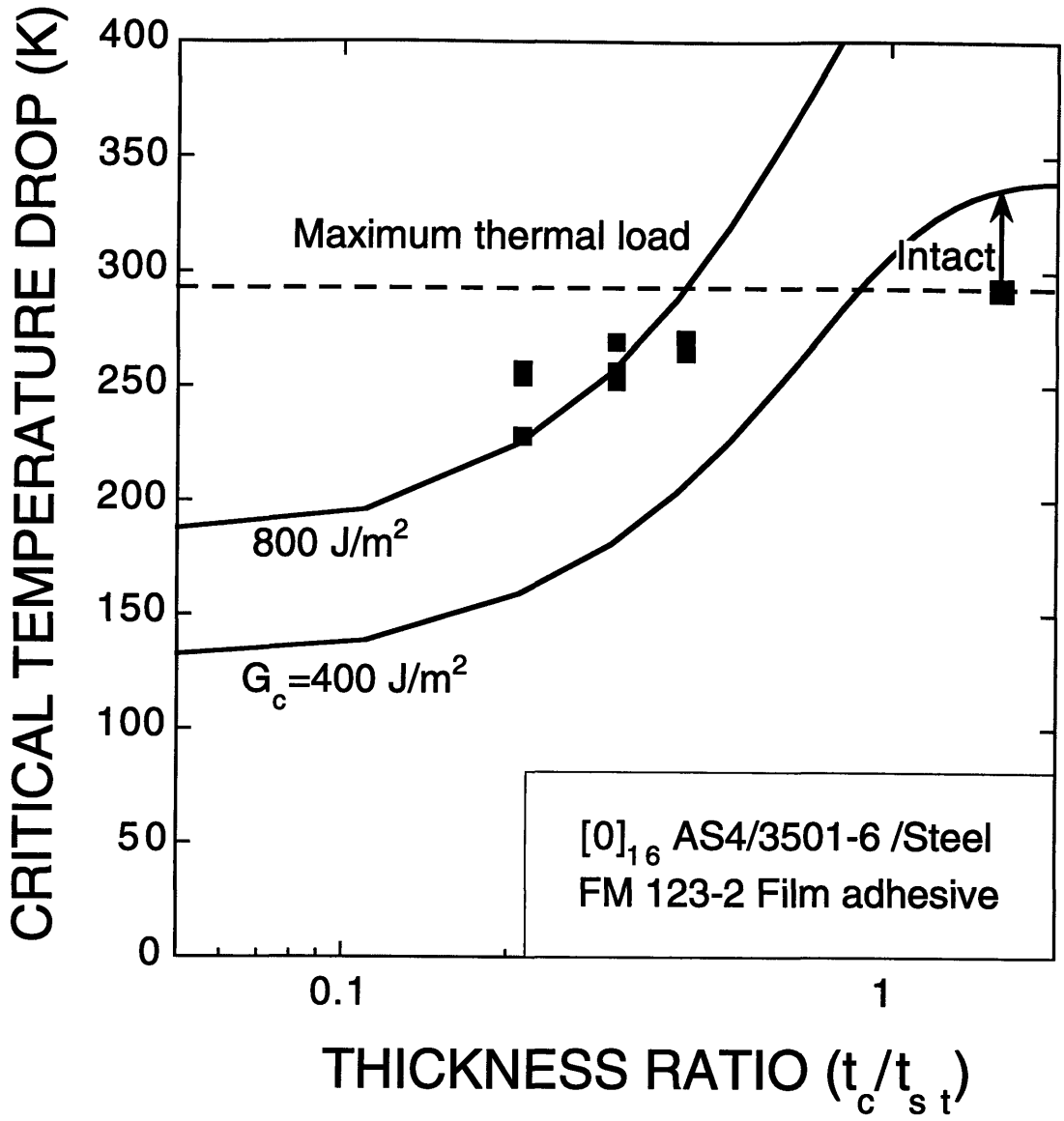

Figure 5.9 Thermal fracture data for precracked single lap joints between $[0]_{16}$ graphite-epoxy/ steel adherends

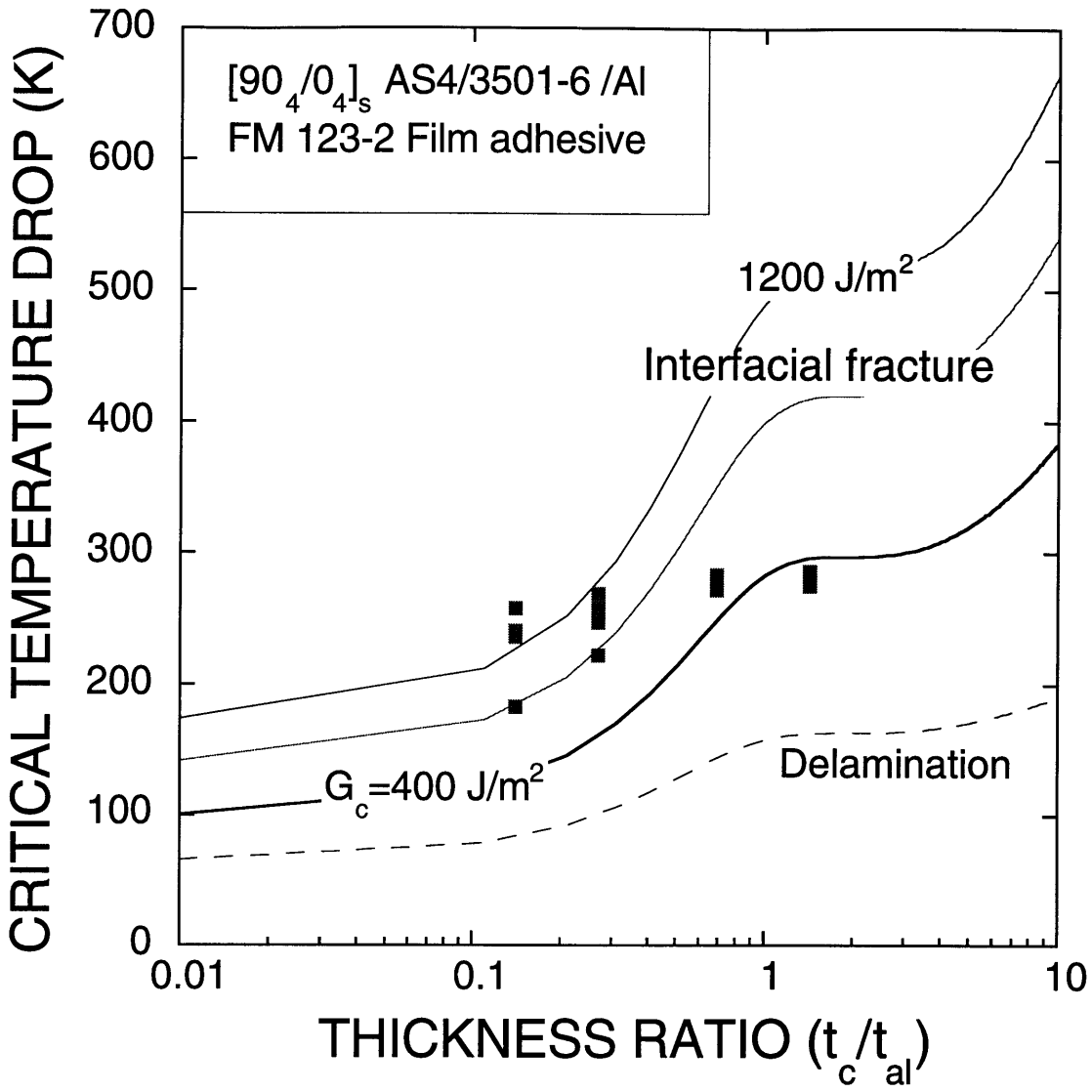

Figure 5.10 Thermal fracture data for precracked single lap joints between $[90_4/0_4]_s$ graphite-epoxy/ aluminum adherends

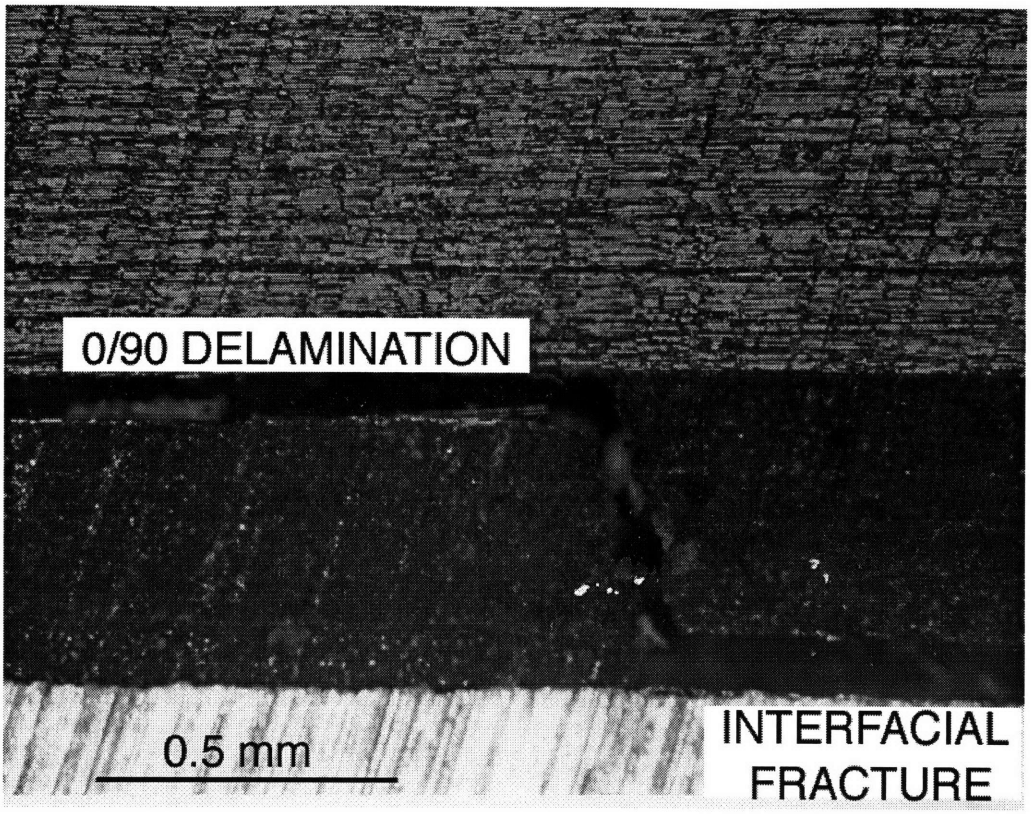

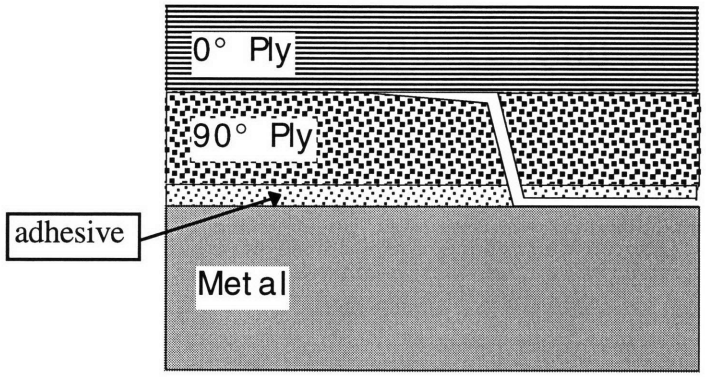

Figure 5.11 Micrograph showing delamination between 90° and 0° layers in $[90_4/0_4]_s$ graphite-epoxy/ aluminum specimens

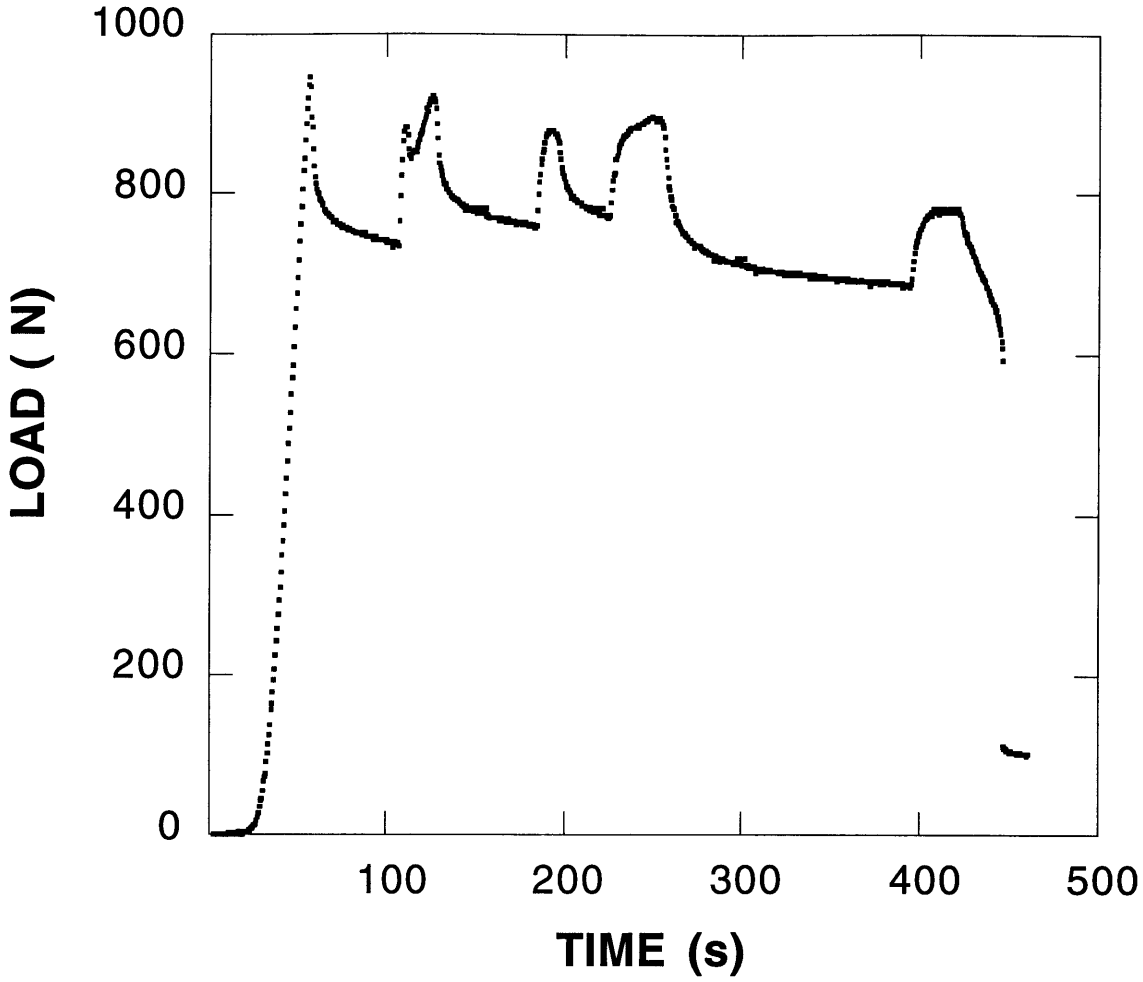

Figure 5.12 Typical load vs. time plot for a DCB specimen

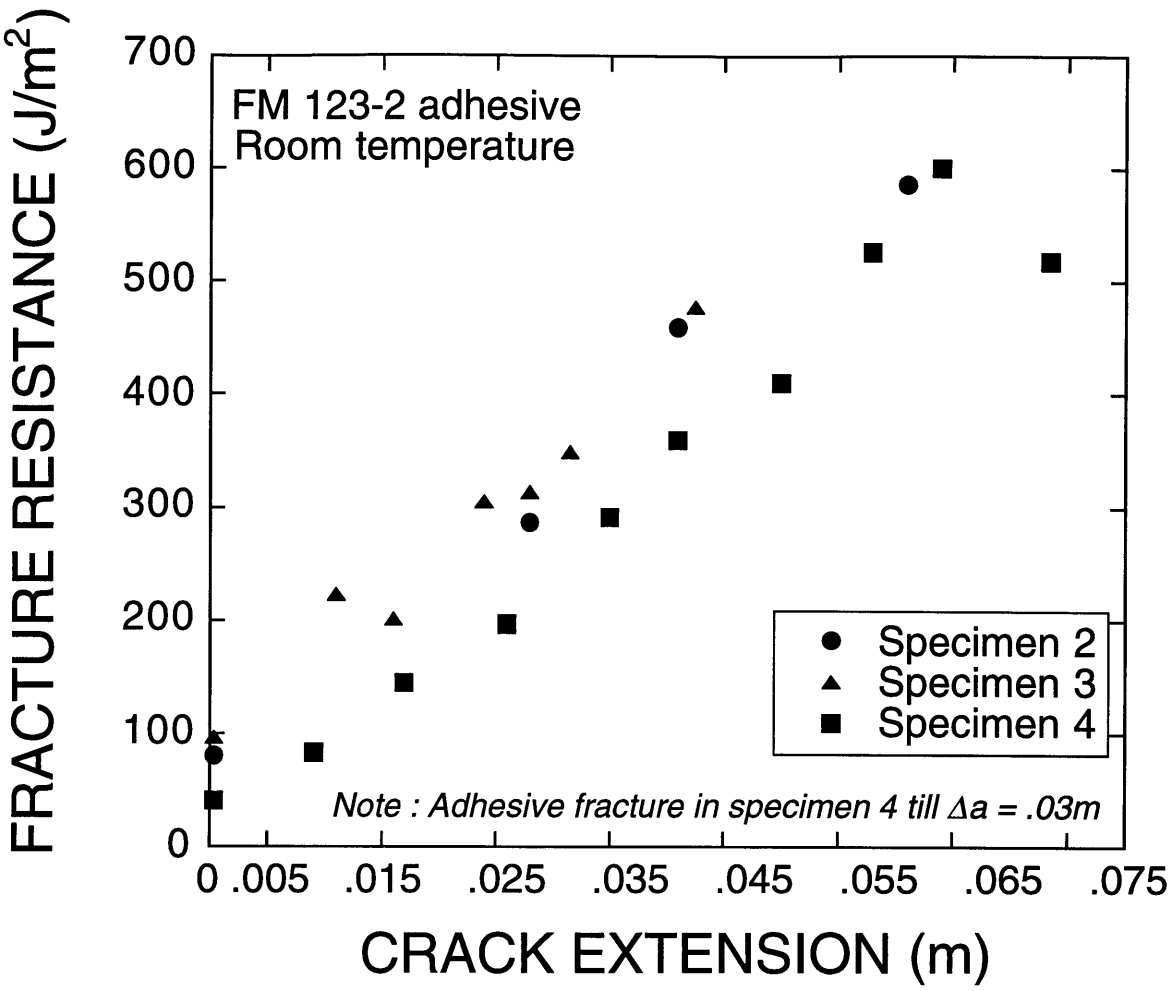

Figure 5.13 Mode I fracture resistance data for aluminum adherends (symbols correspond to 3 different specimens tested)

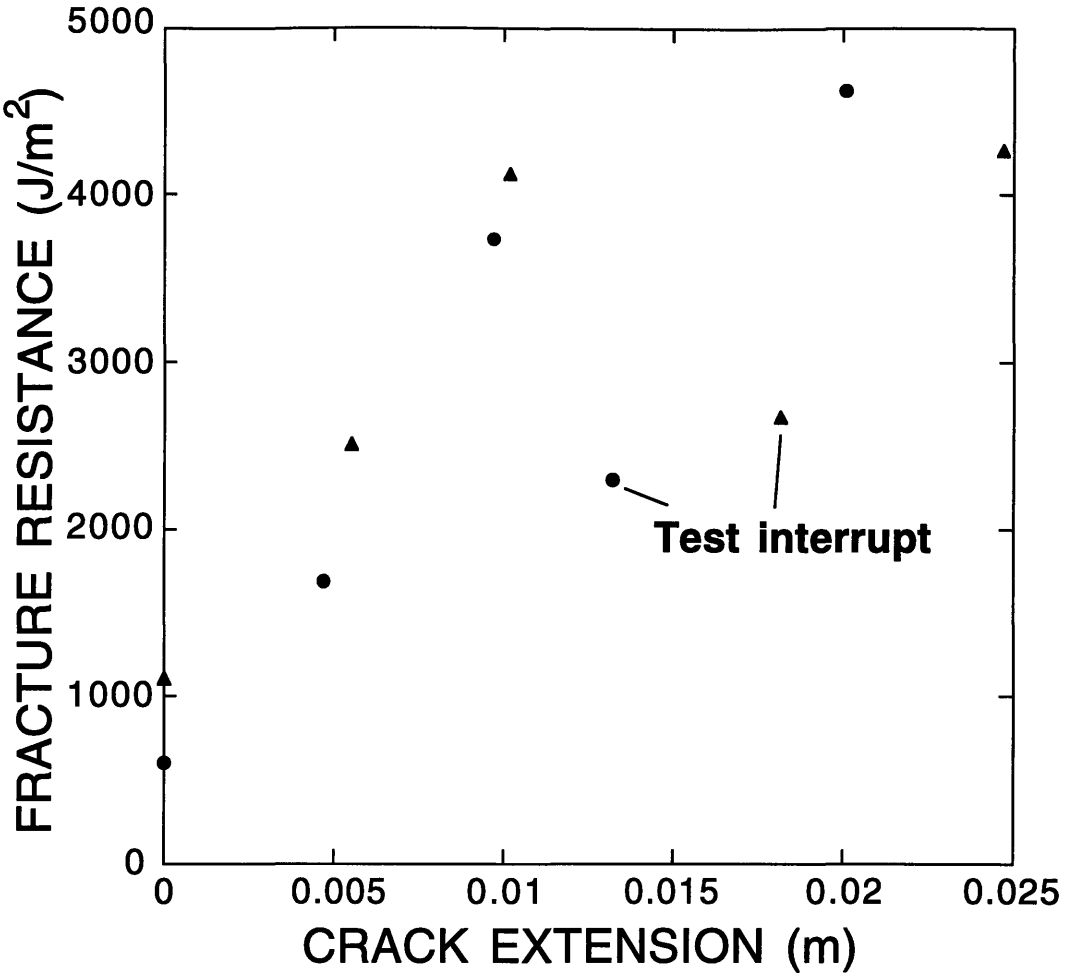

Figure 5.14 Mode II fracture resistance data at room temperature for aluminum adherends bonded with FM 123-2 adhesive

(a)

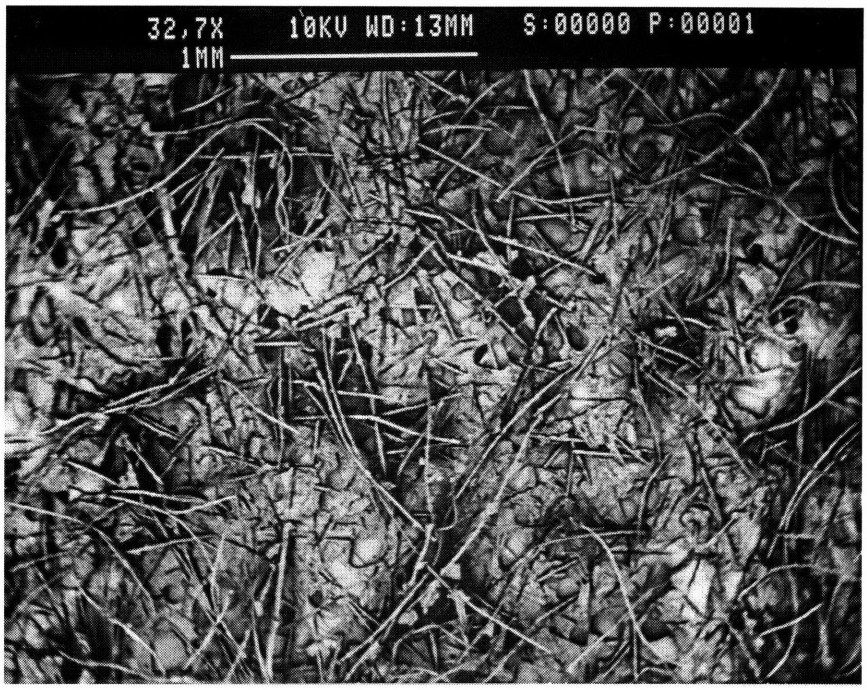

(b)

Figure 5.15 SEM micrograph of fracture surface of adhesive showing presence of bundles of scrim fibers (a) at the starter crack, and (b) away from starter crack

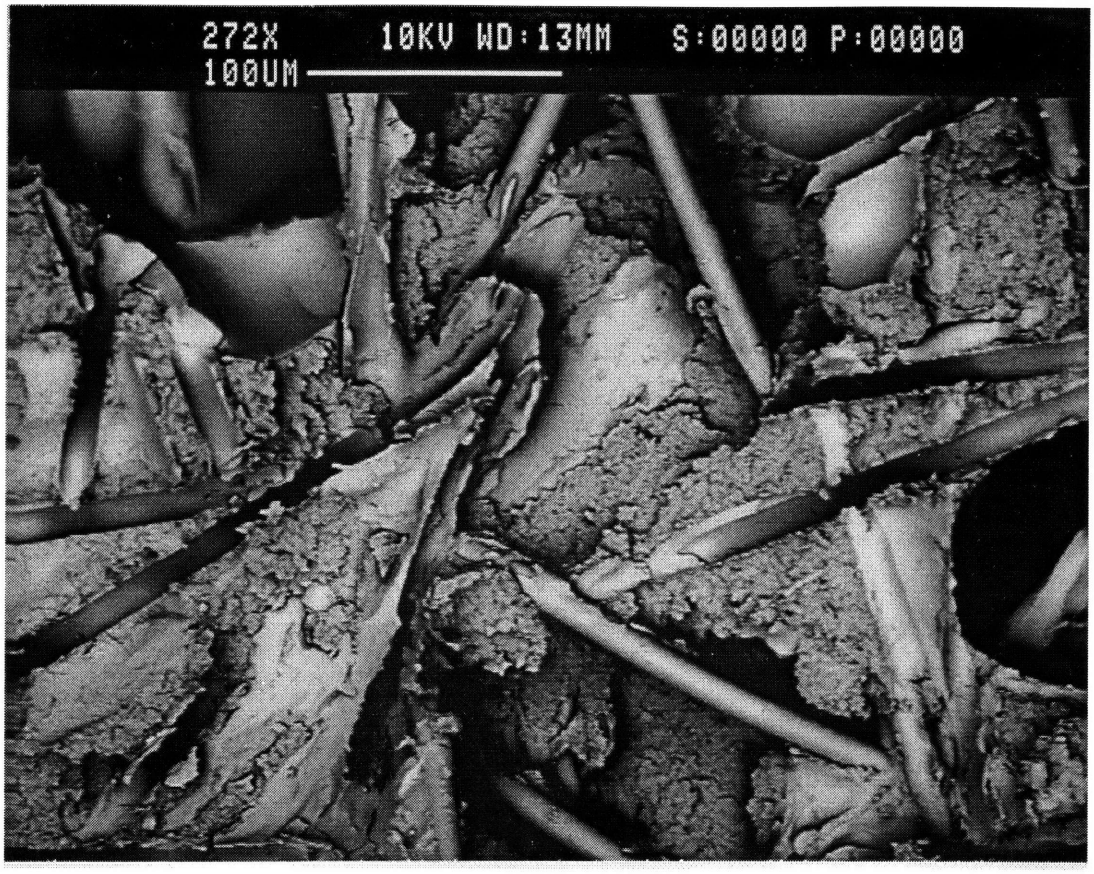

Figure 5.16 SEM close-up micrograph of adhesive fracture surface showing pull-out of scrim fibers at oblique angles

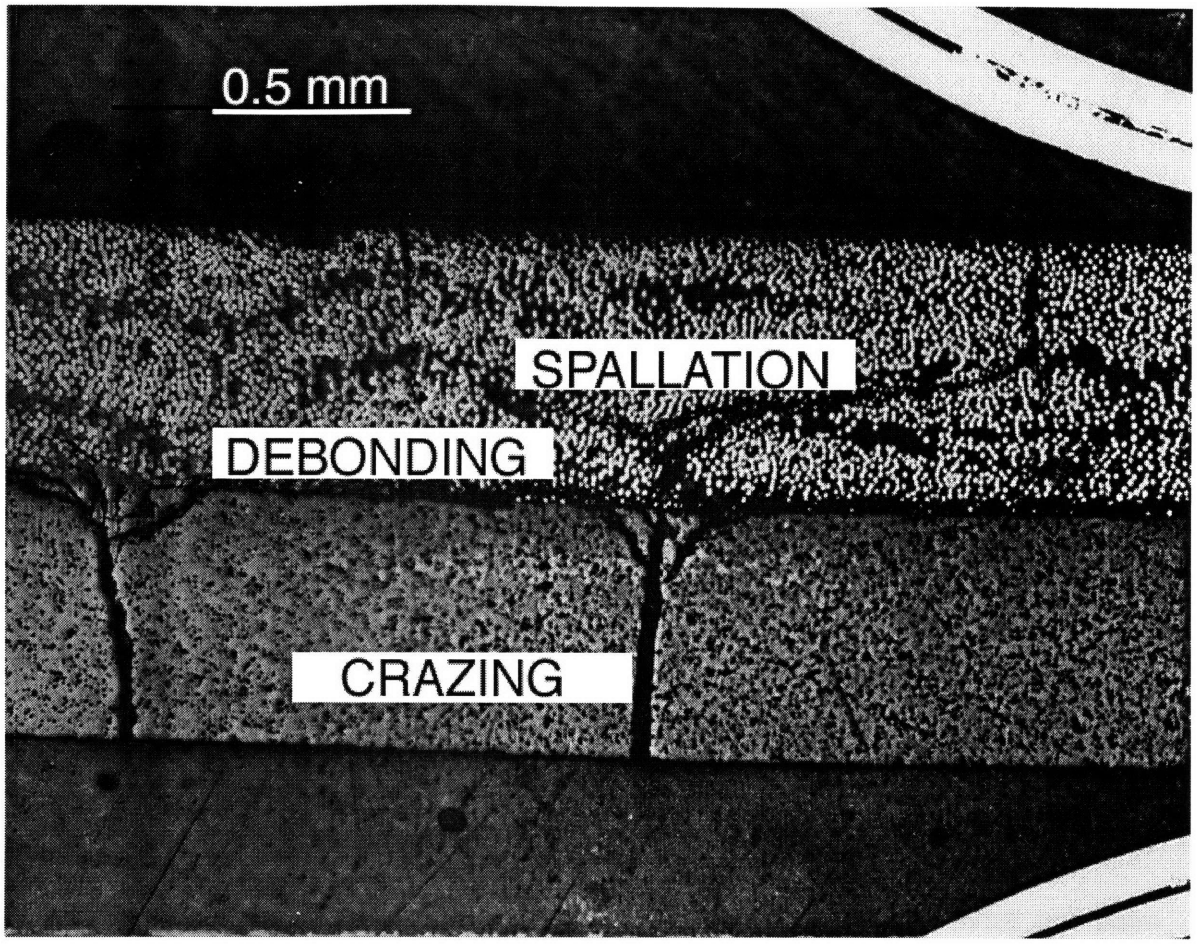

Figure 5.17 Optical micrograph of spallation, debonding, and crazing in alumina bonded with nicalon-reinforced calcium aluminosilicate.

CHAPTER 6

DISCUSSION

6.1 INFERENCES FROM EXPERIMENTAL WORK

This section presents a discussion on the validation of the fracture mechanics model formulated in chapter 3 by the experimental results described in chapter 5. The results from the thermal and mechanical tests are first correlated. The mechanics of the observed R-curve behavior are then modeled; although this is not directly connected with the thermal test results, it nevertheless provides some useful insights into the efficient design of adhesive joints. Finally, the concept of failure design maps is introduced with some illustrative examples.

6.1.1 Results from thermal testing and correlation with mechanical testing

As seen from the results in chapter 5, the steady-state fracture mechanics analysis correctly predicts trends in the critical temperature drop to cause failure as a function of adherend stacking sequence, adherend thicknesses, and joint configuration. Furthermore, the analysis correctly

predicts the change in crack trajectory between the unidirectional and cross-ply specimens.

The mechanical tests provided a measure of the mixed-mode fracture energy of the adhesive interface between the composite and the metal. As seen in chapter 5, the initiation values for the mode I and mode II toughness are approximately 100 J/m^2 and 900 J/m^2 respectively. The mixed-mode fracture resistance is expected to lie between these two values [17], and this correlates well with the toughness values that can be inferred from the thermal test data. However, it is seen that in all cases, constant values of adhesive and delamination toughness fitted at one thickness ratio provide overly conservative predictions at lower values of the composite-to-metal thickness ratio. It is clear that a unique value of adhesive toughness is not sufficient to characterize the data. There are several possible reasons for this phenomenon, including: the mode-mixity of fracture, the effect of short (non-steady-state cracks), the temperature dependence of adhesive properties and stress state, and the effect of large scale nonlinearity of the adhesive and adherend materials. Some of these factors were examined in detail, and results from this work are described in the following subsections.

6.1.2 Mode-mixity

Adhesive toughness is, in general, a function of the mode-mixity [14, 16]. Other factors being the same, the mode-mixity of an interface crack would

depend on the ratio of thicknesses between the two materials. Hutchinson and Suo [14] have provided solutions for the complex stress intensity factor for an interface crack in an elastic bilayer. Based on their solutions, it was seen that the variation in mode-mixity between the range of thickness ratios used for the single lap joints was less than 10°. This might be expected to cause a variation on the order of 100 J/m^2, based on the mode I and II values of G_c. This is substantially less than is required to fit the experimental data. Although an exact analysis was not performed for the double lap joints, the variation in mode-mixity between them was estimated to be of a similar magnitude as that for the single lap joints. From these estimates, it was concluded that variation in mode-mixity was not responsible for the observed fracture behavior.

6.1.3 Short Crack Effects

The second factor investigated was the possibility that the precrack length was insufficient to ensure that the thicker specimens underwent steady-state fracture. This would violate the steady-state assumption used to calculate the strain energy release rate and would lead to higher apparent fracture energies for those thickness ratios. An analysis of the influence of crack length was performed using results from Akisanya and Fleck [64] as described in section 3.3. It was seen, that in all cases, steady-state was achieved within a precrack length of 4-5 times the composite layer thickness.

The precrack length used in the experiments was in all cases more than 12 times the composite thickness. Hence, it is unlikely that any of the specimens fall into the "short crack" regime. It should be noted that Akisanya and Fleck have assumed a symmetry boundary condition on the outer face of the substrate (i.e. forces and moments on the film do not cause substrate deformation). This condition does not hold true for the specimens used in the present work, hence their analysis is not strictly applicable. Nevertheless, the order of magnitude of the results is not expected to change with changing boundary conditions. Short cracks, therefore, are not a likely explanation for the discrepancy.

6.1.4 Temperature Dependence of Adhesive Properties

The temperature dependence of adhesive properties is a third potential source of the discrepancy between modeling and experiment. The apparent adhesive fracture energy in the single lap joints decreased with increasing temperature drop from the cure temperature. This is consistent with polymer behavior [44]; decreasing temperatures would be expected to cause the adhesive to behave in an increasingly brittle manner. This could have the consequence of decreasing toughness from a value of approximately 1200 J/m^2 at room temperature to 400 J/m^2 at the minimum temperature. However, this observation is not supported by the data from tests on double lap joints (see figure 5.9). It is seen that most data points correspond to fracture

energies of 400 J/m^2 or less, even though temperatures are above room temperature. Hence, it was concluded that the adhesive fracture energy was not temperature-dependent for the range of test temperatures used. It is also likely that the presence of the glass fiber scrim in the adhesive layer would reduce the temperature sensitivity of the adhesive.

6.1.5 Edge-Stress Analysis

The possibility of the three-dimensional stress state prevalent at the free edges of the specimens contributing to failure was also examined. Kassapoglou and Lagace [70] formulated the problem of interlaminar stresses in a symmetric laminate and provided an efficient method to determine it, based on assumed stress shapes and minimization of complementary energy. Their method was applied to the present case of double lap joints to solve for the edge stresses. It was seen that the three dimensional edge stresses σ_{33} and σ_{23} were both of the order of 1 MPa, or less, close to the edges. Since this is at least an order of magnitude smaller than typical values of adhesive strength [44], it was concluded that interlaminar stresses did not contribute significantly to the fracture of these joints.

6.1.5 Material Non-linearity

Another potential factor responsible for the observed discrepancy is nonlinear constitutive behavior of the adhesive. It should be noted that a

small change in the adhesive constitutive behavior could result in a large change in its toughness. Large scale adhesive plasticity could result in a blunt crack tip, contrary to linear elastic fracture mechanics assumptions. A detailed investigation into this problem can only be possible numerically, and has not been attempted as part of this thesis.

From the above analyses, it is seen that the observed lower sensitivity of the critical temperature drop to the adherend thickness ratio was not conclusively explained. However, some issues, such as the role of the adhesive layer, were not examined in detail. These could form the basis for future work on this topic. Numerical analyses, using finite elements, could be useful in the analysis at the lengthscale of the adhesive thickness. It should also be noted that the factors examined in sections 6.2.1-6.2.4, though not significant for the test geometries used in this study, could assume significance for other geometries used, and therefore, need to be considered for efficient joint design.

6.2 R-CURVE MODELING

A methodology for modeling R-curve behavior due to bridging has been developed for composite materials [71-73]. Since R-curves depend on specimen geometry, the characterization of materials using bridging laws is favored. Suo et al [72] have presented a comprehensive methodology for the prediction of R-curves from a general traction law. The damage response is simulated by

means of an array of continuously distributed, non-linear springs. The fracture resistance is then a function of the initiation toughness, the stiffness ratio of the springs to the specimens, the bridging traction, and the ratio of the bridged length to the beam thickness. The inverse analysis can also be performed, i.e. the bridging parameters can be estimated if the R-curve is experimentally measured, as in this case. A softening linear bridging law was assumed, following previous work on modeling systems in which fibers break away from a crack plane and subsequently pull out [72]. This is depicted in figure 1. The modeling procedure followed the approach described in appendix A1 of reference [71].

Values of the bridging law parameters of p_o=0.9 MPa and u_o=1.1 mm were back-calculated using G_{ss}=600 J/m^2, G_o=100 J/m^2 and L_{ss}=75 mm, where the subscript 'ss' denotes steady-state. The R-curve calculated using these values is shown in figure 2. The calculated bridging parameters are typical of those observed for frictionally sliding fibers in other material systems [71]. Modeling was not attempted for the mode II R-curve due to the uncertain effect of friction.

The mechanical test results and associated modeling show that relatively weak bridging tractions can result in significant increases in toughness over the inherent initiation toughness of the adhesive. A low volume fraction of scrim fibers, although principally oriented in the plane of the bond line can, nevertheless, result in an order of magnitude increase in

toughness. It was concluded that if a fracture mechanics approach is to be applied to designing adhesive joints or predicting their damage tolerance, this bridging behavior should be accounted for. The designer should also be aware that the resulting R-curve is likely to be strongly dependent on the geometry of the joint. Firstly, there is a strong influence of the mode of loading; and secondly, the stiffness of the adherend relative to the bridging tractions causes the R-curve to develop more slowly for thicker adherends. This is illustrated in figure 6.3, which shows a prediction of an order of magnitude increase in the crack extension to achieve steady-state as the adherend thickness increases from 1mm to 50 mm.

6.3 FAILURE MECHANISM MAPS

The competition between the various failure modes encountered so far can be assessed using the concept of failure mechanism diagrams [3]. The objective is to be able to characterize failure solely in terms of material and interfacial properties, layer thicknesses, and applied temperature change. Given the above information, preliminary design may be possible for any combination of materials from this single diagram. The effect of changing material properties, toughnesses, and/or geometry are readily visualized from the diagram. For a given pair of materials, it is possible to allow any two relevant parameters to vary while holding the others constant.

Such diagrams can be constructed in several formats. One possible format is displayed in figures 6.4-6.7. Figure 6.4 is the failure mode diagram for an aluminum/unidirectional graphite-epoxy bilayer. Here the composite thickness is fixed at 2 mm, the interfacial fracture energy is taken to be 400 J/m^2 and the mode I toughness of the composite is taken as 180 J/m^2 [74]. Using this information, the temperature change and thickness of metal to cause fracture can be determined. Each shaded region corresponds to a particular failure mode. Changing either the interfacial or delamination fracture energy or the matrix cracking strength has the effect of shifting the corresponding curve up or down on the temperature axis. From the diagram, it is seen that interfacial fracture and delamination are the dominant fracture modes for this configuration, while matrix cracking is not a concern. A similar diagram is constructed in figure 6.5 for an aluminum/cross-ply graphite-epoxy bilayer. The delamination toughness of the 0/90 interface is also taken as 180 J/m^2. In reality, this may be higher because the delamination is mixed-mode. However, using the lower value allows a conservative estimate for the temperature drop to cause delamination to be obtained. For this configuration, any of the three failure modes are possible depending on the relative thickness ratio.

Figure 6.6 is a failure design map for a double lap joint consisting of 2 mm thick graphite/epoxy sandwiched between 2 aluminum adherends. The material properties and toughnesses are taken to be the same as before.

Steady-state delamination and alligatoring cracks are assumed to exist before loading, thus making the predictions of both delamination and alligatoring very conservative. In practice, these assumptions are not satisfied, which presumably causes interfacial fracture to take place first. It is apparent that matrix cracking is not a concern for physically realizable temperature drops in this configuration.

Figure 6.7 shows a failure design diagram for the other combination of materials examined, i.e. bilayers of alumina bonded to Nicalon-reinforced calcium aluminosilicate. The stress-free temperature was assumed to be 1000°C. It is seen that crazing of either layer, spallation of the CMC, and interfacial debonding are all possible for thickness ratios of 1 and 0.5, as was observed.

A second format for design diagrams is illustrated in figures 6.8 and 6.9. This plots the adherend coefficient of thermal expansion (α) versus modulus of elasticity (E) for single lap joints (figure 6.8) and double lap joints (figure 6.9). For each of the diagrams, one of the materials is taken to be AS4/3501-6 with a thickness of 2 mm. The temperature load is fixed at ΔT=200 K. The contours on the graphs represent limiting values of E and α to just cause fracture for the other adherend (material 2). These calculations assume that a single value of G_c = 400 J/m^2 is the critical strain energy release rate for fracture. If the thickness of layer 2 is prescribed, then from the diagram, one can obtain a range of values of E and α for material 2. The

safe design region is the region under the curve corresponding to the given thickness. Also plotted are approximate contours for the locations of commonly used engineering materials. The range of values of α is bounded below zero by mirror images of the curves shown. This is because α_1 was taken to be zero. In general, the curves would be symmetric about $\alpha=\alpha_1$. Note that the dependence on α is very strong compared to E. The allowable design region for double lap joints is smaller than that for single lap joints, as expected due to the higher strain energies (see figure 3.4). Following a similar methodology, allowable thicknesses for a known range of E and α values can be determined.

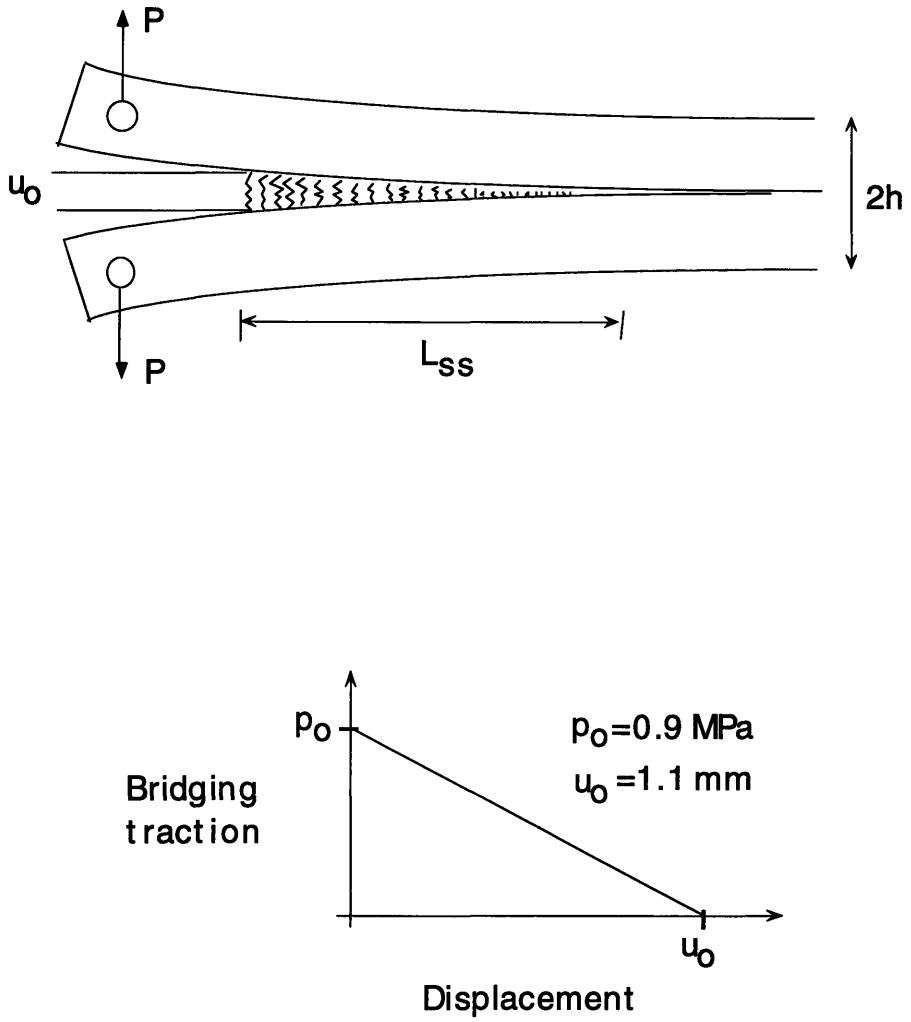

Figure 6.1 R-curve modeling and bridging law

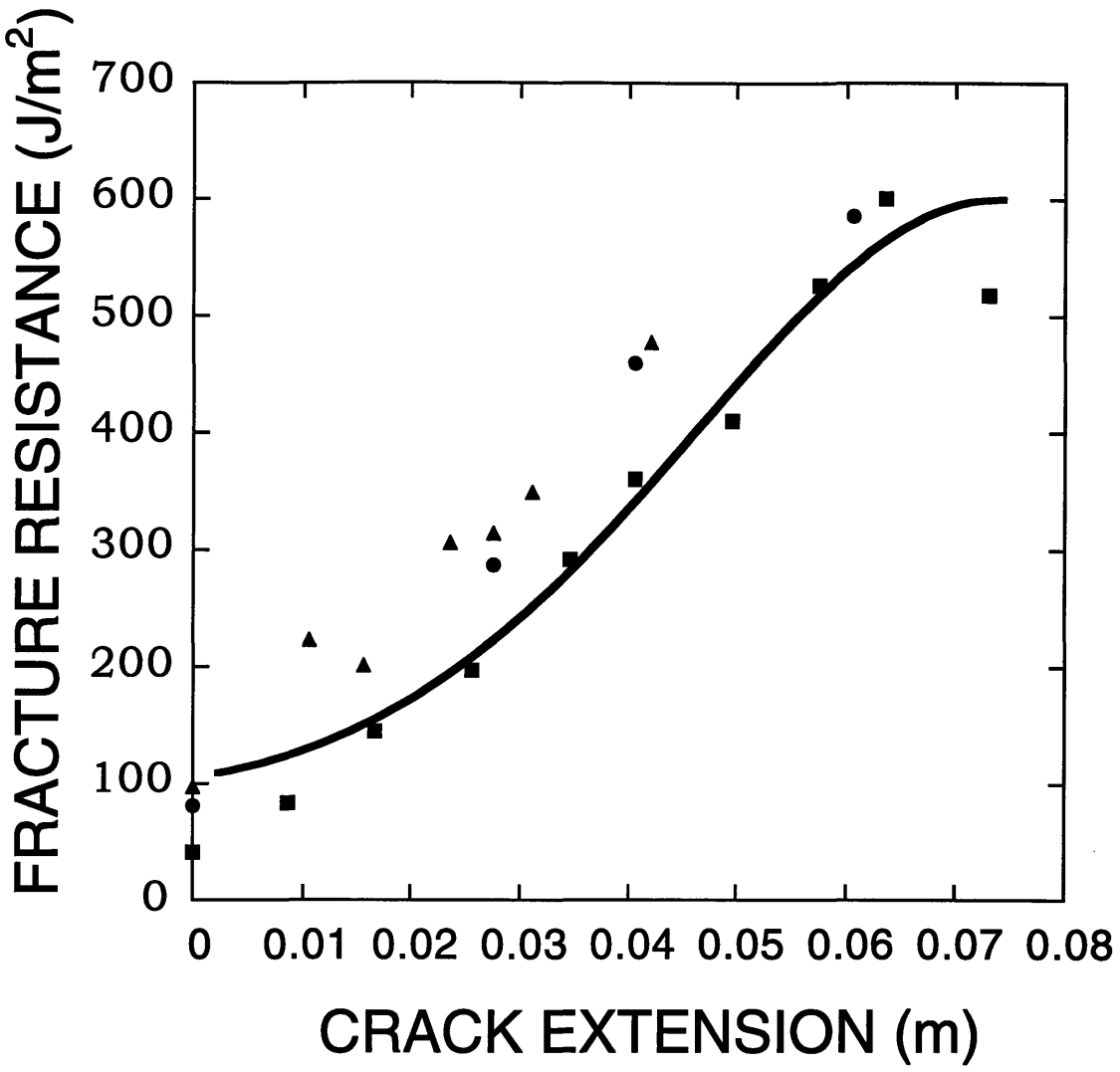

Figure 6.2 R-curve calculated assuming softening bridging tractions, superimposed on fracture resistance calculated from measured data

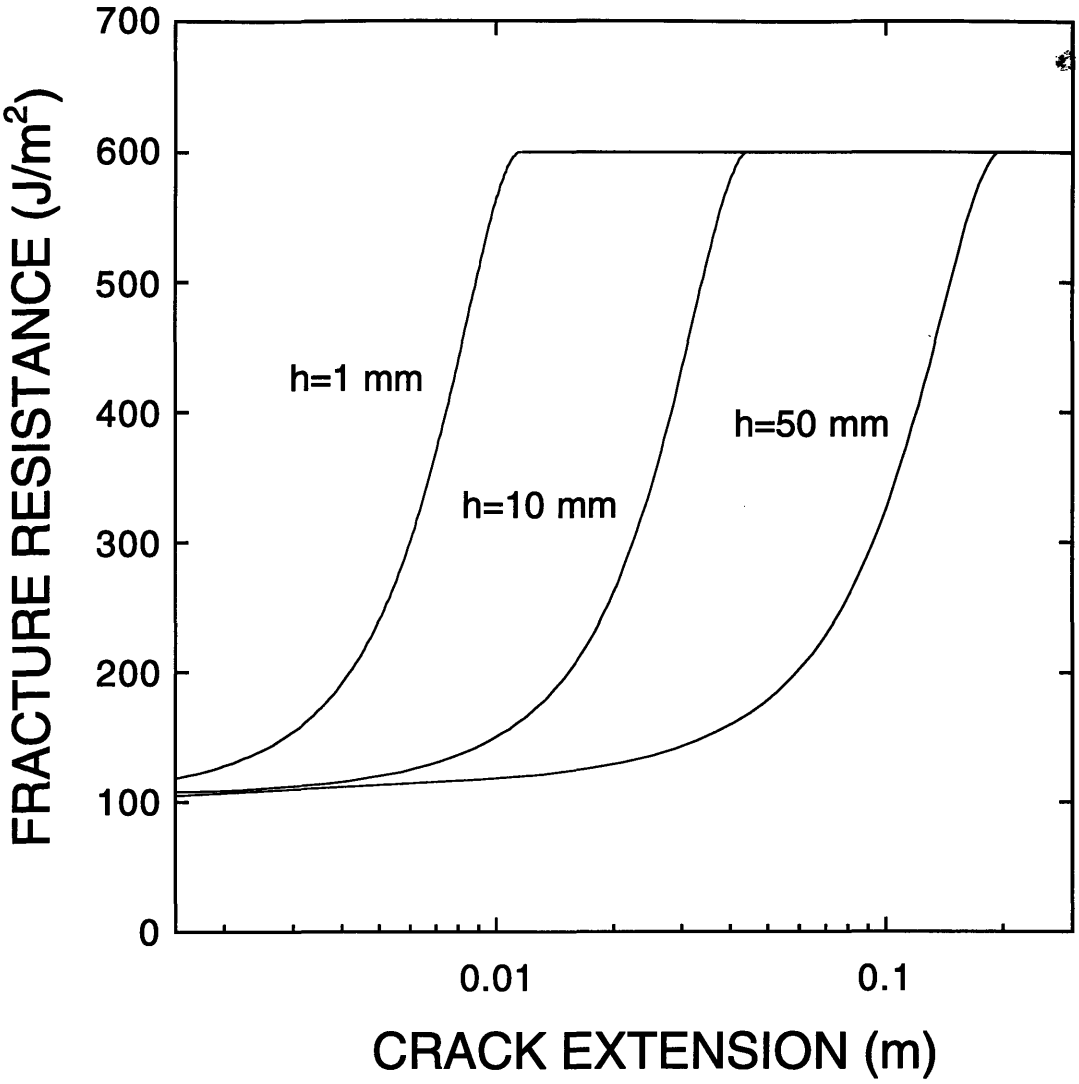

Figure 6.3 Predicted R-curves for DCB specimens of three different thicknesses assuming the bridging behavior shown in figure 6.1

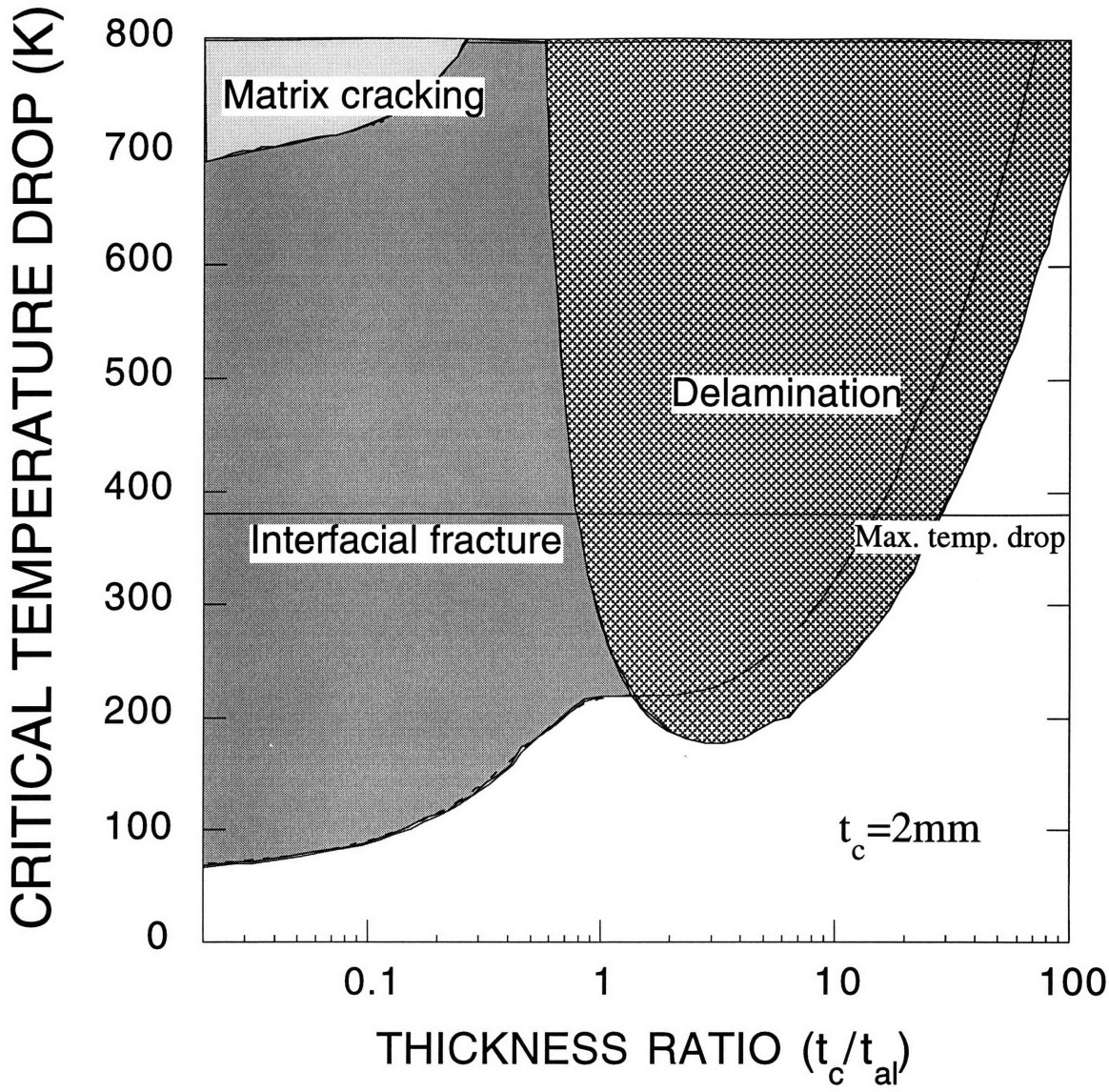

Figure 6.4 Failure mechanism diagram for $[0]_{16}$ AS4/3501-6 graphite/epoxy-aluminum single lap joint. Composite thickness is taken to be 2 mm.

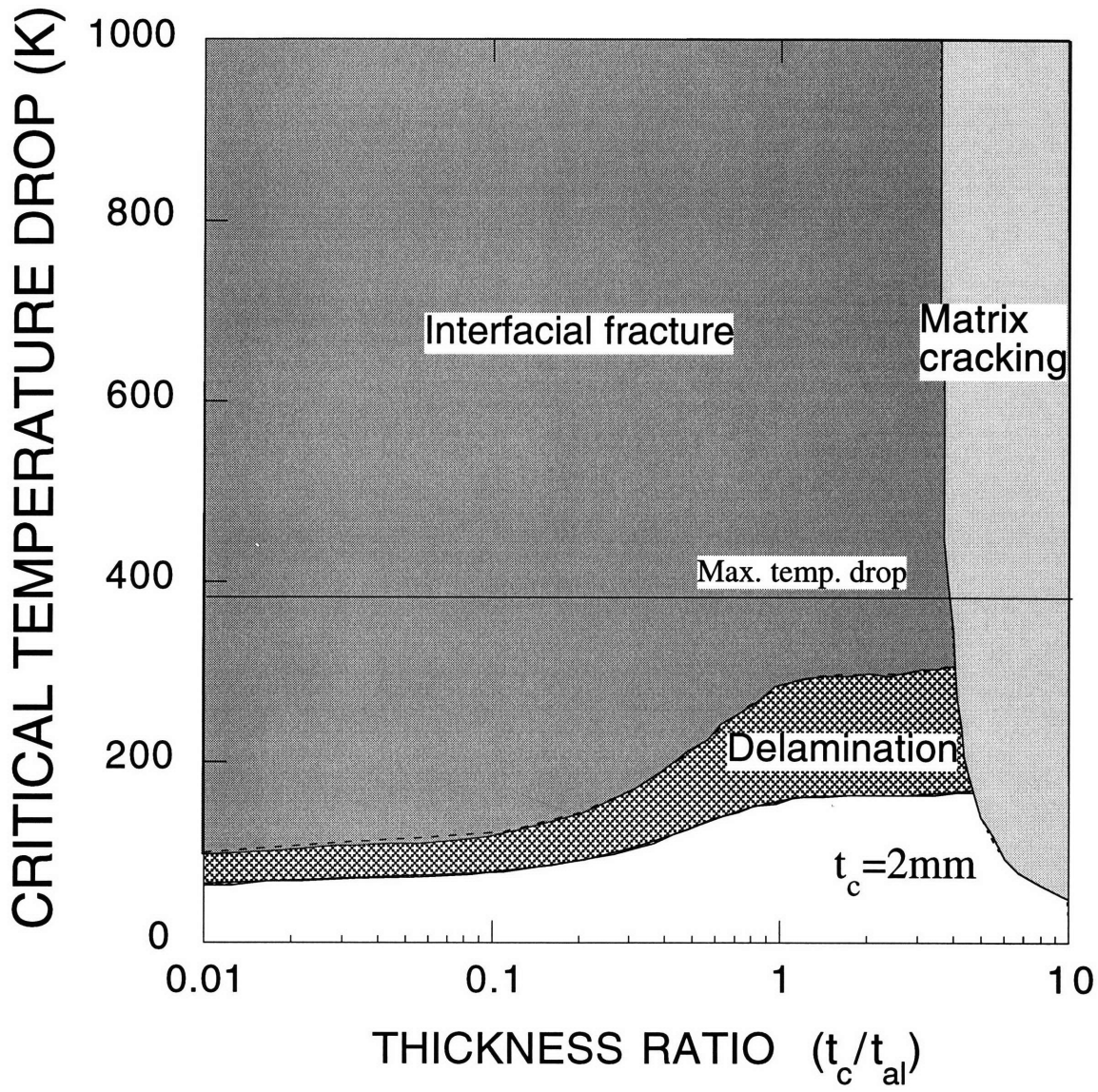

Figure 6.5 Failure mechanism diagram for $[0_4/90_4]_s$ AS4/3501-6 graphite/epoxy-aluminum single lap joint. Composite thickness is taken to be 2 mm.

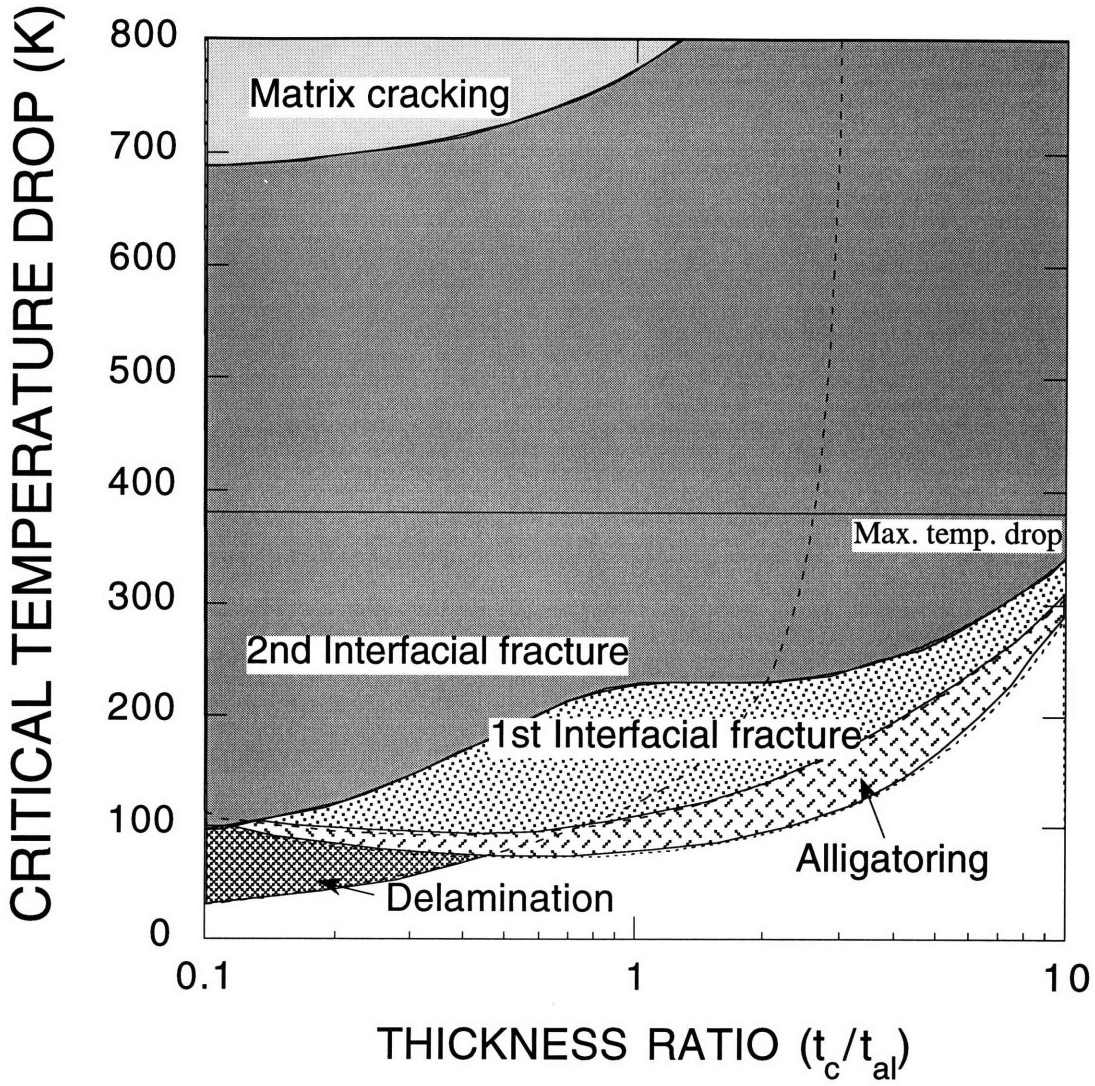

Figure 6.6 Failure mechanism diagram for $[0]_{16}$ AS4/3501-6 graphite/epoxy-aluminum double lap joint. Composite thickness is taken to be 2 mm.

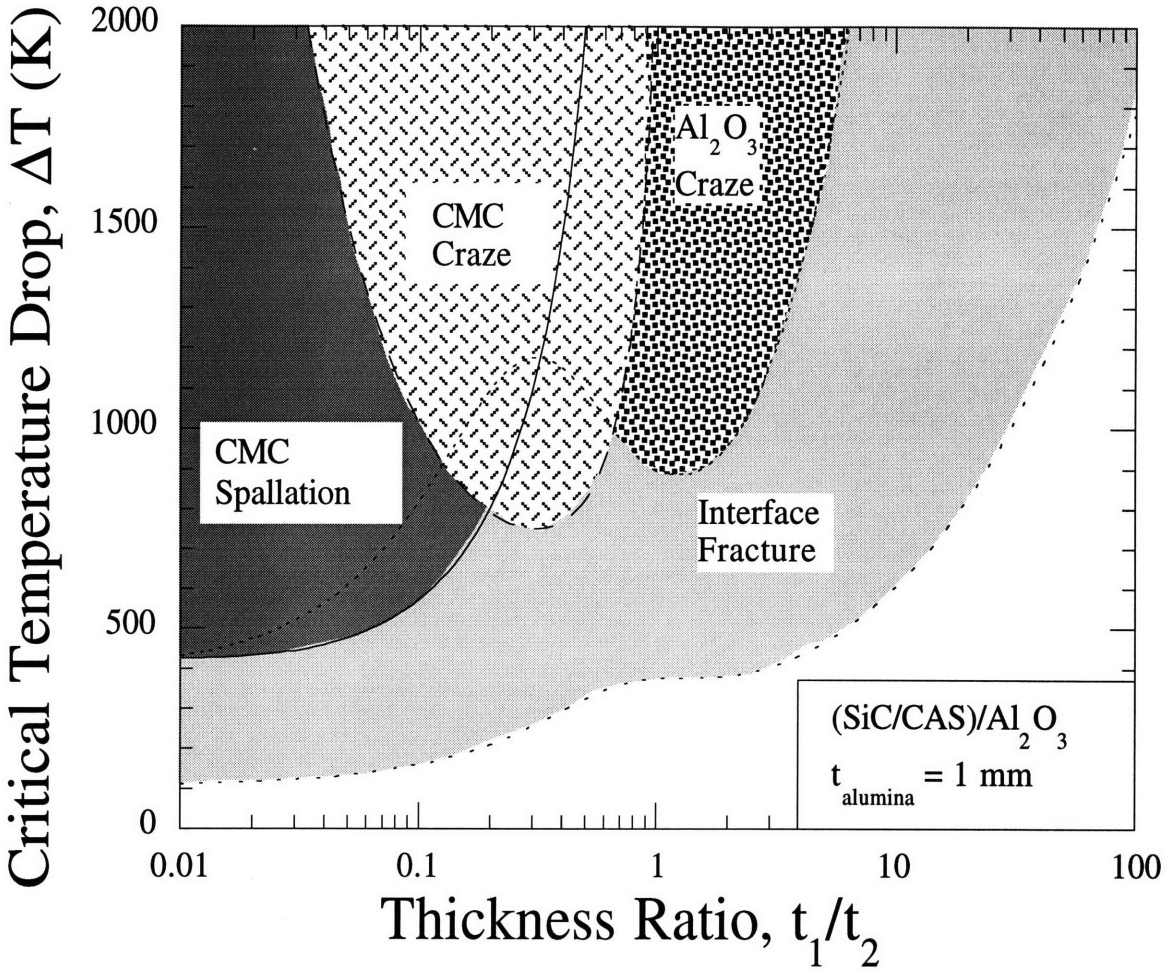

Figure 6.7 Failure mechanism diagram for alumina/ Nicalon-reinforced CAS.

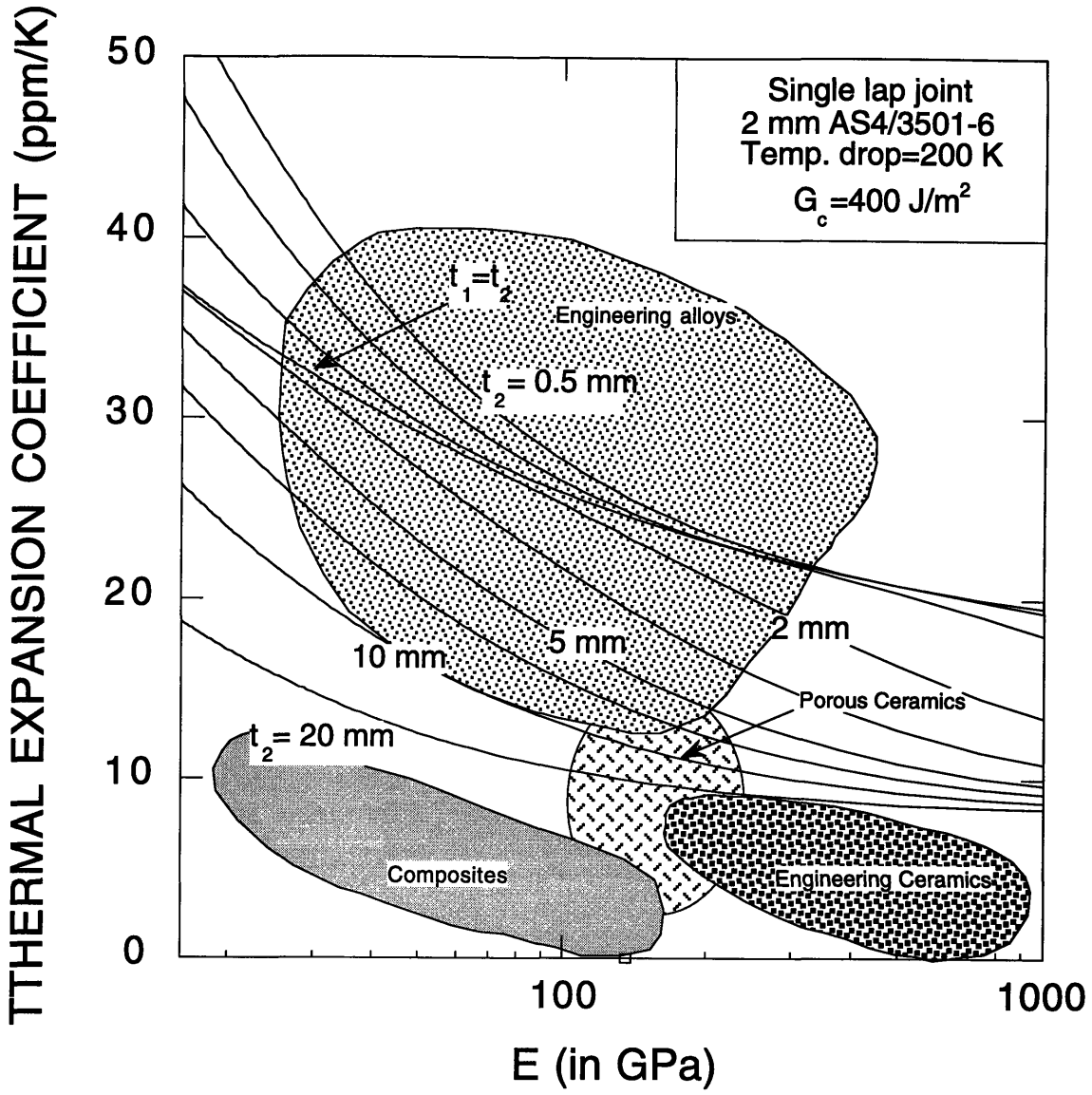

Figure 6.8 E-α contour map for selection of material to be joined with 2mm thick AS4/3501-6 graphite-epoxy in order to avoid interfacial fracture. The rectangle on the x-axis shows the coordinates of unidirectional AS4/3501-6.

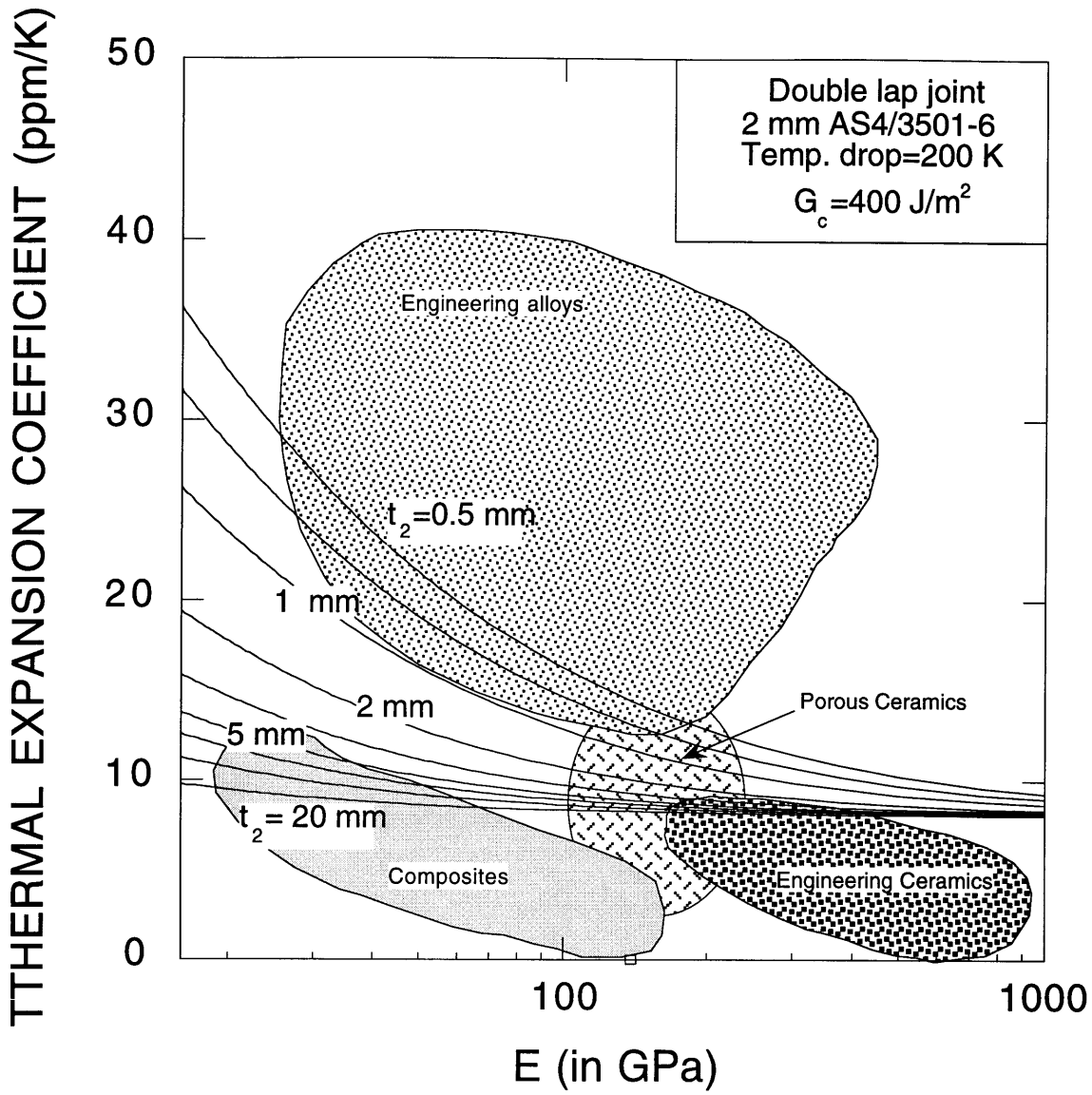

Figure 6.9 E-α contour map for selection of material to be joined with 2mm thick AS4/3501-6 graphite-epoxy on both sides to form a symmetric double lap joint. Design is against interfacial fracture. The rectangle on the x-axis shows the coordinates of unidirectional AS4/3501-6.

CHAPTER 7

CONCLUSIONS AND RECOMMENDATIONS

Steady-state fracture mechanics have been combined with strength of materials concepts to describe the failure of lap joints between metals and composites under thermal loading. As described in chapter 3, the method is perfectly general and can be applied to any combination of materials provided they behave in a linear, elastic, and brittle manner. Non-linearities, viscoelasticity, and other higher order effects can be included in a refined model for the purposes of detailed design. However, this thesis has attempted to formulate a relatively simple methodology for preliminary material selection and design, and those issues have not been addressed.

Experimental results have shown that steady-state fracture solutions can provide a useful bound to experimental results in many circumstances. Using the failure mechanism diagrams presented herein, failure mode analysis and material selection for preliminary design purposes can be conveniently made. However, the designer should be aware that use of simple fracture criteria such as a single value of fracture energy can, in some cases, lead to overly conservative design. Additional factors such as the mode-

mixity of the applied loading, dependence of properties on temperature, and material non-linearities also need to be considered for efficient joint design. Also, practical situations may differ from the assumed conditions. For example, steady-state thermal loading conditions are assumed here; in practice, thermal transients (thermal shock), and temperature gradients could play an important role. In lifetime critical applications, fatigue, material degradation (corrosion), and creep may also be of concern. These factors have to be taken into account before a final choice of materials, geometry and joining method is made.

7.1 CONCLUSIONS

The discussion presented in chapter 6 and in the previous paragraph leads to the following conclusions:

1. Failure of adhesive lap joints, and layered materials in general, is determined by layer thicknesses, material property mismatch, and temperature change.
2. Steady-state fracture solutions provide conservative lower bounds for predicting the failure of adhesive lap joints under thermal loading.
3. In addition to predicting the trends in the critical temperature drop to cause failure, steady-state fracture solutions can also predict the failure mode and crack trajectory as a function of the following:

- adherend thermoelastic properties and configurations (for the case of composite)
- adherend thickness
- single vs. double lap joint

4. Double lap joints are more prone to interfacial fracture than single lap joints under thermal loading.
5. A single value of adhesive fracture toughness is insufficient to characterize failure for the joint configurations employed in the thermal testing experiments.
6. Pre-cracking test specimens is an effective way of ensuring steady-state behavior.
7. Mechanical fracture toughness testing can provide bounds for the mixed-mode fracture resistance of an adhesive interface under thermo-mechanical loading.
8. Scrim-reinforced fibers can exhibit rapidly rising R-curves in both mode I and mode II loading. The R-curve results from the pull-out of scrim fibers.
9. Calculation of bridging parameters for an R-curve from an assumed constitutive law can be useful for design purposes.
10. Failure mechanism maps are potentially useful for preliminary design and failure mode analysis.

7.2 RECOMMENDATIONS FOR FUTURE WORK

There are a number of issues raised by this work which warrant further investigation. The most important issue which was not completely resolved is the reason for the experimentally observed non-unique value of adhesive fracture toughness as a function of adherend thickness ratio. This can be resolved by carrying out a comprehensive investigation as outlined below.

1. The adhesive constitutive behavior was a factor that was not examined quantitatively. A numerical J-integral formulation based on an adhesive constitutive law, using finite element analysis (FEA) is required. The *in situ* adhesive yield stress may be obtained from micro-indentation tests.
2. The temperature dependence of adhesive properties should be verified experimentally by carrying out fracture toughness tests at lower temperatures, to eliminate (or substantiate) any doubts in this regard.
3. The "short crack" effect should to be examined in more detail both experimentally and numerically. Numerically, FEA can be utilized to observe whether changing the boundary conditions on the adherends changes the crack length required to attain steady-state. Specimens with longer precrack lengths also need to be manufactured and tested to see if the critical temperature for fracture changes. Also, longer and

wider specimens should to be tested to ensure that edge effects do not play a role in the observed failure

4. A more reliable estimate of when fracture occurs is needed; sometimes it is difficult to determine whether the precrack has propagated, even under a microscope, especially for small crack opening displacements. X-ray radiography is one technique that is potentially useful for this purpose. This would ensure that critical temperatures for fracture are accurately recorded.

In addition to resolving the issues cited above, extension of this work could proceed in the following directions:

1. Further collection of thermal test data is necessary, for additional combinations of adherends and adhesives. The composite stacking sequence should also to be varied to include commonly used configurations such as quasi-isotropic.
2. The analytical formulation can be easily extended to incorporate the effect of mechanical loads on the adherends. Further extension to include the failure behavior of plates is required. For configurations in which matrix cracking is a concern, fracture mechanics analysis combined with a shear lag model for prediction of stresses can be employed. The analytical methodology needs to be extended to include this.

3. The possibility of extending the analytical formulation to incorporate the following needs to be examined:

   - The effect of fatigue, both thermal and mechanical.
   - Other configurations of adhesive joints (scarf, stepped-lap, etc.).
   - Material non-linearities, such as plasticity.

4. Development of a computer code to generate failure design maps for any combination of materials and adhesives, which the user can choose from an available database, would be useful for preliminary design purposes.

REFERENCES

1. Finot, M., "Deformation of Multi-layered and Graded Materials: Theory and Experiments", MIT, Doctoral Thesis, 1996.

2. Suresh, S., Giannakopoulos, A. E., and Olsson, M., "Elastoplastic Analysis of Thermal Cycling: Layered Materials with Sharp Interfaces", *J. Mech. Phys. Solids*, Vol. 42, 1994, pp. 979-1018.

3. Spearing, S. M., "Design Diagrams for Reliable Layered Materials", *37th AIAA/ASME/ASCE/AMS/ASC Structures, Structural Dynamics and Materials Conference*, Salt Lake City, UT, 1996, pp. 1458-1467.

4. Doerner, M. F. and Nix, W. D., "Stresses and Deformation Processes in Thin Films on Substrates", *CRC Critical Reviews in Solid States and Materials*, Vol. 14, 1988, pp. 225-268.

5. Stoney, G. G., "The Tension of Metallic Films Deposited by Electrolysis", *Proc. R. Soc. Lond. Ser.*, Vol. A82, 1909, pp. 172-175.

6. Timoshenko, S., *J. Opt. Soc. of America*, Vol. 11, 1925, pp. 233-255.

7. Boley, B. A. and Weiner, J. H., *Theory of Thermal Stresses*, Krieger, 1985.

8. Jones, R. M., *Mechanics of Composite Materials*, McGraw Hill Kogakusha Limited, Tokyo, 1975.

9. Erdogan, F., "Stress Distribution in Bonded Dissimilar Materials with Cracks", *J. Appl. Mech.*, Vol. 32, 1965, pp. 400-402.

10. Erdogan, F. and Arin, K., "Penny-shaped Interface Crack between an Elastic Layer and a Half Space", *Int. J. Engng. Sci.*, Vol. 10, 1972, pp. 115-125.

11. England, A. H., "A Crack between Dissimilar Media", *J. Appl. Mech.*, Vol. 32, 1965, pp. 400-402.

12. Rice, J. R. and Sih, G. C., "Plane Problems of Cracks in Dissimilar Media", *J. Appl. Mech.*, Vol. 32, 1965, pp. 418-423.

13. Dundurs, J., "Edge Bonded Dissimilar Orthogonal Elastic Wedges under Normal and Shear Loading", *J. Appl. Mech.*, Vol. 36, 1969, pp. 650-652.

14. Hutchinson, J. W. and Suo, Z., "Mixed Mode Cracking in Layered Materials", *Advances in Applied Mechanics*, Vol. 29, 1991, pp. 63-191.

15. Suo, Z. and Hutchinson, J. W., "Steady State Cracking in Brittle Substrates beneath Adherend Films", *Int. J. Solids Structures*, Vol. 25, 1989, pp. 1337-1353.

16. Suo, Z. and Hutchinson, J. W., "Interface Crack Between Two Elastic Layers", *Int. J. Fracture*, Vol. 43, 1990, pp. 1-18.

17. Evans, A. G. and Hutchinson, J. W., "Thermomechanical Integrity of Thin Films and Multilayers", *Acta Metall. and Mater.*, Vol. 43, 1995, pp. 2507-2530.

18. Charalambides, M., Kinloch, A. J., Wang, Y., and Williams, J. G., "On the Analysis of Mixed-mode Fracture", *Int. J. Fracture*, Vol. 54, 1992, pp. 269-291.

19. Suo, Z. and Hutchinson, J. W., "On Sandwich Test Specimens for Measuring Interface Crack Toughness", *Mater. Sci. Engng.*, Vol. A 107, 1988, pp. 135-143.

20. Charalambides, P. G., Lund, J., Evans, A. G., and McMeeking, R. M., "A Test Specimen For Measuring the Mixed-mode Fracture Resistance of Bimaterial Interfaces", *J. Appl. Mech.*, Vol. 56, 1989, pp. 77-82.

21. Reimanis, I. E., Dalgleish, B. J., and Evans, A. G., "The Fracture Resistance of a Model Metal/Ceramic Interface", *Acta Metall.*, Vol. 39, 1991, pp. 3133-41.

22. Dalgleish, B. J., Reimanis, I. E., and Evans, A. G., "The Strength of Ceramics Bonded with Metals", *Acta Metall.*, Vol. 36, 1988, pp. 2029-35.

23. Bagchi, A., Lucas, G. E., Suo, Z., and Evans, A. G., "A New Procedure for Measuring the Decohesion Energy for Ductile Films on Substrates", *J. Mater. Res.*, Vol. 9, 1994, pp. 1734-1741.

24. Cannon, R. M., Fisher, R., and Evans, A. G., "Decohesion of Thin Films from Ceramics", *Mat. Res. Soc. Symp. Proc.*, 1986, pp. 799-804.

25. Hu, M. S., Thouless, M. D., and Evans, A. G., "The Decohesion of Thin Films from Brittle Substrates", *Acta Metall.*, Vol. 36, 1988, pp. 1301-1307.

26. Thouless, M. D., Evans, A. G., Ashby, M. F., and Hutchinson, J. W., "The Edge Cracking and Spalling of Brittle Plates", *Acta Metall.*, Vol. 35, 1987, pp. 1301-1307.

27. Drory, M. D., Thouless, M. D., and Evans, A. G., "On the Decohesion of Residually Stressed Thin Films", *Acta Metall.*, Vol. 36, 1988, pp. 2019-2028.

28. Nix, W. D., "Residual Stresses and Fracture of Thin Films", *Met. Trans.*, Vol. 20A, 1989, pp. 2217.

29. Volkerson, O., "Die Nietkraftverteilung in Zugbeanspruchten Nietverbindungen mit Konstanten Laschen-querschnitten", *Luftfahrtforschung*, Vol. 15, 1938, pp. 4-47.

30. Goland, M. and Reissner, E., "The Stresses in Cemented Joints", *J. Appl. Mech.*, Vol. 11, 1944, pp. A17-A27.

31. Hart-Smith, L. J., "Adhesively Bonded Single Lap Joints", NASA CR 112236, 1973.

32. Hart-Smith, L. J., "Adhesively Bonded Double Lap Joints", NASA CR 112235, 1973.

33. Hart-Smith, L. J., *Developments in Adhesives-2*, ed. Kinloch, A. J. Appl. Sci. Publ., London, 1981.

34. Renton, W. J. and Vinson, J. R., "On the Behavior of Bonded Joints in Composite Material Structure", *Engng. Fract. Mech.*, Vol. 7, 1975, pp. 41-60.

35. Allman, D. J., *Quarterly J. Mechanics Appl. Maths.*, Vol. 30, 1977, pp. 415.

36. Wooley, G. R. and Carver, D. R., *J. Aircraft*, Vol. 8, 1971, pp. 817.

37. Wang, S. S., Mandell, J. F., Christiansen, T. H., and McGarry, F. J., "Analysis of Lap Shear Adhesive Joints with and without Short Edge Cracks", R76-2, MIT, 1976.

38. Reddy, J. N. and Roy, S., "Non-linear Analysis of Adhesively Bonded Joints", *Int. J. Non-Linear Mechanics*, Vol. 23, 1988, pp. 97-112.

39. Ripling, E. J., Mostovoy, S., and Corten, H. T., "Fracture Mechanics: A tool for evaluating Structural Adhesives", *J. Adhesion*, Vol. 3, 1971, pp. 107-123.

40. Fleck, N. A., Hutchinson, J. W., and Suo, Z., "Crack Path Selection in a Brittle Adhesive Layer", *Int. J. Solids Structures*, Vol. 27, 1991, pp. 1683-1703.

41. Thouless, M. D., "Fracture Resistance of an Adhesive Interface", *Scripta Metallurgica et Materialia*, Vol. 26, 1992, pp. 949-951.

42. Cao, H. C. and Evans, A. G., "An Experimental Study of the Fracture Resistance of Bimaterial Interfaces", *Mech. of Materials*, Vol. 7, 1989, pp. 295-304.

43. Chai, H., "A Note on Crack Trajectory in an Elastic Strip Bounded by Rigid Substrates", *Int. J. Fracture*, 1987, pp. 211-213.

44. Kinloch, A. J., *Adhesion and Adhesives*, Chapman and Hall, London, 1987.

45. "ASTM Standard D1002-94", in *Annual Book of ASTM Standards*, Vol. 15.06, 1994.

46. "ASTM Standard D3528-92", in *Annual Book of ASTM Standards*, Vol. 15.06, 1994.

47. "ASTM Standard D3167-93", in *Annual Book of ASTM Standards*, Vol. 15.06, 1994.

48. "ASTM Standard D295-92", in *Annual Book of ASTM Standards*, Vol. 15.06, 1994.

49. "ASTM Standard D2557-93", in *Annual Book of ASTM Standards*, Vol. 15.06, 1994.

50. "ASTM Standard D1151-90", in *Annual Book of ASTM Standards*, Vol. 15.06, 1994.

51. "ASTM Standard D3433-93", in *Annual Book of ASTM Standards*, Vol. 15.06, 1994.

52. Gent, A. N. and Kinloch, A. J., *J. Polymer Sci.*, Vol. 50, 1971, pp. 107.

53. Bascom, W. D. and Cottington, R. L., *J. Adhesion*, Vol. 7, 1976, pp. 333.

54. Gledhill, R. A., Kinloch, A. J., Yamini, S., and Young, R. J., *Polymer*, Vol. 19, 1978, pp. 574.

55. Spearing, S. M., Tenhover, M. A., Lukco, D. B., Viswanathan, L., and Hollen, D. K., "Models for the Thermomechanical behavior of Metal/Ceramic Laminates", *Mat. Res. Soc. Symp.*, 1994,

56. Shetty, S. P. and Spearing, S. M., "The Reliability of Composite-Metal Adhesive Joints Subject to Thermo-mechanical Loading", *38th AIAA/ASME/ASCE/AMS/ASC Structures, Structural Dynamics and Materials Conference*, Orlando, FL, 1997, pp. to be published.

57. Shetty, S. P. and Spearing, S. M., "Fracture of Composite-Metal Joints under Thermo-mechanical Loading", *ICCM 11*, 1997, pp. to be published.

58. Timoshenko, S., *Strength of Materials I*, 2nd ed., Van Nostrand, 1940.

59. Aveston, J., Cooper, G., and Kelley, A., *Properties of Fiber Composites: Single and Multiple Fracture*, IPC Science and Technology Press Ltd., Surrey, UK, 1971.

60. Laws, N. and Dvorak, G. J., "Progressive Transverse Cracking in Composite Laminates", *J. Compos. Mater.*, Vol. 22, 1988, pp. 900-915.

61. Spearing, S. M. and Zok, F. W., "Stochastic Aspects of Matrix Cracking in Brittle Matrix Composites", *J. Eng. Mater. Technol.*, Vol. 115, 1993, pp. 314-318.

62. Maddocks, J. R., "Microcracking in Composite Laminates under Thermal and Mechanical Loading", MIT, Masters Thesis, 1995.

63. Shetty, S. P. and Spearing, S. M., "Fracture Resistance of a Fiber-Reinforced Film Adhesive", *Scripta Materialia*, 1997, pp. in press.

64. Akisanya, A. R. and Fleck, N. A., "The Edge Cracking and Decohesion of Thin Films", *International Journal of Solids and Structures*, Vol. 31, 1994, pp. 3175-3199.

65. Lagace, P. A., Brewer, J. C., and Varnerin, C., "*TELAC Manufacturing Course Notes*", TELAC Report 88-4B, Massachusetts Institute of Technology, 1990.

66. Grady, J. E., "Fracture Toughness Testing of Polymer Matrix Composites", *NASA-TP-3199*, NASA, Lewis Research Center, Cleveland, OH, 1992.

67. Carlsson, L. A., Gillespie, J. W., and Trethewey, B. R., "On the Analysis and Design of the End Notched Flexure (ENF) Specimen for Mode II testing", *J. Compos. Mater.*, Vol. 20, 1986, pp. 594.

68. Anderson, T. L., *Fracture Mechanics: Fundamentals and Applications*, 2nd ed., CRC Press, Boca Raton, 1995.

69. Palazotto, A. N. and Birman, V., "Review of Fracture in Adhesive Joints Considering Rocket Motor Application", *J. Spacecraft and Rockets*, 1995, pp. 538.

70. Kassapoglou, C. and Lagace, P. A., "An Efficient Method for the Calculation of Interlaminar Stresses in Composite Materials", *J. Appl. Mech.*, Vol. 53, 1986, pp. 744-750.

71. Spearing, S. M. and Evans, A. G., "The Role of Fiber Bridging in the Delamination Resistance of Fiber-Reinforced Composites", *Acta Metall. Mater.*, Vol. 40, 1992, pp. 2191.

72. Suo, Z., Bao, G., and Fan, B., "Delamination R-Curve Phenomena due to Damage", *J. Mech. Phys. Solids*, Vol. 40, 1992, pp. 1.

73. Foote, R. M. L., Mai, Y.-W., and Cotterell, B., "Crack Growth Resistance Curves in Strain-Softening Materials", *J. Mech. Phys. Solids*, Vol. 34, 1986, pp. 593-607.

74. Smiley, A. J. and Pipes, R. B., "Rate Effects on Mode I Interlaminar Toughness in Composite Materials", *J. Compos. Mater.*, Vol. 21, 1987, pp. 670-687.